Using Optical Resonances for Chemical and Biological Sensing Applications

By

MELIKHAN TANYERI
B.S. (Bogazici University) 1999
M.S. (University of California, Davis) 2000

DISSERTATION

Submitted in partial satisfaction of the requirements for the degree of

DOCTOR OF PHILOSOPHY
in
PHYSICS

in the

OFFICE OF GRADUATE STUDIES

of the

UNIVERSITY OF CALIFORNIA

DAVIS

Approved:

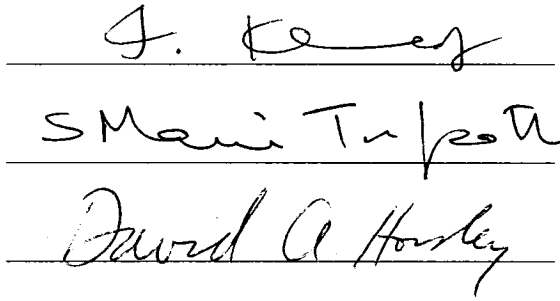

Committee in Charge

2007

Reproduced with permission of the copyright owner. Further reproduction prohibited without permission.

UMI Number: 3261197

INFORMATION TO USERS

The quality of this reproduction is dependent upon the quality of the copy submitted. Broken or indistinct print, colored or poor quality illustrations and photographs, print bleed-through, substandard margins, and improper alignment can adversely affect reproduction.

In the unlikely event that the author did not send a complete manuscript and there are missing pages, these will be noted. Also, if unauthorized copyright material had to be removed, a note will indicate the deletion.

UMI®

UMI Microform 3261197

Copyright 2007 by ProQuest Information and Learning Company.

All rights reserved. This microform edition is protected against unauthorized copying under Title 17, United States Code.

ProQuest Information and Learning Company
300 North Zeeb Road
P.O. Box 1346
Ann Arbor, MI 48106-1346

Reproduced with permission of the copyright owner. Further reproduction prohibited without permission.

To my lovely wife,

Reproduced with permission of the copyright owner. Further reproduction prohibited without permission.

Acknowledgements

Finishing a Ph.D. requires dedication, persistence and hard work. It starts with a diligent application process which takes months to prepare. After getting admission, you start taking the coursework and meanwhile choose a research topic and an advisor. One needs a lot of things going on his/her way during dissertation research; a balanced blend of guidance, advice, support and help. During the whole course of the doctoral program, there are good times and there are bad times. Good moments make you enjoy what you are doing and keep you on track in pursuing the degree. During the hard times, the people surrounding you can offer the desperately needed intellectual and motivational support. I was lucky enough to have many people around me to provide me with the encouragement and inspiration to finish my degree.

First of all, I would like to thank to my advisor Prof. Ian M. Kennedy. He always encouraged me to come up with my own ideas and implement them. To me, becoming an independent researcher is the major outcome of a Ph.D. degree and Ian provided me the flexibility and openness to attain the necessary skills and the

Reproduced with permission of the copyright owner. Further reproduction prohibited without permission.

mindset to achieve this goal. Having a good advisor is like getting half of your Ph.D. already done.

I would like to also thank to my dissertation committee members; Prof. Mani Tripathi and Prof. David Horsley. Mani encouraged me to choose an advisor outside the department. Without his help, I will not be able to work on the projects that I was interested in. He also supported me to finish my Ph.D. and raised my self-confidence during tough times. Prof. David Horsley was especially helpful during my last project. He personally helped preparing the setup to acquire some nice images of the microdroplets. Special thanks to Meilin Chan, his graduate student, for helping out when I needed.

During the first few years of my Ph.D., I was lucky enough to have Dr. Jun Feng in our lab. He was previously a professor in China before joining our lab and advised his own graduate students. He was always an excellent source of advice and encouragement. From him, I understood the importance of planning and patience to finish a project.

"My neighbors", Dr. Dosi Dosev and Dr. Mikaela Nichkova were also a source of inspiration for me. Mikaela helped me to prepare any biological sample needed for my experiments. She also provided valuable insight and knowledge regarding the biosensing aspect of my projects. Without her input, it would be impossible for me to evaluate the feasibility of experiments on the biology end. Dosi helped me to get some images in the confocal microscope. He was also an excellent source of advice along with Mikaela when I come across a problem.

I would like to thank Rick Perron for his extensive help and collaboration for fabricating the T-junction microdroplet generator that I used during my last project. His discipline and hard work paid off very well and I was able to finish the

Reproduced with permission of the copyright owner. Further reproduction prohibited without permission.

project in eight months. Surprisingly, we presented this project as a final homework in one of my graduate classes that I took five years ago. It was particularly satisfying to achieve what I proposed at the beginning of your Ph.D.

Dr. Bing Guo (now a professor at Texas A&M University) was very helpful when I needed any help or advice in troubleshooting problems. I wish him good luck in getting his tenure.

Hammock Lab (Prof. Bruce D. Hammock) was the main collaborator of our research group and I consulted them for the biology part of my experiments. People working in his lab, Dr. Mikaela Nichkova and Dr. Marja Koivunen were quite nice and helpful in providing help.

For the cell detection experiments, I would like to thank Kristin Hicks, Hussna Wakily and Dr. Krassimira Hristova for both teaching and helping me out to grow and harvest bacterial cells.

And last but not least, I am thankful to my wonderful wife, Nihan, for giving me her love, encouragement and support during the last year of my Ph.D. I am lucky to meet her at the right time and at the right place. She is an inspiration and steady source of joy that uplifts my energy and motivation to do my best in my job. We got engaged during my last year and the plan was to get married after finishing my Ph.D. Her love and support shortened the path to our wedding ceremony.

Doing my dissertation research was a great learning experience for me. I learned how to come up with a problem to work on through sifting the literature and talking to people in the field. I also learned about various experimental techniques and developed and improved my own setup. I also enhanced my presentation and writing skills. Without the help and support of the people around me, it would be very difficult to accomplish all these. I appreciate them all.

Reproduced with permission of the copyright owner. Further reproduction prohibited without permission.

Abstract

The detection of single bacterial cells has been demonstrated through optical resonances in microdroplets. The experimental setup enables high throughput detection of single Escherichia coli (E. Coli) cells without any direct labeling although Rhodamine 6G (R6G) has been used as the signal transduction mechanism. A microdroplet acts as an optical cavity that supports Morphology Dependent Resonances (MDRs) at wavelengths where the droplet circumference is an integer multiple of the emission wavelength. The cells inside the droplet have a direct effect on the fluorescence lasing spectrum of R6G fluorescence by means of scattering and local refractive index change. The change in the lasing spectrum can be observed at the concentrations where each droplet has as little as one cell.

Enhanced radiative energy transfer through the optical resonances can also be utilized as a transduction mechanism for chemical and biological sensing. Enhancement in radiative energy transfer is observed when a donor/acceptor pair is present in the resonant medium of a microcavity. Avidin-biotin binding and its detection through a FRET pair has been demonstrated as a potential application for ultra-sensitive detection for fluoroimmunoassays. The binding interaction be-

Reproduced with permission of the copyright owner. Further reproduction prohibited without permission.

tween the biotinylated fluorescent beads (donor) and streptavidin-Alexa Fluor 555 (acceptor) conjugate was used to observe the radiative energy transfer between the dye pairs. Strong coupling of acceptor emission into optical resonances shows that the energy transfer is efficiently mediated through these resonances.

The radial modes of MDRs extend to approximately 0.6 r_0 inside the droplet. As a result, the fluorescent emission around the center is not coupled to the optical resonances losing sensitivity. To address this problem, water-in-oil emulsions of avidin and biotin containing solutions were prepared. The water phase contains the streptavidin-Alexa Fluor 610 and the oil phase contains biotinylated fluorescent bead. Streptavidin-biotin binding reaction occurs at the water-oil interface. The water phase accumulates at the droplet air interface due to higher specific density enhancing the resonance coupling. Water and oil phase were index-matched to avoid scattering problems. As a result, a large portion of the avidin-biotin complex was localized at the pendant droplet and air interface. An increase in the efficiency of energy transfer mediated through optical resonances was observed.

Lasing from spherical microdroplets ejected into a liquid medium with lower refractive index is observed in a microchannel. A microfabricated device that combines the droplet production and excitation/detection has been utilized. Droplets of 50 μm-diameter containing a fluorescent dye were first detected and then excited through multimode fibers after their production at a T-junction. Images show intense lasing emission around the droplet rim. Spectra from the droplets exhibit morphology dependent resonances (MDRs) which are red shifted relative to the bulk fluorescence emission from the dyes. The dependence of resonant peak intensities on the pump beam power is nonlinear.

Reproduced with permission of the copyright owner. Further reproduction prohibited without permission.

Table of Contents

Dissertation Title page i

Acknowledgements iii

Abstract vi

Table of Contents viii

List of Figures and Tables x

Publication List xii

Chapter 1: Introduction 1

A. Biosensors 1

1. Biological Recognition Mechanisms 2

2. Signal Transduction Mechanisms 3

B. Optical Biosensors 5

1. Indirect Detection (Labeled Analytes) 6

2. Direct Detection (Non-labeled Analytes) 7

C. Optical Resonances in Microcavities as a Biosensing Mechanism 8

Chapter 2: Optical Resonances in Microcavities: Theory and Applications 10

A. Introduction 10

1. Optical Resonances in Microcavities 11

a. Wave Optics or Ray Approach 12

b. Electromagnetic Wave (Mie Scattering) 13

c. Quantum Mechanics (Bohr Atom analogy) 17

2. Q-factor 25

B. Lasing in Microcavities 26

C. FRET in Microcavities 28

Chapter 3: Using Optical Resonances in Microcavities for Chemical and Biological Sensing 34

Chapter 4: Detecting Single Bacterial Cells through Optical Resonances in Microdroplets 42

A. Introduction 42

B. Methods and Materials 43

C. Results and Discussion 48

Reproduced with permission of the copyright owner. Further reproduction prohibited without permission.

Chapter 5: Fluorescent Immunoassays in Microdroplets through Radiative Energy Transfer Mediated by Optical Resonances 53

A. Introduction 53
B. Methods and Materials 55
C. Results and Discussion 59

Chapter 6: Pendant Droplet Approach to Immunoassays in Microdroplets 68

A. Introduction 68
B. Methods and Materials 69
C. Results and Discussion 73

Chapter 7: Lasing Microdroplets in a Microfabricated Channel 81

A. Introduction 81
B. Methods and Materials 82
C. Results and Discussion 86

Chapter 8: Conclusion 90

A. Summary 90
B. Future Work 92
1. Microspheres fused/attached on a coverslip excited by TIR 94
2. Monodisperse microsphere stream in a microfabricated channel 96

Appendix A – Fabrication of a T-junction Microfluidic Device for Droplet Generation 99

A. Materials 99
B. Fabrication 99

Bibliography 104

Reproduced with permission of the copyright owner. Further reproduction prohibited without permission.

List of Figures & Tables

Figures

Figure 2.1 First experimental observation of optical resonances in liquid microcavities.

Figure 2.2 Ray optics description of optical resonances within microcavities.

Figure 2.3 Effective potential for the photonic atom model of a spherical particle.

Figure 2.4 Photonic atom model of optical resonances in microcavities.

Figure 2.5 Overview of Fluorescence Resonance Energy Transfer (FRET)

Figure 3.1 Biosensing with a spheroid optical fiber tip.

Figure 3.2 Subfemtomole detection of small molecules by a microsphere-based sensor.

Figure 3.3 A ring resonator biosensor.

Figure 4.1 Experimental setup for optical resonance experiments in microdroplets.

Figure 4.2 Suppression of MDR peaks in a microdroplet due to a single cell presence.

Figure 4.3 Single cell detection through optical resonances in microdroplets.

Figure 5.1 Experimental setup for fluorescent immunoassay experiments in microdroplets.

Figure 5.2 Fluorescein quenching (physical) upon streptavidin binding.

Figure 5.3 FRET observed between fluorescent nanobeads and Alexa 555 through streptavidin-biotin binding.

Figure 5.4 Detection of binding reaction between streptavidin and biotin through enhanced energy transfer in a microdroplet.

Figure 5.5 Acceptor emission from enhanced FRET (fluorescent radiative energy transfer) experiments in microdroplets.

Figure 6.1 Experimental setup for pendant microdroplet experiments.

Figure 6.2 Confocal micrograph of the water droplets in oil phase.

Figure 6.3 Using emulsion approach in pendant microdroplet experiments.

Figure 6.4 Results of the pendant droplet experiment using emulsion approach.

Figure 6.5 Transition between the bulk emission and the emission coupled to the resonances of a pendant droplet as the droplet grows.

Figure 6.6 Biotin-4-fluorescein emission spectrum in a pendant droplet.

Reproduced with permission of the copyright owner. Further reproduction prohibited without permission.

Figure 7.1 The layout of the microfabricated droplet generator.

Figure 7.2 Experimental setup for optical resonance experiments in microdroplets produced in a T-junction microfluidic device.

Figure 7.3 Droplet lasing in a microchannel.

Figure 7.4 Lasing spectra from 50-60 μm diameter water-glycerol droplets containing 10 μM Rhodamine 6G or Fluorescein.

Figure 8.1 Microspheres fused/attached on a coverslip and optical resonances are excited by Total Internal Reflection.

Figure 8.2 Monodisperse microspheres in a microchannel for immunoassay applications based on optical resonances.

Figure A.1 Layout of a T-junction microdroplet generator.

Figure A.2 Layout of a flow focusing microdroplet generator.

Tables

Table 2.1 Analogy between conventional lasers and liquid microcavity lasing.

Table 3.1 Potential applications of optical resonances.

Reproduced with permission of the copyright owner. Further reproduction prohibited without permission.

Publication List

Papers

1. R. Perron, M. Tanyeri, I. M. Kennedy "Monodisperse emulsion production at low breakup rates in a modified T-junction microfluidic device" (to be submitted to Applied Physics Letters)
2. M. Tanyeri, R. Perron, I. M. Kennedy, "Lasing Droplets in a Microfluidic T-junction Device with Integrated Optics" (to appear in Proc. SPIE Vol. 6465, Microfluidics, BioMEMS, and Medical Microsystems V, March 2007)
3. M. Tanyeri, R. Perron, I. M. Kennedy, "Lasing Droplets in a Microfabricated Channel" (to be submitted to Optics Letters)
4. M. Tanyeri, I. M. Kennedy, "Detecting Single Bacterial Cells through Optical Resonances in Microdroplets" (submitted to Optics Letters)
5. M. Tanyeri, D.K. Dosev, I.M. Kennedy, "Chemical and Biological Sensing through Optical Resonances in Pendant Droplets", Proc. SPIE Vol. 6008, p. 114-125, Nanosensing: Materials and Devices II, November 2005
6. M. Tanyeri, I.M. Kennedy, "Chemical and biological sensing through optical resonances in microcavities", Proc. SPIE Vol. 5699, p. 227-236, Imaging, Manipulation, and Analysis of Biomolecules and Cells: Fundamentals and Applications III, March 2005
7. M. Tanyeri, I.M. Kennedy, "Microdroplets for integrated high-sensitivity biosensors", Proc. SPIE Vol. 5275, p. 133-140, BioMEMS and Nanotechnology, March 2004

Patents

1. M. Tanyeri, R. Perron, I. M. Kennedy "Optical Resonances in Droplets in a Microchannel", Application No: 60/808,768, May 25 2006

Presentations

1. (invited) "Optical microcavities for chemical and biological sensing". Biophotonics/Biophysics Colloquium, Center for Biophotonics Science & Technology, April 14 2006, University of California, Davis
2. "Biological Sensing through Optical Resonances in Pendant Droplets", Biophysical Society 50th Annual Meeting, February 18-22 2006, Salt Lake City, UT
3. (Invited) "Chemical and Biological Sensing through Optical Resonances in Pendant Droplets", SPIE Optics East 2005 Symposium, October 23-26 2005, Boston, MA

Reproduced with permission of the copyright owner. Further reproduction prohibited without permission.

4. "Chemical and biological sensing using optical resonances in microdroplets", Biophysical Society 49th Annual Meeting, February 12-16 2005, Long Beach, CA
5. "Chemical and biological sensing through optical resonances in microcavities", SPIE International Symposium on Biomedical Optics (BiOS), January 22-27 2005, San Jose, CA
6. "Detecting single cells using optical resonances in microdroplets", Biophysical Society 48th Annual Meeting, February 14-18 2004, Baltimore, MD

Reproduced with permission of the copyright owner. Further reproduction prohibited without permission.

Chapter 1

Introduction

A. Biosensors

A biosensor is an analytical device which incorporates a biological or biochemical response into discrete or continuous digital electronic signal – which is proportional to a single analyte or a related group of analytes – through a transducer.* The term "biosensor" is quite often used for devices that measure critical parameters for biological systems like concentration, pH and temperature.[1-4] The term, biosensor, consists of two parts: "Bio" relates the term to biological molecules and organisms. "Sensor" relates it to the physicochemical transduction mechanisms that are used to extract information about the biological process from the measurable signal.[5, 6]

It is apparent from the definition of the biosensor concept that the key parts of a biosensor are the biorecognition element and the transducer. For this reason,

* IUPAC definition of biosensors

Reproduced with permission of the copyright owner. Further reproduction prohibited without permission.

biosensors can be categorized into two: according to the biorecognition element or the transduction mechanism utilized in the biosensor.[7-15]

1. Biological Recognition Mechanisms

Biological recognition is accomplished by three basic mechanisms which are:

a. Biocatalytic-based,

b. Bioaffinity-based, and

c. Microorganism-based.

Each mechanism is briefly explained as follows:

a. Biocatalysis-based Recognition

Biocatalysis-based biosensors use enzymes.[16] Enzymes are large protein molecules that catalyze chemical reactions. The enzyme participates actively in the transformation of a specific substrate into a specific product but remains unchanged at the end of the reaction. In biosensors, enzymes are used as a recognition mechanism because of their specificity in terms of entering a chemical reaction.

Enzyme-based biosensors primarily rely on two operational mechanisms. The first mechanism involves the catalytic transformation of a biochemical molecule from a non-detectable form to a detectable form. The second mechanism involves the detection of biochemical molecules that inhibit or mediate the enzyme's activity.

b. Bioaffinity-based Recognition

Bioaffinity-based biosensors use antibodies.[17, 18] The term immunosensor is often used rather than biosensor, when the bio-recognition component of a bio-

Reproduced with permission of the copyright owner. Further reproduction prohibited without permission.

sensor is comprised of immunoglobulins/antibodies. Antibodies are also proteins, produced by the immune system of animals in response to the entry of "foreign" materials into the body – for example, viruses and bacteria. In contrast to enzymes, antibodies do not (usually) catalyze chemical transformations but rather undergo a physical transformation – they bind tightly to the foreign material (the antigen) that provoked the response and mark it for attack by other elements of the immune system. Antibodies are also very specific in recognizing and binding to the foreign substance only, and not to materials native to the organism. Typically, antibodies specifically directed against the substance of interest (i.e. the desired analyte) are immobilized on the transducer of the biosensor. Then, the sensor is exposed to the intended medium. If antigen is present in that medium, it will be bound by the antibody to form a larger antigen-antibody complex. This will change some physicochemical parameter (usually mass or an optical parameter) of the environment at the transducer surface of the sensor and that change is subsequently detected.

c. Microorganism-based Recognition

Microorganism-based biosensors rely on the measurable change of the cellular response of a microorganism either directly or through enzyme activity or gene expression.[19] Biosensors have also been developed with the use of genetically engineered microorganisms that recognize and report the presence of specific chemicals.

2. Signal Transduction Mechanisms

The biological recognition systems mentioned above have been linked to electrochemical, optical, and acoustic transducers:

Reproduced with permission of the copyright owner. Further reproduction prohibited without permission.

a. Electrochemical Transduction

There are three different mechanisms[20] that fall under the general area of electrochemical transduction.

The first one is the potentiometric transducer: The basic principle behind potentiometric measurements is the development of charge related to the analyte activity in the sample through the Nernst relation. Typically, a reference electrode and one working electrode, both in contact with the sample, are required.

The second type of electrochemical transducers is the amperometric transducer.[21] Amperometric biosensors typically rely on an enzyme system that catalytically converts electrochemically non-active analytes into products that can be oxidized or reduced at a working electrode. This electrode is maintained at a specific potential with respect to a reference electrode. The current produced is linearly proportional to the concentration of the electroactive product, which in turn is proportional to the non-electroactive enzyme substrate.

The third type is the conductometric transducer: Enzyme reactions that produce or consume ionic species will, depending on the total ionic strength of the media, change the conductance / capacitance of the solution. These changes are monitored to detect molecules that are involved in these enzymatic reactions.

b. Acoustic Transduction

A piezoelectric crystal can be used as a mass sensor due to the linear relationship between the change in its mass and its oscillating frequency.[22] A small mass change upon adsorption or specific binding of molecules/particles on the crystal surface shifts the resonant oscillating frequency of the piezo. Piezoelectric crystals, sometimes referred to as quartz crystal microbalances (QCM)[23], are typi-

Reproduced with permission of the copyright owner. Further reproduction prohibited without permission.

cally made of quartz and operate at frequencies between 1 and 10 MHz. These devices can operate in liquids with a frequency determination limit of 0.1 Hz; the detection limit of mass bound to the electrode surface is about 10-100 picograms. These transducers are usually coupled with enzymes and antibodies to detect analytes.

Micromechanical cantilever-based transduction is another example of acoustic transduction mechanism.[24, 25] Similar to QCM, a cantilever-based sensor also exhibit a change in its resonant frequency due to attachment of analytes on its surface. Materials as well as the dimensions used to construct these micro/nanomechanical sensors determine the sensitivity of the detection.

c. Optical Transduction

This technique is described in full detail in section B.

B. Optical Biosensors

The third and final category of signal transduction mechanisms is optical transduction.[26] Due to its relevance to this dissertation work, this transduction mechanism is reviewed under a separate title in this chapter.

Owing to the range and reliability of optical methods, a vast number of optical transduction techniques can be used for biosensor development.[27, 28] Optical transduction approaches to biosensors take a number of forms depending on the format of the device, type of biological recognition system chosen and the concentration range of the analyte to be measured. Specific techniques include absorbance, fluorescence, luminescence, refractive index and total internal reflection. The optical biosensor formats may involve direct detection of the analyte

Reproduced with permission of the copyright owner. Further reproduction prohibited without permission.

of interest or indirect detection through optically labeled probes. Optical transduction mechanisms can be divided into two main categories:

1. Indirect Detection (Labeled Analytes)

It is known that any chemical has a unique "finger-print" spectrum when examined by most spectroscopic methods. However, in most real-life situations, the molecule of interest (i.e. the analyte) is not present alone in the sample but is part of a "soup". All these different molecules contribute their spectral features, in proportion to their concentrations, to the overall measured spectrum of the sample. In a few cases, the spectrum of the desired analyte will be so different from those of its partners that it is "visible" above the background, and can thus be identified and quantified directly. But whenever this is not possible, an artificial optical label must be added to the system. The most common labels used in biosensors are fluorescent. We can group the indirect detection methods as follows:

a. Fiber Optic Biosensors

This transduction mechanism involves a single or a bundle of optical fibers to conveniently transport light to and from a sensing area – which is at the tip of the fiber – containing the bio-recognition elements.[29]

b. Total Internal Reflection Fluorescence (TIRF)

Total internal reflection occurs when a light wave traveling in a medium is incident at an interface with a second medium of relatively low refractive index. Above a critical incident angle, the light wave is completely reflected back to the initial medium with the same incident angle. An evanescent wave, which decays exponentially, penetrates approximately half a wavelength (200-250 nm for visible

Reproduced with permission of the copyright owner. Further reproduction prohibited without permission.

light) into the second medium. This evanescent light is used to excite the labeled analytes located at the interface in the second medium and the emission wave is collected through various microscopy techniques. This localization is ideal for bio-sensing as a thin film of bio-recognition molecules can be deposited at the interface and in the evanescent wave region. This results in the optical interrogation of only the recognition layer and not the bulk of the sample, reducing the background signal.

2. Direct Detection (Non-labeled Analytes)

a. Surface Plasmon Resonance (SPR)

The main non-labeled optical technique[30] that has been commercialized is the surface plasma resonance.[31] In SPR, incident light is reflected from the internal surface of a prism where the external surface is coated with a thin metal (usually gold) film. At a critical angle, the intensity of the reflected light is lost to resonant oscillation of free electrons (surface plasmons) at the surface of the metal film. Since the critical angle depends on the refractive index of material present on the metal surface, this method has been used to measure the specific binding reactions between antibodies and antigens immobilized at the sensor surface. The transduction surface is multilayered; consisting of quartz (prism surface), metal, antigen and antibody.

b. Light Addressable Potentiometric Transduction (LAPS)

The second major example of a non-labeled optical detection system is the hybrid electrochemical/optical LAPS – the Light-Addressable Potentiometric Sensor.[32] This sensor is based on arrays of semiconductor devices, on which the

Reproduced with permission of the copyright owner. Further reproduction prohibited without permission.

chemical/biological material has been immobilized. LAPS sensor is a semiconductor-based biosensor with an electrolyte-insulator-semiconductor (EIS) structure. When the device is illuminated with modulated light, a transient alternative current (AC) is measured against a bias voltage. I-V characteristics of the device depend on the surface potential, which is related to the surface pH. So it can be used as an effective pH sensor. When the sensor surface is modified accordingly, it may also be used to measure concentrations of various ions and molecules.

C. Optical Resonances in Microcavities as a Biosensing Mechanism

Optical resonances can be used as a transduction mechanism for chemical and biological sensing applications. Following the classification of signal transduction mechanisms above, optical resonances would fall into optical transduction mechanism. Although optical resonances can be used in direct or indirect detection format, recent studies have mainly demonstrated direct (label-free) detection of analytes. Bioaffinity-based recognition is the major biological recognition mechanism that is associated with resonant optical microcavities as the signal transduction mechanism. The experimental demonstration of the detection of a binding reaction between two biomolecules (e.g. avidin-biotin) on a resonant microcavity surface is a typical example of utilizing optical resonances for bioaffinity-based recognition.[33, 34] A review of the recent work describing the application of optical resonances for biosensing applications will be summarized in Chapter 3, "Using Optical Resonances in Microcavities for Chemical and

Reproduced with permission of the copyright owner. Further reproduction prohibited without permission.

Biological Sensing". The theoretical background for the optical resonances is presented in the next chapter.

Reproduced with permission of the copyright owner. Further reproduction prohibited without permission.

Chapter 2

Optical Resonances in Microcavities: Theory and Applications

A. Introduction

The optical resonances in microcavities are often called "Morphology Dependent Resonances" (MDRs) or "Whispering Gallery Modes" (WGMs) because the location of the resonant peaks in the spectrum depend on the morphological properties of the system like refractive indices of the droplet and its surrounding, the size and the shape of the droplet. These resonances occur at specific wavelengths inside a microcavity. For each resonance peak the droplet circumference is an integer multiple of that specific wavelength. If the resonance condition is met, the droplet becomes a high Q factor microcavity. The light can be confined up to microseconds, which means that the light can travel up to several hundred meters inside the droplets. That is about 5 million trips around the rim for a 20 μm droplet.

Reproduced with permission of the copyright owner. Further reproduction prohibited without permission.

This effect boosts the signal from any fluorescent label inside the cavity. The cavity also becomes very sensitive to the local refractive changes.

1. Optical Resonances in Microcavities

The theoretical work on optical resonances goes back to 1910 when Lord Rayleigh (John William Strutt) published a paper on the whispering gallery modes of sound waves traveling along the outer wall of a walkway in the circular dome of St. Paul's Cathedral in London.[35]

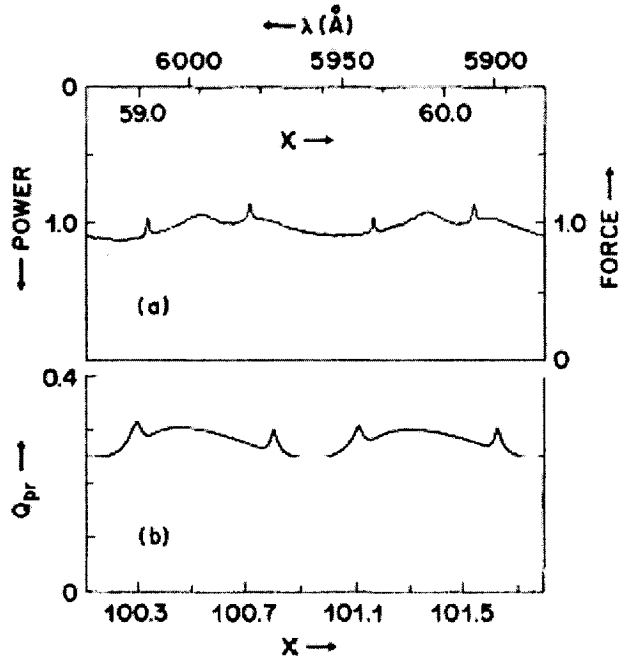

Figure 2.1 First experimental observation of optical resonances in liquid microcavities. Measured (above) and calculated (below) radiation pressure force vs. X for a droplet. The radiation pressure is directly related to light scattering, therefore the "ripple structure" corresponds to the resonances in the light scattering from the microdroplet. (Adopted from Ashkin et al., PRL, (1977))

The first experimental observation of optical resonances from a single microcavity was by Ashkin et al in 1977[36]. They measured the radiation pressure needed to levitate a single liquid (silicon oil) microdroplet by changing the size parameter x (where $x = 2\pi a / \lambda$). Sharp resonance peaks were observed due to

Reproduced with permission of the copyright owner. Further reproduction prohibited without permission.

"surface waves" from which the size of the droplet could be deduced to a precision of one part in ten thousand.† The resonant peak locations showed good agreement with the Mie scattering calculations.

Optical resonances can be explained through several approaches including geometrical optics, electromagnetic waves and quantum mechanics. We will provide short physical explanation and mathematical formalism for each description.

a. Ray Optics or Wave Approach:

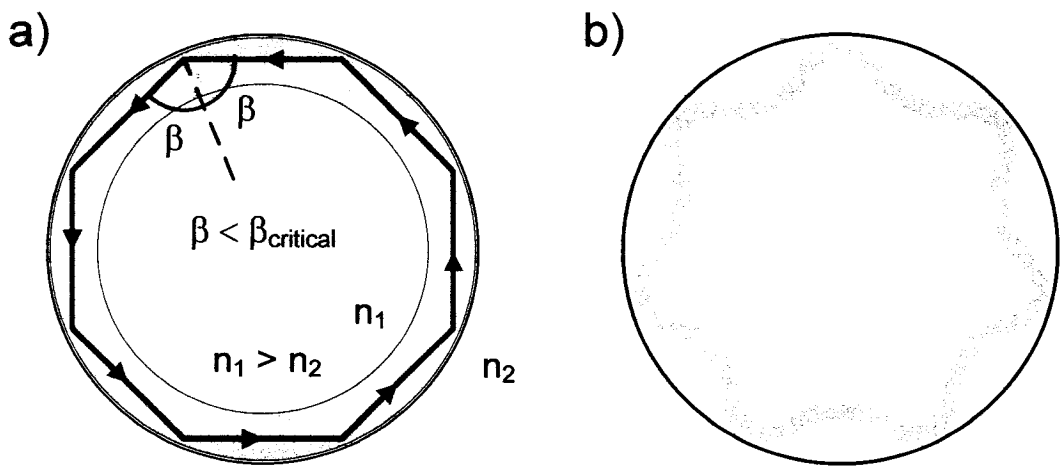

Figure 2.2 Ray optics description of optical resonances within microcavities. a) The light is confined at the interface through total internal reflection. The wavelengths completing a full trip around the circumference in phase are amplified. b) The counter-propagating waves form standing waves with greatly enhanced internal field intensities inside the microcavity.

Optical resonances can be understood via ray optics (Figure 2.2). A light wave undergoes total internal reflection at the microcavity interface when the refractive index of the microcavity is higher than the surrounding medium. The wavelengths that complete a round trip in phase are trapped within the microcavity and amplified. This process can also be interpreted through the wave nature of

† They used the term "surface waves" to describe the MDRs or WGMs in the microdroplet.

Reproduced with permission of the copyright owner. Further reproduction prohibited without permission.

light. The wavelengths corresponding to the morphology dependent resonances of the microcavity form a standing wave with highly enhanced internal field intensity.

b. Electromagnetic wave (Mie Scattering):

The MDRs of a optical microcavity can be calculated through Lorentz-Mie theory which provides the analytical solution to Maxwell's equations for the interaction of a plane electromagnetic wave incident on a homogenous dielectric sphere.[37-40] The location of the MDRs depends on the Mie size parameter x ($x = 2\pi a / \lambda$, where a is the radius of the sphere and λ is the wavelength of the resonance) and the relative complex refractive index m ($m = m_{sphere} / m_{medium}$).

Briefly, Maxwell's wave vector equation is solved in spherical coordinates through separation of variables (the incident plane wave which is originally in Cartesian coordinates is also expressed in spherical coordinates). The incident and the scattered wave satisfying Maxwell's equations are expressed in vector spherical harmonics. The internal field $r < a$ (due to scattered wave inside the microcavity) and the external field $r \geq a$ (due to incident wave and scattered wave outside the microcavity) are matched at the surface of the microcavity as the boundary condition.

Starting with the Maxwell equations:

$$\begin{aligned} \nabla \bullet \mathbf{E} &= 0 \\ \nabla \bullet \mathbf{H} &= 0 \\ \nabla \times \mathbf{E} &= i\omega\mu\, \mathbf{H} \\ \nabla \times \mathbf{H} &= -i\omega\varepsilon\, \mathbf{E} \end{aligned} \qquad \textbf{(2.1)}$$

and defining $k^2 \equiv \omega^2 \varepsilon \mu$ as the wavenumber and $m(\mathbf{r})$ as the refractive index profile the vector wave equations will be:

Reproduced with permission of the copyright owner. Further reproduction prohibited without permission.

$$\nabla^2\mathbf{E} + m^2(\mathbf{r})k^2\mathbf{E} = 0$$
$$\nabla^2\mathbf{H} + m^2(\mathbf{r})k^2\mathbf{H} = 0 \qquad \textbf{(2.2)}$$

The initial plane wave can be expressed in vector spherical harmonics as:

$$\mathbf{E}_{incident} = \sum_{n=0}^{\infty}\sum_{m=-l}^{l}(B_{nm}^{\varepsilon}\mathbf{M}_{nm}^{\varepsilon} + B_{nm}^{o}\mathbf{M}_{nm}^{o} + A_{nm}^{\varepsilon}\mathbf{N}_{nm}^{\varepsilon} + A_{nm}^{o}\mathbf{N}_{nm}^{o}) \qquad \textbf{(2.3)}$$

where $\mathbf{M}_{nm}$ and $\mathbf{N}_{nm}$ are the transverse electric (TE) modes and the transverse magnetic (TM) modes respectively. If the plane wave is polarized in the x-direction and moving along the z-axis, then only m = 1 contributes, so the expansion becomes

$$\mathbf{E}_{incident} = \sum_{n=0}^{\infty} i^n \frac{2n+1}{n(n+1)}\left[\mathbf{M}_{o1}^{(1)} - i\mathbf{N}_{e1}^{(1)}\right] \qquad \textbf{(2.4)}$$

in spherical coordinates the TE and the TM modes are expressed as:

$$\mathbf{M}_{n1}(r,\theta,\phi) = \frac{e^{i\phi}}{kr}S_n\mathbf{X}_{n1}(\theta),$$
$$\mathbf{N}_{n1}(r,\theta,\phi) = \frac{e^{i\phi}}{k^2m^2(r)}\left[\frac{1}{r}\frac{\partial C_n(r)}{\partial r}\mathbf{Y}_{n1}(\theta) + \frac{1}{r^2}C_n(r)\mathbf{Z}_{n1}(\theta)\right], \qquad \textbf{(2.5)}$$

The angular functions $\mathbf{X}_{n1}, \mathbf{Y}_{n1}$ and $\mathbf{Z}_{n1}$ are defined as:

$$\mathbf{X}_{n1}(\theta) = i\pi_{n1}(\theta)\hat{\mathbf{e}}_\theta - \tau_{n1}(\theta)\hat{\mathbf{e}}_\phi,$$
$$\mathbf{Y}_{n1}(\theta) = \tau_{n1}(\theta)\hat{\mathbf{e}}_\theta - i\pi_{n1}(\theta)\hat{\mathbf{e}}_\phi, \qquad \textbf{(2.6)}$$
$$\mathbf{Z}_{n1}(\theta) = n(n+1)P_n^{(1)}(\cos\theta)\hat{\mathbf{e}}_r,$$

where

$$\pi_{n1}(\theta) = \frac{m}{\sin\theta}P_n^{(1)}(\cos\theta),$$
$$\tau_{n1}(\theta) = \frac{\partial}{\partial\theta}P_n^{(1)}(\cos\theta), \qquad \textbf{(2.7)}$$

Reproduced with permission of the copyright owner. Further reproduction prohibited without permission.

$P_n^{(1)}(\cos\theta)$ is the associated Legendre polynomial and $\hat{e}_\theta, \hat{e}_\phi, \hat{e}_r$ are the unit orthogonal vectors associated with spherical coordinates. The functions $S_n(r)$ and $C_n(r)$ are the radial Debye potentials which satisfy:

$$\begin{aligned} &\frac{d^2S_n(r)}{dr^2} + \left[k^2m^2(r) - \frac{n(n+1)}{r^2}\right]S_n(r) = 0, \\ &\frac{d^2C_n(r)}{dr^2} - \frac{2}{m(r)}\frac{dm(r)}{dr}\frac{dC_n(r)}{dr} + \left[k^2m^2(r) - \frac{n(n+1)}{r^2}\right]C_n(r) = 0, \end{aligned} \tag{2.8}$$

$S_n(0) = 0$ and $C_n(0) = 0$ to ensure that the electric field is finite at the origin.

Assuming a homogenous optical microcavity, we will have $m(\mathbf{r}) = m$ (constant) inside the cavity $(r < a)$, then the two equations in (2.8) will essentially be the same and the Ricatti-Bessel functions are the linearly independent solutions:

$$\begin{aligned} &u_{internal}(r) = c_n\chi_n(mkr) + d_n\psi_n(mkr), \quad \text{where} \\ &\psi_n(mkr) = mkr\, j_n(mkr), \\ &\chi_n(mkr) = mkr\, n_n(mkr), \end{aligned} \tag{2.9}$$

and $j_n(mkr)$ and $n_n(mkr)$ are spherical Bessel functions of the first kind and second kind respectively.

Outside the optical cavity $(r \geq a)$, where $m(\mathbf{r}) = 1$, the solutions are linear combinations of Riccati-Bessel functions, so we write it as:

$$u_{scattering}(r) = a_n\chi_n(kr) + b_n\psi_n(kr), \tag{2.10}$$

Essentially, the solutions for the radial equations for the Debye potentials in (2.8) are spherical Bessel functions. The incident wave as well as the scattered wave and the internal wave can be expressed in terms of linear combinations of the spherical Bessel functions with two independent coefficients. The scattered

Reproduced with permission of the copyright owner. Further reproduction prohibited without permission.

wave will contribute a_n and b_n and the internal wave will contribute c_n and d_n. These coefficients are solved by applying the boundary conditions at the interface of the microcavity.

The boundary conditions require that the transverse components of the total electric and magnetic fields should be equal to zero at the microcavity surface. This means that the sum of the incident and scattered fields (outside the microcavity) should be equal to the interior field (inside the microcavity).That is:

$$\begin{aligned} \mathbf{n}\times\left(\mathbf{H}_{\text{cavity}}-\mathbf{H}_{\text{medium}}\right)=0 \\ \mathbf{n}\times\left(\mathbf{E}_{\text{cavity}}-\mathbf{E}_{\text{medium}}\right)=0 \end{aligned} \qquad \textbf{(2.11)}$$

Thus we get the coefficients for the internal wave (inside the microcavity) and scattered wave (outside the microcavity):

$$\begin{aligned} a_n &= \frac{\psi_n(x)\psi_n'(mx)-m\psi_n(mx)\psi_n'(x)}{\zeta_n(x)\psi_n'(mx)-m\psi_n(mx)\zeta_n'(x)}, \\ b_n &= \frac{m\psi_n(x)\psi_n'(mx)-\psi_n(mx)\psi_n'(x)}{m\zeta_n(x)\psi_n'(mx)-\psi_n(mx)\zeta_n'(x)}, \\ c_n &= \frac{-im}{\zeta_n(x)\psi_n'(mx)-m\psi_n(mx)\zeta_n'(x)}, \\ d_n &= \frac{-im}{m\zeta_n(x)\psi_n'(mx)-\psi_n(mx)\zeta_n'(x)}, \end{aligned} \qquad \textbf{(2.12)}$$

a_n and b_n are the scattering, c_n and d_n are the internal coefficients ($\zeta_n=\psi_n-i\chi_n$). Note that the denominators of the a_n and c_n are identical to those of the b_n and d_n respectively.

Optical resonances correspond to the size and refractive index conditions which make the denominators of these coefficients vanish or get very small. In other words, optical resonances in a microcavity correspond to the poles

Reproduced with permission of the copyright owner. Further reproduction prohibited without permission.

of the partial wave expansion coefficients. In this case both the internal and the scattered fields are amplified.

For a certain MDR, the Mie size parameter ($x = 2\pi a/\lambda$) decreases, if the refractive index decreases; similarly the size parameter increases if the radius increases. Therefore, a blue shift in the output resonance is observed when the radius of the microcavity decreases. This could be due to evaporation for a microdroplet. A blue shift in the MDR can also be associated with a decrease in refractive index. This could be due to a temperature increase in the microcavity.

c. Quantum mechanics (Bohr Atom analogy):

Some features of MDRs cannot be explained solely on the basis of classical physics. The line width of the resonances cannot be determined from Mie's theory for example. A higher level description that makes use of quantum mechanics is required. The analogy to quantum mechanics rests on the similarity between the Schrodinger equation and the Helmholtz equation to which Maxwell's equations often reduce.[41] Starting with the Schrodinger equation:

$$\begin{aligned} &\mathbf{H}\Psi = E\Psi, \\ &\mathbf{H} \equiv \frac{\mathbf{p}^2}{2m} + V(\mathbf{r}) = -\frac{-\hbar^2}{2m}\nabla^2 + V(\mathbf{r}), \quad \text{with} \quad \mathbf{p} \equiv -i\hbar\nabla, \\ &\left[\frac{-\hbar^2}{2m}\nabla^2 - (V(\mathbf{r}) - E)\right]\Psi(\mathbf{r}) = 0 \end{aligned} \tag{2.13}$$

The solution through separation of variables will involve:

$$\begin{aligned} &\Psi(\mathbf{r}) \equiv \Psi(r,\theta,\phi) = R(r)\Theta(\theta)\Phi(\phi) = R(r)Y(\theta,\phi), \\ &\nabla^2 \equiv \frac{1}{r^2\sin\theta}\left[\sin\theta\frac{\partial}{\partial r}\left(r^2\frac{\partial}{\partial r}\right) + \frac{\partial}{\partial\theta}\left(\sin\theta\frac{\partial}{\partial\theta}\right) + \frac{1}{\sin\theta}\frac{\partial^2}{\partial\phi^2}\right] \end{aligned} \tag{2.14}$$

We obtain three partial differential equations for the three coordinates:

Reproduced with permission of the copyright owner. Further reproduction prohibited without permission.

$$
\begin{aligned}
&\text{For } r: \quad \frac{1}{\mathrm{R}}\frac{d}{dr}\left[r^2\frac{dR}{dr}\right]+\frac{2mr^2}{\hbar^2}\big(E-V(r)\big)\equiv \ell(\ell+1),\\
&\text{For } \phi: \quad \frac{1}{\Phi}\frac{d^2\Phi}{d\phi^2}\equiv -m_\ell{}^2,\\
&\text{For } \theta: \quad \frac{\mathrm{Sin}\theta}{\Theta}\frac{\mathrm{d}}{\mathrm{d}\theta}\left[\sin\theta\frac{d\Theta}{d\theta}\right]=m_\ell{}^2\sin^2\theta-\ell(\ell+1),
\end{aligned}
\tag{2.15}
$$

and the normalized solutions for Hydrogen atom will be:

$$
\begin{aligned}
&R_{n,\ell}(\alpha r)=\sqrt{\left(\frac{2}{na_0}\right)^3\frac{(n-\ell-1)!}{2n\big[(n+\ell)!\big]}}\;(\alpha r)^\ell\;e^{-(\alpha r)/2}\;L_{n-\ell-1}^{2\ell+1}(\alpha r),\\
&\Theta_{\ell,m_\ell}(\theta)=\sqrt{\frac{(2\ell+1)(\ell-m_\ell)!}{2(\ell+m_\ell)!}}\;P_\ell^{m_\ell}(\cos\theta)\ \text{and}\ \Phi_{m_\ell}(\phi)=\frac{1}{\sqrt{2\pi}}e^{im_\ell\phi},\\
&\text{or } Y_{\ell,m_\ell}(\theta,\phi)=\sqrt{\frac{(2\ell+1)(\ell-m_\ell)!}{4\pi(\ell+m_\ell)!}}\;P_\ell^{m_\ell}(\cos\theta)\;e^{im_\ell\phi},
\end{aligned}
\tag{2.16}
$$

where n,ℓ,m_ℓ are principal quantum number, orbital quantum number and magnetic quantum number respectively.

$$
\begin{aligned}
&n=1,2,3,\ \ldots\ldots \text{ integers};\\
&\ell=0,1,2,3\ \ldots\ldots\ n-1;\\
&m_\ell=-\ell,-\ell+1,\ \ldots\ 0\ \ldots\ \ell-1,\ell;
\end{aligned}
\tag{2.17}
$$

However, we can approach the same problem through the angular momentum operator $\mathbf{L}=\ \mathbf{r}\times\mathbf{p}\equiv r\times\left(\text{-i}\hbar\nabla\right)=\text{-i}\hbar\left(r\times\nabla\right)$. In spherical coordinates:

$$
\begin{aligned}
&\mathbf{L}^2=-\hbar^2\left[\frac{1}{\sin\theta}\frac{\partial}{\partial\theta}\left(\sin\theta\frac{\partial}{\partial\theta}\right)+\frac{1}{\sin^2\theta}\frac{\partial^2}{\partial^2\phi}\right],\\
&L_z=-i\hbar\frac{\partial}{\partial\phi},
\end{aligned}
\tag{2.18}
$$

If we carefully compare $\mathbf{L}^2$ and (2.15), we will see that $\mathbf{L}^2$ is related to the non-radial part of the Hamiltonian after separation of variables. Indeed we can show that

Reproduced with permission of the copyright owner. Further reproduction prohibited without permission.

$$\mathbf{L}^2 Y_{\ell,m_\ell}(\theta,\phi) = \ell(\ell+1)\hbar^2 Y_{\ell,m_\ell}(\theta,\phi);$$
$$L_z Y_{\ell,m_\ell}(\theta,\phi) = m_\ell \hbar Y_{\ell,m_\ell}(\theta,\phi) \qquad \textbf{(2.19)}$$

Using (2.14) and (2.18), we can rewrite the Hamiltonian:

$$\nabla^2 \equiv \frac{1}{r^2 \sin\theta}\left[\sin\theta \frac{\partial}{\partial r}\left(r^2 \frac{\partial}{\partial r}\right) + \frac{\partial}{\partial \theta}\left(\sin\theta \frac{\partial}{\partial \theta}\right) + \frac{1}{\sin\theta}\frac{\partial^2}{\partial \phi^2}\right] \text{ and,}$$
$$\mathbf{L}^2 = -\hbar^2\left[\frac{1}{\sin\theta}\frac{\partial}{\partial\theta}\left(\sin\theta\frac{\partial}{\partial\theta}\right) + \frac{1}{\sin^2\theta}\frac{\partial^2}{\partial^2\phi}\right], \text{ then we have;}$$
$$\mathbf{L}^2 = -\hbar^2\left[r^2\nabla^2 - \frac{\partial}{\partial r}\left(r^2\frac{\partial}{\partial r}\right)\right], \text{ if we write } \nabla^2 \text{ in terms of } \mathbf{L}^2 : \qquad \textbf{(2.20)}$$
$$\nabla^2 = \frac{1}{r^2}\left[\frac{\partial}{\partial r}\left(r^2\frac{\partial}{\partial r}\right) - \frac{\mathbf{L}^2}{\hbar^2}\right];$$

and we obtain:

$$\mathbf{H} = -\frac{\hbar^2}{2m}\nabla^2 + V(\mathbf{r}) = -\frac{\hbar^2}{2m}\frac{1}{r^2}\left[\frac{\partial}{\partial r}\left(r^2\frac{\partial}{\partial r}\right) - \frac{\mathbf{L}^2}{\hbar^2}\right] + V(\mathbf{r});$$
$$\mathbf{H} = -\frac{\hbar^2}{2mr^2}\frac{\partial}{\partial r}\left(r^2\frac{\partial}{\partial r}\right) + \frac{\mathbf{L}^2}{2mr^2} + V(\mathbf{r}); \qquad \textbf{(2.21)}$$

Now, considering the Schrodinger equation again:

$$\mathbf{H}\Psi = E\Psi,$$
$$\left[-\frac{\hbar^2}{2mr^2}\frac{\partial}{\partial r}\left(r^2\frac{\partial}{\partial r}\right) + \frac{\mathbf{L}^2}{2mr^2} + V(\mathbf{r})\right]\Psi(\mathbf{r}) = E\Psi(\mathbf{r}); \qquad \textbf{(2.22)}$$

only $\mathbf{L}^2$ will be affecting the non-radial part of $\Psi(r,\theta,\phi) = R(r)Y_{\ell,m_\ell}(\theta,\phi)$. So we get:

$$\left[-\frac{\hbar^2}{2mr^2}\frac{\partial}{\partial r}\left(r^2\frac{\partial}{\partial r}\right) + \frac{\ell(\ell+1)\hbar^2}{2mr^2} + V(r)\right]R(r) = ER(r) \qquad \textbf{(2.23)}$$

If we define $u(r) = r\ R(r)$, then the equation simplifies as:

Reproduced with permission of the copyright owner. Further reproduction prohibited without permission.

$$-\frac{\hbar^2}{2m}\frac{d^2u}{dr^2}+\left[\frac{\ell(\ell+1)\hbar^2}{2mr^2}+V(r)\right]u(r)=Eu(r) \qquad \textbf{(2.24)}$$

So the 3-D Schrodinger equation is reduced down to 1-D with:

$$H=-\frac{\hbar^2}{2m}\frac{d^2}{dr^2}+V_{eff} \quad \text{with} \quad V_{eff}=\frac{\ell(\ell+1)\hbar^2}{2mr^2}+V(r) \qquad \textbf{(2.25)}$$

The first term in V_{eff} is often called "centrifugal potential". The solution of $u(r)$ for a free particle $V(r)=0$ will be:

$$R(r)=Cj_\ell(kr) \qquad \textbf{(2.26)}$$

which is simply the spherical Bessel function. As a result, the 3-D Schrodinger equation can be divided into radial and non-radial parts where the angular momentum operator provides the solution for the non-radial part.

Now; going back to our original problem (i.e. the scattering of a plane wave from a spherical cavity), starting with the Helmholtz equation for $\mathbf{E}$ in (2.2) and defining the Laplacian in terms of an "angular momentum" operator, we get:

$$\begin{aligned}&\nabla^2\mathbf{E}+m^2(\mathbf{r})k^2\mathbf{E}=0,\\&\nabla^2=\frac{1}{r^2}\left[\frac{\partial}{\partial r}\left(r^2\frac{\partial}{\partial r}\right)-\frac{\mathbf{L}^2}{\hbar^2}\right],\\&\left[\frac{1}{r^2}\left[\frac{\partial}{\partial r}\left(r^2\frac{\partial}{\partial r}\right)-\frac{\mathbf{L}^2}{\hbar^2}\right]+m^2(\mathbf{r})k^2\right]\mathbf{E}=0\end{aligned} \qquad \textbf{(2.27)}$$

Similarly, with the assumptions $\mathbf{E}=\mathbf{L}\psi$, $\psi(r,\theta,\phi)=R(r)Y_{\ell,m_\ell}(\theta,\phi)$ and $u(r)=r\,R(r)$; $\mathbf{L}^2$ will reduce the 3-D equation into a 1-D radial equation:

$$\begin{aligned}&\frac{d^2u}{dr^2}+\left(k^2-V_{eff}\right)u=0,\\&V_{eff}=k^2\left(1-m^2(r)\right)+\frac{\ell(\ell+1)}{r^2}\end{aligned} \qquad \textbf{(2.28)}$$

Reproduced with permission of the copyright owner. Further reproduction prohibited without permission.

where the first term in the effective potential confines the light in the microcavity and the second term, the centrifugal term is repulsive. For a spherical particle of diameter a with a constant refractive index m, the effective potential will be:

$$V_{eff} = \begin{cases} k^2\left(1-m^2\right)+\dfrac{\ell(\ell+1)}{r^2} & \mathrm{r} \le \mathrm{a} \\ \dfrac{\ell(\ell+1)}{r^2} & \mathrm{r} \le \mathrm{a} \end{cases} \qquad \textbf{(2.29)}$$

Figure 2.3 shows V_{eff} for a particle with radius a, refractive index $m = 1.47$ and wavenumber $k = 33/a$. Here the dashed line represents the total energy in the system. Therefore, classically only the region $r_1 < r < a$ is allowed since the potential energy is smaller than the total energy of the system allowing a positive value for the kinetic energy.

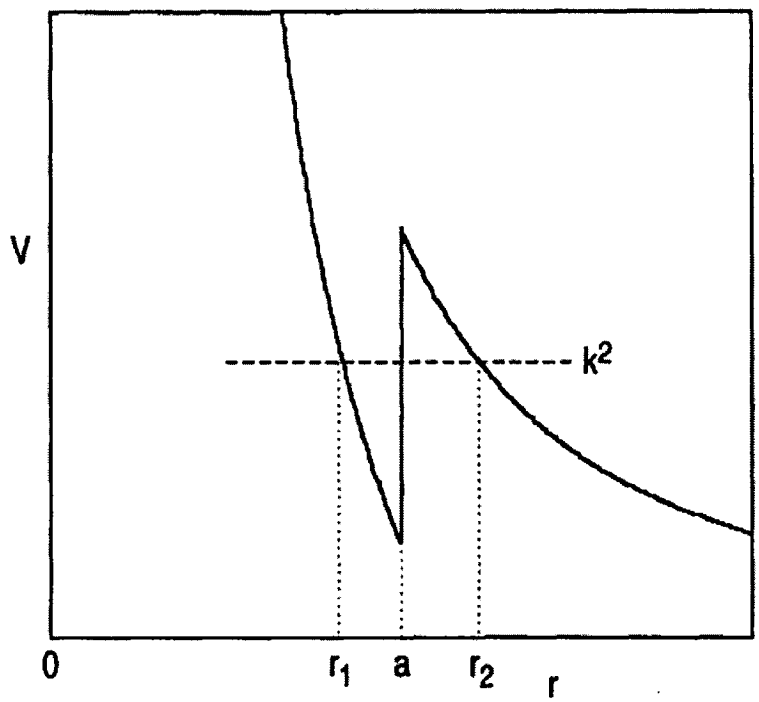

Figure 2.3 Effective potential for the photonic atom model of a spherical particle. Radius a, m=1.47 and k=33/a. (Adopted from Johnson et al., J. Opt. Soc. Am. A (1993))

Reproduced with permission of the copyright owner. Further reproduction prohibited without permission.

An optical resonance can be interpreted as a quasi-bound state temporarily trapped in a potential well. The optical resonance can tunnel through the energy barrier into the classically forbidden regions outside the potential well with exponential decay behavior. The resonances corresponding to low energy levels in the potential well should overcome a larger barrier, therefore should exhibit a longer lifetime and a narrow resonance width.[42]

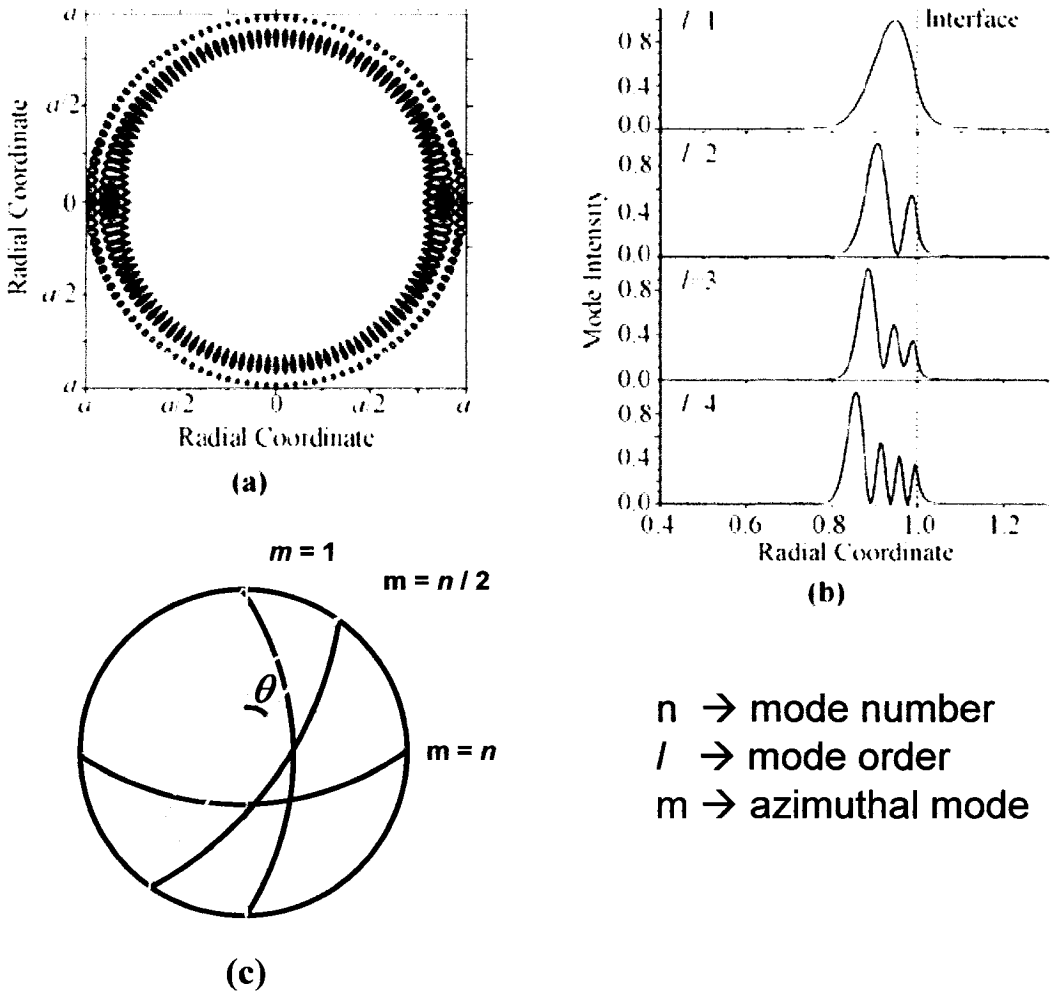

Figure 2.4 Photonic atom model of optical resonances in microcavities. (a) Internal intensity distribution of an optical resonance with $n = 60$ and $\ell = 2$ calculated for a droplet of size parameter 53.3130188. (b) Influence of mode order on radial field. (c) Orientation of different degenerate azimuthal modes in a spherical droplet. (Adopted from Symes et al., Phys. Chem. Chem. Phys. (2004))

Reproduced with permission of the copyright owner. Further reproduction prohibited without permission.

The solution to the Helmholtz equation for the field inside the optical microcavity will give rise to quantized states as it did for the solutions of the hydrogen atom problem in equations (2.16) and (2.17). The physical interpretation of the quantum numbers for the optical resonances is depicted in Figure 2.4.

The angular variation in the internal field intensity is described by n, the mode number. In the classical picture, this integer number corresponds to the number of reflections that the wave undergoes due to total internal reflection at the microcavity interface.

The mode order number, ℓ, indicates the number of radial maxima for a specific mode. For higher mode orders, the resonances extend into the inner regions of the microcavity by a fraction of the cavity radius ($r \approx a/m$ from the center, where a is the cavity radius and m is the relative refractive index). In the classical picture, this corresponds to the closest ray to the center that still goes through total internal reflection inside the microcavity. Figure 2.4 (b) shows the exponential decay component extending out of the microcavity. This is the evanescent wave tunneling through the potential well into the classically forbidden regions. Coupling external optical resonances (input resonances) is possible through evanescent wave excitation. This is not possible according to geometric optics since a light wave (entering into a spherical or cylindrical microcavity with higher refractive index compared to its surrounding) cannot be confined through total internal reflection as it will exit the microcavity with the same incident angle.

Azimuthal mode number, m, represents the $2n+1$ azimuthal mode degeneracy as shown in Figure 2.4 (c).

Reproduced with permission of the copyright owner. Further reproduction prohibited without permission.

For each mode number n, and mode order number ℓ, there exists a TE and TM mode. Chýlek et al. calculated the approximate distances between the two resonances of successive modes with the same order (ℓ) and polarization (TE or TM).[43, 44]

$$\Delta\lambda \approx \frac{\lambda^2 \tan^{-1}\left[m^2-1\right]^{1/2}}{2\pi a\left[m^2-1\right]^{1/2}} \qquad \textbf{(2.30)}$$

This formula implies that for a longer (shorter) wavelength and a smaller (larger) cavity radius, the distance between successive modes increases (decreases), which are intuitively verified through classical ray optics approach.

It is possible to determine the size, the refractive index and the dispersion of a microcavity with tremendous precision through the optical resonances[45-48]. To do this, initially the experimentally observed resonances are assigned to theoretical resonance locations usually obtained through Mie scattering calculations. Then equation (2.30) is used to deduce the size, the refractive index or dispersion one at a time by observing the shift in the optical resonance peak locations with the corresponding change in the parameter to be measured. The refractive index can be measured with a precision of one part in 10^5 and size can be measured with a precision of one part in 10^5 (corresponding to 0.1 A° change in size !!!) for a small microcavity.[48] This extreme precision, of course, is the basis for utilization of optical resonances for detection of atomic or molecular layers of chemical and biological agents in gas as well as liquid media.

An interesting demonstration of the analogy between the optical resonances with the quantum mechanical states is shown by Mukaiyama et al.[49] The authors placed two nearly identical fluorescent microspheres together and re-

Reproduced with permission of the copyright owner. Further reproduction prohibited without permission.

corded the splitting in optical modes similar to the splitting of electronic states in a diatomic molecule. In other words, the researchers formed a photonic molecule.

2. Q-factor

The definition of Q-factor is:

$$Q = \frac{2\pi \times \text{Energy stored}}{\text{Energy lost per cycle}} = \frac{\omega_0}{\gamma} = \omega_0 \tau \qquad \textbf{(2.31)}$$

where ω_0 is the resonance frequency, γ is the linewidth (FWHM) of the resonant peak τ is the lifetime of the oscillation. A resonator has a high Q-factor if the resonance frequency (proportional to the energy stored) is high, and the linewidth is very narrow (minimal energy dissipation). The highest Q-factor[50] in optical systems is observed in silica microspheres at Q = 2 x 10^9. The high finesse allows the light to be confined within the microcavity up to microseconds which corresponds to several million trips around the rim.

Absorption and scattering cause significant degradation of Q-factor and are the main reasons for (several orders of magnitude) obtaining low experimental Q-factor values compared to the possible theoretical limits. The absorption and scattering can be formulated into the Q-factor formula as:

$$\frac{1}{Q} = \frac{1}{Q_0} + \frac{1}{Q_{abs}} + \frac{1}{Q_{leak}} \qquad \textbf{(2.32)}$$

The leakage term would affect the mode visibility and the absorption term would affect the threshold for the stimulated processes like lasing and stimulated Raman scattering.

Q-factors for optical resonances increase with increasing mode numbers and decreasing mode orders.

Reproduced with permission of the copyright owner. Further reproduction prohibited without permission.

B. Lasing in microcavities

Although optical resonances in microcavities were first observed through light scattering[36, 51]; fluorescence[52] and Raman scattering[53, 54] were later shown to support such resonances as well.

The first experimental observation of lasing from liquid microcavities was reported by Tzeng et al. in 1984.[55, 56] They observed sharp peaks at specific wavelengths that were commensurate with the morphology dependent resonances of a 60 micron ethanol droplet doped with Rhodamine 6G dye. The resonance peaks were superimposed on the broad fluorescence emission of Rhodamine 6G and the intensity of the peaks increase nonlinearly with the pump laser power which is quite typical for lasing.

To achieve lasing, three requirements need to be satisfied: A pump source, a gain medium and an optical cavity. The comparison between a conventional laser and the lasing action in a liquid microcavity is given in Table 2.1

Table 2.1 Analogy between conventional lasers and liquid microcavity lasing.

	Conventional laser	*Liquid microcavity lasing*
Pump source	A flash lamp or another laser (pump laser)	Laser (Nd:YAG or Argon ion laser)
Gain medium	A solid state rod (e.g. Nd:YAG) or a gas medium (e.g. Argon ion)	Fluorescent dyes or Quantum Dots
Optical cavity	Highly reflective mirrors	Liquid microcavity (microdroplet) with total internal reflection

If a specific incident wavelength is coupled to the MDRs in a microcavity, these are called "input resonances". The evanescently coupled laser light can only match the resonance conditions of a microcavity with certain size parameter

Reproduced with permission of the copyright owner. Further reproduction prohibited without permission.

and cavity shape. Since the homogenous linewidth of conventional lasers are extremely narrow, the possibility of coupling into an input resonance is slim.

When the wavelengths that satisfy MDR conditions are internally generated through inelastic scattering or any stimulated emission process, these are called "output resonances". Especially, if the internal radiation is due to an organic dye, the emission has a broad linewidth and it is quite common to attain at least several wavelengths that match the resonance conditions for a microcavity of certain size and shape.

For a liquid microcavity doped with an organic dye or a quantum dot, laser emission (output resonances) will be based on the fluorescence emission. Certain wavelengths that satisfy the MDR conditions will be amplified within the microcavity. Laser emission is expected when the gain for the round-trip of an output resonance is larger than the round-trip loss resulting from optical absorption and radiation leakage from the droplet. The optical absorption is mainly due to the self-quenching of the fluorescent dye. The loss mechanism will be dominant at the wavelengths where the overlap between the absorption spectrum and the emission spectrum is significant. The gain increases at longer wavelengths of the emission where the overlap with the absorption spectrum is low. Therefore, the lasing emission occurs at longer wavelengths (red-shifted) compared to the emission peak of the fluorescent dye. The radiation leakage is usually due to the shape distortions (imperfections in the microcavity shape) or inclusions (defects) that causes scattering.

Since the optical resonances are a result of the boundary conditions (which depend on the relative refractive index, shape and size), the position of the

Reproduced with permission of the copyright owner. Further reproduction prohibited without permission.

resonances for elastic (e.g. Rayleigh scattering) or inelastic scattering (e.g. fluorescence, Raman scattering) can be determined through Lorentz-Mie theory.

C. FRET in microcavities

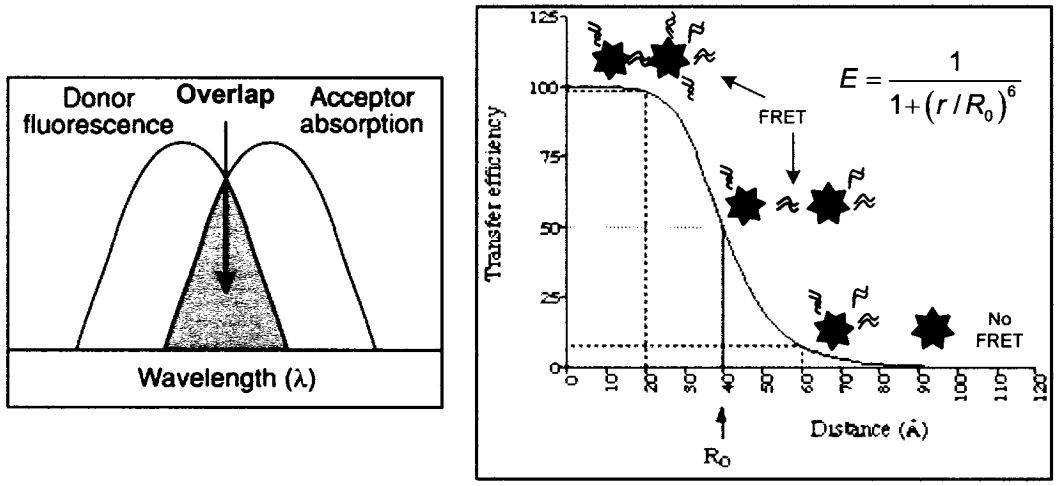

R_0 : Förster radius, 50% energy transfer efficiency distance (2-10 nm)

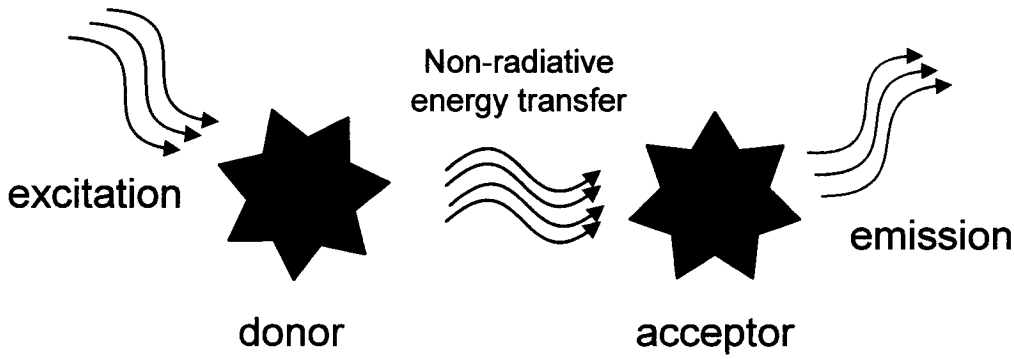

Figure 2.5 Overview of Fluorescence Resonance Energy Transfer (FRET). FRET is the non-radiative energy transfer between two fluorescent molecules in close proximity. The energy transfer efficiency is inversely dependent on the sixth power of distance between the two molecules. The emission spectrum of the donor and the absorption spectrum of the acceptor should overlap.

Fluorescence (Förster) Resonance Energy Transfer (FRET) is a non-radiative energy transfer mechanism[57] that occurs between two fluorescent molecules (a donor and an acceptor molecule) through resonant dipole-dipole interaction. When a fluorescent molecule is exposed to photons at a specific

Reproduced with permission of the copyright owner. Further reproduction prohibited without permission.

wavelength (within its absorption spectrum), the electronic states of the molecule are excited through the absorption of the photons. These excited states usually relax to the ground state through the emission of photons with longer wavelength (Stokes-shifted) compared to the excitation.

If an excited fluorescent molecule has another fluorescent molecule within close proximity (2-10 nm), the relaxation of the electronic states can happen through non-radiative energy transfer to this neighboring fluorescent molecule. In this case, the second fluorescent molecule (absorbing the transfer energy) becomes excited and consequently relaxes through emission of photons.

The fluorescent molecule which is initially excited through light and relaxes without emission of photons is called the "donor" molecule. The second fluorescent molecule which is excited through the resonant energy transfer from the donor molecule is called the "acceptor" molecule. For efficient energy transfer, the emission spectrum of the donor molecule and the absorption spectrum of the acceptor molecule should overlap extensively. Figure 2.5 explains the basics of the FRET process:

The FRET efficiency is determined by three parameters:

1. The distance between the donor and the acceptor.
2. The spectral overlap of the donor emission spectrum and the acceptor absorption spectrum.
3. The relative orientation of the donor emission dipole moment and the acceptor absorption dipole moment.

FRET efficiency can be formulated as follows:

Reproduced with permission of the copyright owner. Further reproduction prohibited without permission.

$$E = \frac{1}{1+(r/R_0)^6} \equiv 1 - \frac{I_d^a}{I_d} \qquad \textbf{(2.33)}$$

where R_0 is the Förster radius defined as the distance between the fluorescent dyes with 50% FRET efficiency. I_d^a is the intensity from the donor molecule in the presence of acceptor and I_d is the intensity from the donor molecule in the absence of acceptor. In practice, the FRET efficiency (as in (2.33)) is calculated by measuring the ratio of the intensity of donor emission in the presence and absence of the acceptor molecule. As FRET efficiency increases, the emission from the donor molecule decreases and the emission from the acceptor molecule increases due to the resonance energy transfer from the donor molecule.

The transfer efficiency depends inversely on the sixth power of the distance between the donor and the acceptor molecule leading to a powerful nanoscale (2-10 nm) measurement technique. Therefore, FRET is often referred to as a "spectroscopic ruler".

FRET is also related to the fluorescence lifetime of the donor and acceptor molecule. As FRET efficiency increases, the fluorescence lifetime of the donor decreases. For that reason, FRET efficiencies can also be calculated through lifetime measurements of the donor molecule in the presence and absence of an acceptor molecule.

There are many fluorescent dyes which can be used as efficient FRET pairs. The transfer efficiencies for a wide variety of fluorescent dyes have been studied. Non-fluorescent quenchers such as QSY can also be used as efficient acceptors (donors) because of their availability in a wide spectrum range and the absence of any intrinsic fluorescence emission.

Reproduced with permission of the copyright owner. Further reproduction prohibited without permission.

FRET can be used to measure intramolecular distances for biological molecules in studying protein-protein and protein-DNA interactions, and protein conformational changes. FRET can also be utilized to detect binding reactions such as enzymatic reactions and immunoassays.

When a FRET pair is located in a microcavity, the energy transfer process is enhanced as the cavity quantum electrodynamics plays a role in spontaneous and stimulated emission. The spontaneous emission transition rate can be enhanced in a microcavity by a factor of

$$f = \frac{3DQ\lambda}{4\pi^2 V} \qquad \textbf{(2.34)}$$

where Q is the quality factor, D is the mode degeneracy and V is the mode volume of the microcavity as theoretically first predicted by Purcell[58]. However this enhancement is valid if the homogenous linewidth of the emission is narrower than the linewidth (FWHM) of the WGM of the cavity.[59] Physically this means that if the lifetime of the emission is smaller than the lifetime of the resonances in a cavity, there should be no enhancement in the spontaneous emission.

In practice, spontaneous emission transition rate (or fluorescence decay rate) should not exhibit any enhancement in a microcavity for an organic fluorescent dye since the homogenous linewidth of organic dyes are much broader than WGM linewidths. For this reason, quantum dots or lanthanide nanoparticles are ideal to show the cavity enhancement or inhibition of spontaneous emission due to their narrow linewidths. Since the emission from a fluorescent dye typically overlaps several WGMs, cavity enhanced inhibition occurs at wavelengths that does not commensurate with the WGMs of the cavity as theoretically first pre-

Reproduced with permission of the copyright owner. Further reproduction prohibited without permission.

dicted by Kleppner[60]. This is indeed true for small microcavities ($< 20\mu m$) where WGMs occupy most of the microcavity volume. In this case, bulk fluorescence emission from the inner regions of the microcavity reduces down to zero through inhibited spontaneous emission which does not allow the wavelengths other than those correspond to the WGMs to leak out from the microcavity. Surprisingly, on the other hand, a size-dependent enhancement in spontaneous emission for organic fluorescent molecules (with broad linewidth) has also been shown in very small microspheres ($< 10\mu m$).[61-64]

Similar to spontaneous emission, FRET (dipole-dipole interaction) has also shown to be affected through the change in the emission rate of the donor molecules in optical microcavities.[65] Andrew et al. has done a series of experiments where they separated the donor and acceptor molecules by well-defined distances and studied the FRET efficiency in three sample optical environments: a half optical cavity, a full optical cavity (with various cavity sizes), and a non-cavity environment for control. By monitoring the fluorescence lifetime of the donor molecule, they concluded that resonant energy transfer (dipole-dipole) is enhanced for small donor-acceptor separations.

Radiative energy transfer is also enhanced in an optical microcavity. In a radiative energy transfer process, a photon rather than a dipole-dipole interaction mediates the energy transfer from the donor molecule to the acceptor molecule. Since a photon is involved, the energy transfer happens in the far-field; the distance between the donor and the acceptor molecule can be larger than in a dipole-dipole interaction. A radiative energy transfer between a donor and an acceptor molecule happens in two stages in an optical microcavity.[66] Initially, spe-

Reproduced with permission of the copyright owner. Further reproduction prohibited without permission.

cific wavelengths from the donor emission are coupled to the WGMs of the microcavity. Then, the acceptor molecules are excited through these WGMs. Eventually, the emission from the acceptor molecules also are coupled to the WGMs. As a result both the donor and the acceptor emission are coupled to the resonant modes of the optical microcavity. The donor emission is damped through the absorption by the acceptor molecules. Therefore, the acceptor molecules act as absorbers and reduce the Q-factor of the cavity for donor emission. The donor emission will be lower when the acceptor molecules are present within the microcavity. In this sense, the radiative energy transfer is similar to FRET, where introducing acceptor molecules give rise to a reduction in donor emission and a corresponding increase in acceptor emission. But the distance between the donor and the acceptor molecule can be much larger – on the order of microns.[67] The radiative energy transfer efficiency within optical microcavities can be as high as 1000 times the energy transfer efficiency exhibited by conventional FRET processes. Therefore, MDR-enhanced energy transfer between a donor and an acceptor molecule can be used as a sensitive mechanism in biological and chemical sensing applications based on enzymes and immunoassays.

Reproduced with permission of the copyright owner. Further reproduction prohibited without permission.

Chapter 3

Using Optical Resonances in Microcavities for Chemical and Biological Sensing

Optical resonances in microcavities have been studied extensively due to its potential applications in photonics, quantum electrodynamics (QED), atomic, molecular and optical physics, telecommunications and chemical and biological sensing during the past two decades. Some of the potential applications are summarized in Table 3.1.

Recent studies have shown that optical resonances, often called Whispering Gallery Modes (WGMs) or Morphology Dependent Resonances (MDRs), can be used for biomolecule detection. In this chapter, the utilization of

Reproduced with permission of the copyright owner. Further reproduction prohibited without permission.

optical resonances and microresonators for chemical and biological sensing are summarized.

Table 3.1 Potential applications of optical resonances.

Application fields of optical resonances	*Examples of potential applications*
Photonics	Microlasers, Optoelectronic oscillators
Atomic, Molecular and Optical Physics	Chaos, High resolution spectroscopy (e.g. Raman)
Quantum Electrodynamics	Enhancement & inhibition of spontaneous emission
Telecommunication	Optical switching, Optical and photonic filters
Chemical and Biological sensing	Label-free sensors

The first biosensing application of optical resonances in microcavities was demonstrated by Whitten[68] et al. in 1995. In this study, antibodies specific to two different types of bacteria (E. Coli and S. Aureus) were immobilized on fluorescent beads (antibody specific to E. Coli on 10 μm beads and antibody specific to S. Aureus on 6.5 μm beads). A sample containing E. Coli and S. Aureus was stained and incubated with a mixture of beads conjugated with the appropriate antibodies. Then, the beads with bound microorganisms were identified (with the help of staining) by fluorescence microscopy and the size of the beads (microspheres) was deduced from the optical resonances in the fluorescence emission from the beads. Since a bead with specific size was conjugated to a specific antibody, the type of bound microorganism was determined by the detection of bead size. By this method, the microorganisms were detected in an indirect format. The main detection was done by fluorescence microscopy. The optical resonances were utilized to determine the size of the beads; which, in turn, identifies the type of organism that is bound to the bead.

Reproduced with permission of the copyright owner. Further reproduction prohibited without permission.

The most remarkable utilization of optical resonances coupled to a microcavity for biosensing applications was described by the pioneering work of Vollmer et al.[34] The optical resonances of a microcavity (spheroid-shaped melted fiber tip) were excited through evanescent wave coupling by an eroded fiber located within close proximity to the microcavity. (Figure 3.1)

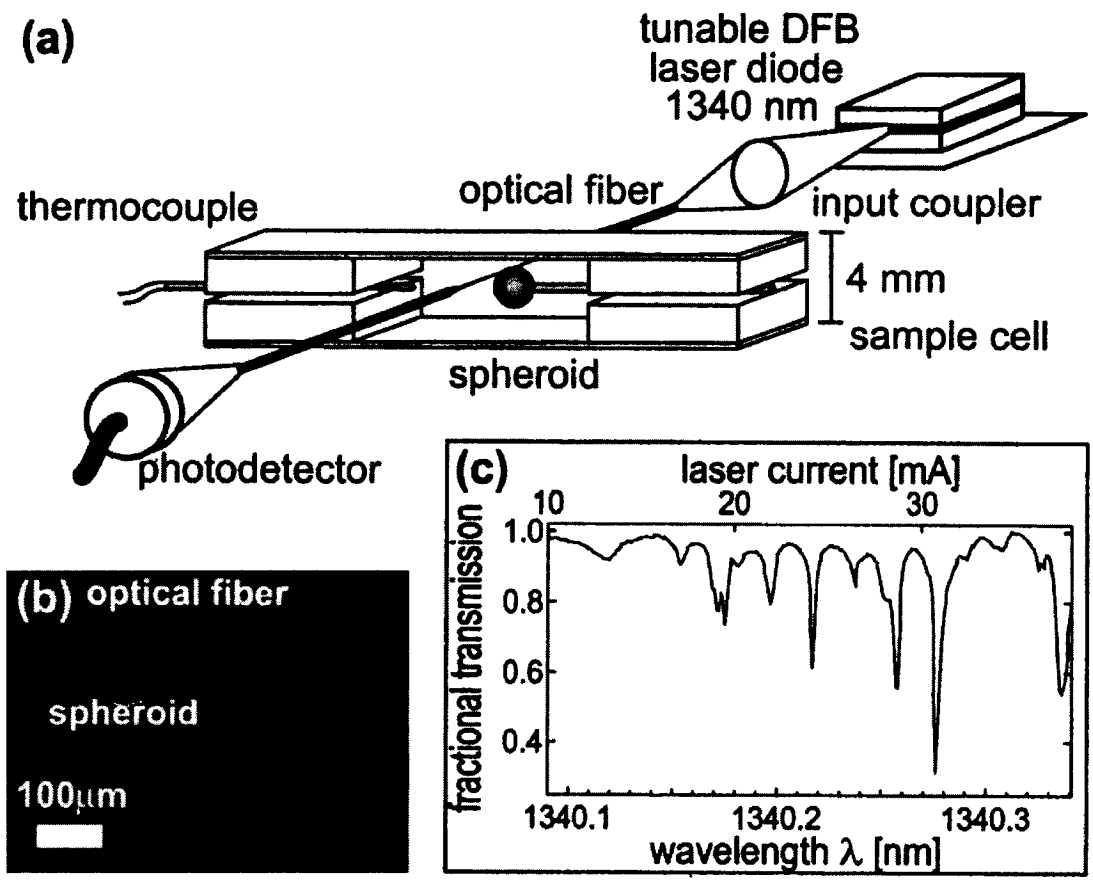

Figure 3.1 Biosensing with a spheroid optical fiber tip. (a) Experimental setup. Optical resonances are coupled to a spheroid melted fiber tip by an eroded single mode fiber through evanescent wave coupling. (b) Micrograph of the glass spheroid microcavity and the eroded single mode fiber for resonance coupling. (c) Optical resonances are detected as transmission dips in the photodiode signal as the laser wavelength is tuned. (Adopted from Vollmer et al., Appl. Phys. Lett. (2002))

The optical resonances were detected as dips in the light intensity transmitted through the eroded fiber as the laser wavelength is tuned. Biosensing application was demonstrated through the detection of nonspecific adsorption of

Reproduced with permission of the copyright owner. Further reproduction prohibited without permission.

Bovine Serum Albumin (BSA) as well as the immunoassay reaction between BSA-biotin and streptavidin. Adsorption of proteins (here BSA) on to the microcavity changes the size and the refractive index of the microcavity which can be detected as a shift (to a longer wavelength) in the resonant spectrum. Similarly, the immunoassay reaction between BSA-biotin (which is adsorbed on the surface of the microcavity) and Streptavidin (which is introduced into the liquid medium surrounding the microcavity) can also be detected by observing the shift of a specific resonant peak upon binding. This technique offers low detection limits; a single layer of BSA molecules adsorbed on the microcavity surface can be detected. Multiplexed DNA detection and quantification was also demonstrated using two resonant microcavities.[69]

Recently, various applications of microsphere-based sensors have been demonstrated by the Xudong Fan Lab in University of Missouri, Columbia.[70-74] Their experimental setup is very similar to Vollmer et al. The optical resonances of a spheroid microcavity are excited by a fiber prism and the reflected light is collected through a detector. A spectral dip in the reflected light corresponds to a resonant mode of the microcavity. The resonant wavelength shifts upon removal/binding of molecules from/onto the microcavity surface.

Initially, detection of the removal of silica molecules from the microcavity surface[73] was investigated as the microcavity was immersed in and etched by a low concentration hydrofluoric acid solution. (Figure 3.2) Although introducing the HF solution into the medium changes the refractive index and the temperature of the system; a steady shift which depends on the acid concentration and not saturating over long period of time was clearly indicating that removal of silica molecules due to etching was the main cause behind the observed spectral shift.[75] In a

Reproduced with permission of the copyright owner. Further reproduction prohibited without permission.

similar way, the Xudong Fan group has also demonstrated protease (trypsin) detection. Removal of a monolayer of protein (BSA) by a protease (trypsin) was observed on the surface of a microsphere.[72] More recently, the same group has developed a new technique based on liquid core optical ring resonators. The optical resonances are excited through anti-resonant reflecting optical waveguides and the analytes to be detected are carried to the sensor surface through the liquid core of the ring resonator.[76, 77] This way, the liquid core both serves as a low refractive index medium to support optical resonances within the ring resonator as well as serving as the medium carrying the analytes to be detected.

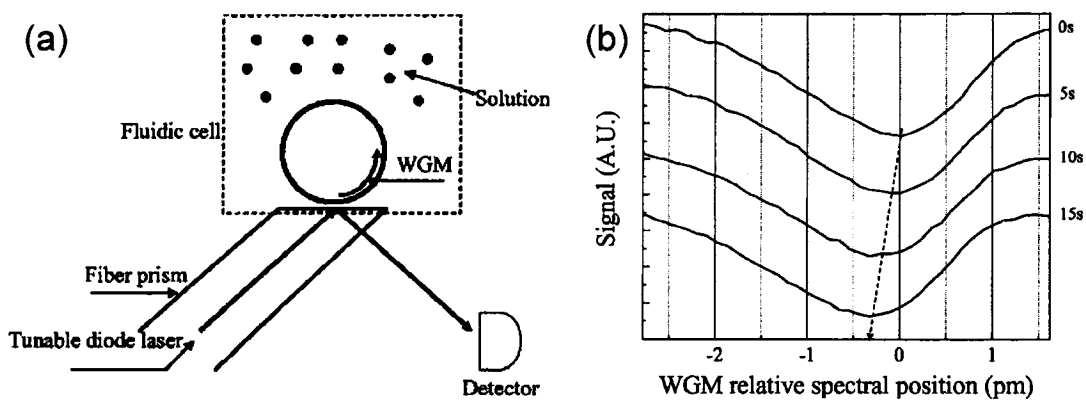

Figure 3.2 Subfemtomole detection of small molecules by a microsphere-based sensor. (a) Experimental setup. Optical resonances are coupled to a spheroid silica microcavity by a fiber prism. (b) As the microcavity is etched with HF, the resonant wavelength is blue-shifted. A spectral shift as low as 0.04 picometer (corresponding to removal of 0.4 femtomole silica molecules) can be detected. (Adopted from White et al., Opt. Lett. (2005))

In addition to microspheres, various microcavity geometries – including microring, microdisk – have been utilized in a biosensor format. Using microdisk and microring shaped resonators as biosensors are first proposed by the theoretical work of Boyd et al and Blair et al in 2001.[78, 79] Since then, many experimental studies have been reported on the demonstration of biosensing applications of microring and microdisk resonators.[33, 76, 77, 80-88]

Reproduced with permission of the copyright owner. Further reproduction prohibited without permission.

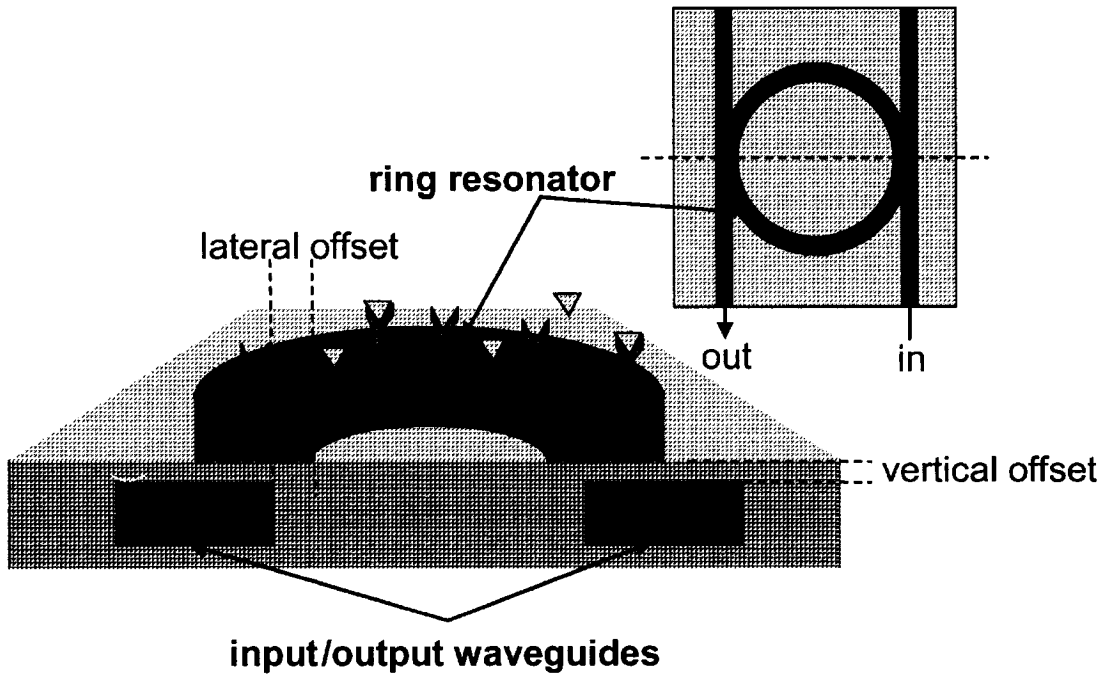

Figure 3.3 A ring resonator biosensor. A ring-shaped optical resonance-based biosensor with Q≈12,000. The resonance peak shift is linearly dependent on the refractive index of the medium. Smallest detectable refractive index change is 1.8 x 10^{-5} refractive index units. Avidin-biotin binding is demonstrated for biosensing applications. (Adopted from Yalcin et al., IEEE J. Sel. Top. Quantum. Electron. (2006))

The work by Yalcin et al. is a useful example of a microring biosensor exploiting the ultra-high sensitivity of optical resonance-based biosensing.[33] A ring resonator is coupled to two planar waveguides; one of them delivers the tunable laser which excites the resonant modes of the ring-shaped microcavity and the other one collects the output signal from the microcavity (Figure 3.3). As the analytes bind to the surface of the resonator, the resonant wavelength is shifted to a longer wavelength. Instead of measuring the shift of the resonant wavelength, Yalcin et al initially characterized the resonant spectrum of the microring cavity, then observed the intensity drop at one of the resonant wavelengths as the resonant peak shifts upon binding. Therefore, the shift in the resonant peak is deduced from the intensity drop and related to refractive index change of the sur-

Reproduced with permission of the copyright owner. Further reproduction prohibited without permission.

rounding medium. Small changes in the refractive index (1.8×10^{-5} refractive index unit) of the surrounding medium can be detected. They have also demonstrated the detection of avidin-biotin binding on the microring resonator surface.

Regarding the theoretical studies on optical resonance-based biosensors, we point out to the following reports and the references therein.[78, 79, 89-98] There is also a recent review on optical resonators with Whispering Gallery Modes which successfully summarizes all the theory and applications of optical resonances in microcavities.[99, 100]

This concludes the theoretical and experimental review of the utilization of optical resonances for chemical and biological sensing applications. In the following chapters (Chapters 4 through 7), the experimental work for this dissertation research will be described.

A short digression on the detection limit of optical resonators

The resonant frequencies depend on the size of the resonator. In general, the resonant modes for a circular resonator are approximately predicted by $2\pi rn = mc_0/f$, where m is an integer, n is the refractive index of the cavity material, r is the radius of the cavity, and f is the resonant frequency of mode m. The frequency shift of a given resonant mode is estimated to be $\Delta f/f = -(\Delta r/r + \Delta n/n)$, where Δr and Δn represent small changes of the radius and refractive index of the cavity, respectively.

If we assume a constant refractive index and consider the linewidth of the resonance to be the smallest measurable shift (taken as Δf = 10 MHz, $f = 3.75 \times 10^8$ MHz at λ = 800 nm), then the smallest "measurable" size change is $|\Delta r|_{min} = 2.6 \times 10^{-8} r$. With a radius r in the range of 1–10 μm in a typical microcavity, $|\Delta r|_{min}$

Reproduced with permission of the copyright owner. Further reproduction prohibited without permission.

is down to the order of 10^{-4} nm, which is an order of magnitude smaller than the size of an atom that is potentially detectable in theory.

Such a feature is being explored for use as detectors and sensors for identifying molecules surrounding the peripheral surface of optical resonators. When peptides, protein molecules, or cell membranes are attached on a resonator, they interact with the evanescent radiation field around the resonator. The interactions polarize the molecules or target analytes and change the effective size and/or refractive index of the resonator. All these can lead to a detectable frequency shift in the resonance modes. Thus it is possible to identify and detect single molecules by observing the resonant frequency shifts in optical resonance-based sensors. These optical resonance techniques can also be used to enhance the existing sensitivity of biosensor devices.

Reproduced with permission of the copyright owner. Further reproduction prohibited without permission.

Chapter 4

Detecting Single Bacterial Cells through Optical Resonances in Microdroplets

A. Introduction

As discussed in Chapter 3, optical resonances in microcavities have recently been utilized in biosensing applications.[34, 68, 69, 72, 73, 101] These studies have shown that the resonances, often called Whispering Gallery Modes (WGMs) or Morphology Dependent Resonances (MDRs), can be used for detecting the specific binding between two biomolecules. Vollmer[34] et al. demonstrated protein detection by observing the shift of a resonant peak in a silica microsphere through the adsorption of proteins on to the microsphere, inducing a change in its size and/or optical properties and thereby offering a sensitive detection scheme.

Reproduced with permission of the copyright owner. Further reproduction prohibited without permission.

The effect of inclusions in a microcavity is of great interest from both the theoretical and experimental perspective. The size and number of inclusions will have a direct impact on the MDRs inside the cavity through scattering and local refractive index changes. The radial position of the inclusion and its orientation with respect to the illumination source is also important. Experimental work has shown a variety of effects of inclusions in liquid microcavities.[102-108]

In this chapter, I describe the detection of single bacterial cell inclusions through the suppression of optical resonances in liquid microcavities. The results of this study have been submitted to Optics Letters for publication.

B. Methods and Materials

Here, I will provide the details of the setup used for the experiments described in the next three chapters (Chapters 5 through 7). In the latter chapters, I will give a brief description of the setup and provide the modifications necessary for specific experiments.

The experimental setup consists of a droplet generator, a laser, a spectrometer and a CCD camera (Figure 4.1). The droplet generator is a customized commercial piezo inkjet printhead (Epson, Japan). Only one of the nozzles is used to eject droplets with approximately 20 micron diameter. This single nozzle is driven by a function generator (Agilent 33120A, Palo Alto, CA) through a specially developed circuit. A square voltage of 6.3 Volts (peak-to-peak) is sufficient to eject droplets. Increasing the magnitude of voltage applied to the piezo only changes the initial speed of the droplets and does not affect the size of the droplets. The droplets are diagnosed about 2 mm away from the orifice. The droplets reach the laser focus in a time scale of few tens of milliseconds (0-50 ms after

Reproduced with permission of the copyright owner. Further reproduction prohibited without permission.

ejection is used for most experiments) with an initial ejection speed on the order of few meters per second.

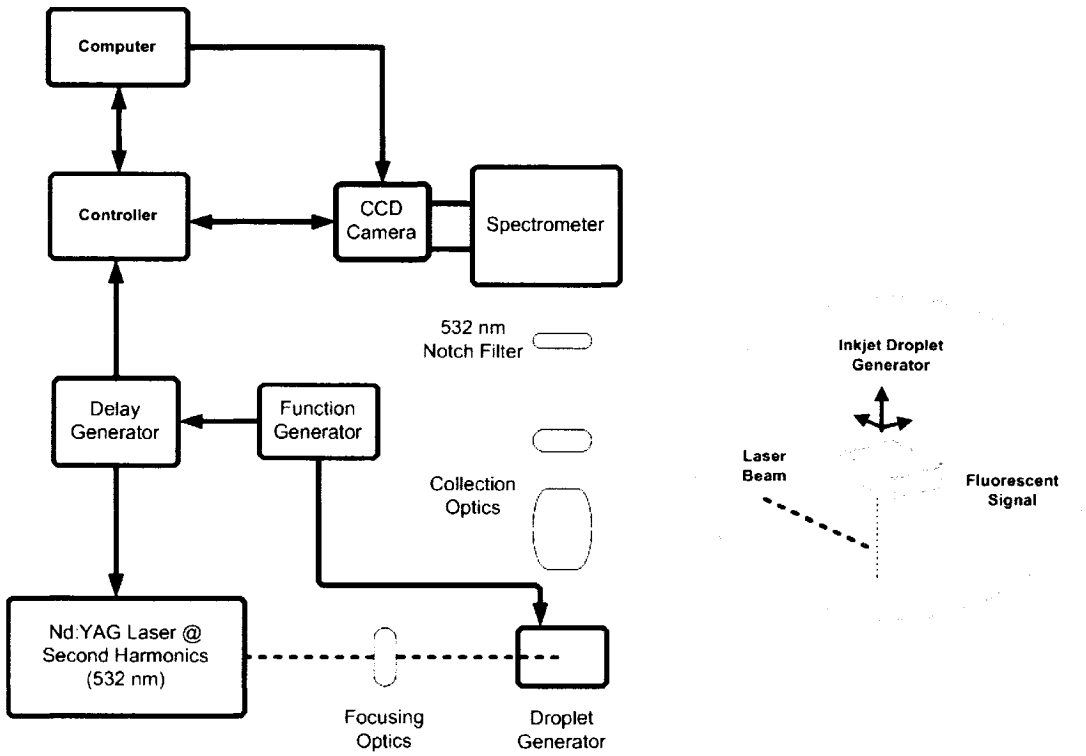

Figure 4.1 Experimental setup for optical resonance experiments in microdroplets. The microdroplets are produced by a modified commercial inkjet printhead and excited at 532 nm. The fluorescent emission is collected at 90° with respect to the excitation beam and focused onto a spectrometer/CCD camera system.

The microdroplets are optically pumped by the second harmonic (532 nm) of a Q-switched Nd:YAG laser (Spectra Physics, Mountain View, CA). The original beam size is 8 mm. The beam (intensity, 0.24 MW/cm^2) is focused to a 50 micron spot. The fluorescent signal from the microdroplets is collected by a long working distance Plano Apochromat lens (Mitutoyo, Japan) and an objective lens.

The collected emission light is focused onto a 150 mm focal-length, dual-grating, imaging spectrometer (Acton Research Corporation, Acton, MA). This spectrometer is connected to a TEK 512 x 512D front-illuminated thermoelectrically-cooled CCD camera (Princeton Instruments, Trenton, NJ). The

Reproduced with permission of the copyright owner. Further reproduction prohibited without permission.

data collection is executed from this configuration through a controller (ST-130, Princeton Instruments) which is an interface between the camera and the computer. The data is collected and processed through the Princeton Instruments software controlling the camera shutter and the controller.

The scattered laser light collected by the collection lenses is filtered out by a holographic notch filter (Kaiser Optical Systems, Ann Arbor, MI) at 532 nm.

The camera, the laser and the droplet generator are synchronized by a function generator and a delay generator (DG535 SRS, Sunnyvale, CA). The timing scheme is as follows: First, the function generator sends a square signal to the droplet generator to start the droplet ejection. This signal is also sent to the delay generator as an external trigger to synchronize the function generator and the delay generator at the time of the droplet ejection. The triggering delay from an external source is 85 ns and the jitter of the delay generator for the delayed signals is 0.86 ns. So this will determine the timing accuracy of the delayed signals. The first delayed signal is sent to the laser as a trigger to the flash lamp. The laser light is released from the cavity around 270 μs after the flash lamp trigger. By adding a delay of 1 ms delay between the function generator (droplet trigger) and the flash lamp trigger (laser trigger), the real time delay is approximately 1.27 ms. The second delayed signal is sent to the camera. This happens around 80 ms. after the droplet is ejected and the laser is triggered. The shutter opens in 5-10 ms and shuts down in 20-25 ms. In this configuration the camera will catch the next droplet and laser excitation pulse. The timing logic is simple: the camera shutter and the image processing time is the slowest step in this detection scheme, so it is more convenient to setup the camera system to catch the next excitation.

Reproduced with permission of the copyright owner. Further reproduction prohibited without permission.

With the help of synchronization, it is possible to probe every microdroplet ejected by the droplet generator. The throughput is limited by the speed of the camera and controller data processing time. The maximum effective rate is limited to 10 Hz with the system resulting in data acquisition every 100 ms. By changing the delay time, the microdroplet can be diagnosed between 0-50 ms after its ejection. The time resolution of droplet diagnostics in this time interval is limited by the uncertainty which depends on the relative size of the droplet and the laser spot. The time interval of 50-100 ms is not reliable because the droplets slow down (get closer to their terminal speed) and are easily affected by the air disturbances; misalignment of the droplet trajectory and the laser beam can ensue. This causes poor repeatability of the experimental results.

The cell cultures were prepared at UC, Davis. The E-Coli KB culture was prepared in Luria-Bertani Medium (LB Medium, Contents/liter: 10g tryptone-B, 5g yeast extract-B, 10g NaCl, adjust pH=7.0) at 37 C overnight. The 50 ml culture was centrifuged and washed with PBS solution (Contents/liter: 8.18g NaCl, 2.98g KCl, 0.27g Na_2HPO_4-$7H_2O$, 1.43g KH_2PO_4, adjust pH=7.4) twice before running the experiment and reduced down to a 4 ml volume. This washing cycle is necessary for two reasons: 1) to demonstrate the detection in PBS/R6G solution 2) to avoid the optical effects of the LB medium on the fluorescence resonance spectrum from the microdroplets. The concentrated cell culture was then diluted 10-fold by 10 μM Rhodamine 6G (R6G) in phosphate buffer solution (PBS). The experiments were performed within 4 hours of the PBS wash; assuring most of the cells are still alive during the experimental run. The Streptococcus culture was prepared in Tryptic Soy Broth (TSB media, Contents/liter: Peptone from casein 17g, Peptone from soymeal 3g, dextrose 2.5g, NaCl 5g, K_2HPO_4 2.5g, adjust

Reproduced with permission of the copyright owner. Further reproduction prohibited without permission.

pH=7.3) for 72 hours. The 500 ml culture was centrifuged and washed with PBS twice to a final volume of 10 ml. For the experimental run, the thick cell culture was diluted 20-fold with 10 μM R6G in PBS.

For the droplet generation, several milliliters of each cell solution in R6G/PBS were enough. The actual amount of sample used in each experiment was in the nanoliter range, but several milliliters were flushed through the printhead to make sure that the droplets produced by the instrument contained the solution to be diagnosed. After each run the printhead was flushed with 20 ml Deionized water (DI water) (Resistance = 18 MΩ) and operated for 5 minutes to avoid contamination between each run.

Incubated and washed cell cultures (E-Coli KB and Streptococcus) were diluted in Phosphate Buffer Saline (PBS) buffer containing 10 μM Rhodamine 6G. The cells were checked under a microscope for viability to assure that most of the cells were alive during the experimental run. The cell-Rhodamine 6G solution was used immediately after its preparation to avoid any absorption/adsorption of fluorescent molecules by the cells which would reduce the concentration of free Rhodamine 6G in the solution. The cell concentration was checked in a 96-well plate reader with absorptivity measurements at 600 nm. Assigning an optical density of 1 at 600 nm (Maniatis[109] et al.) to a concentration of 10^8 cells/mL, we concluded that the cell cultures prepared had on the order of 10^9 cells/mL. The volume of a 20 micron-diameter droplet is approximately 4.19 picoliters (pL). Therefore, with a cell concentration of 10^9 cells/mL and an average droplet diameter of 20 microns, every microdroplet contained 0.3 cells on average. This means that three in every ten microdroplets should yield an observation of a single cell.

Reproduced with permission of the copyright owner. Further reproduction prohibited without permission.

C. Results and Discussion

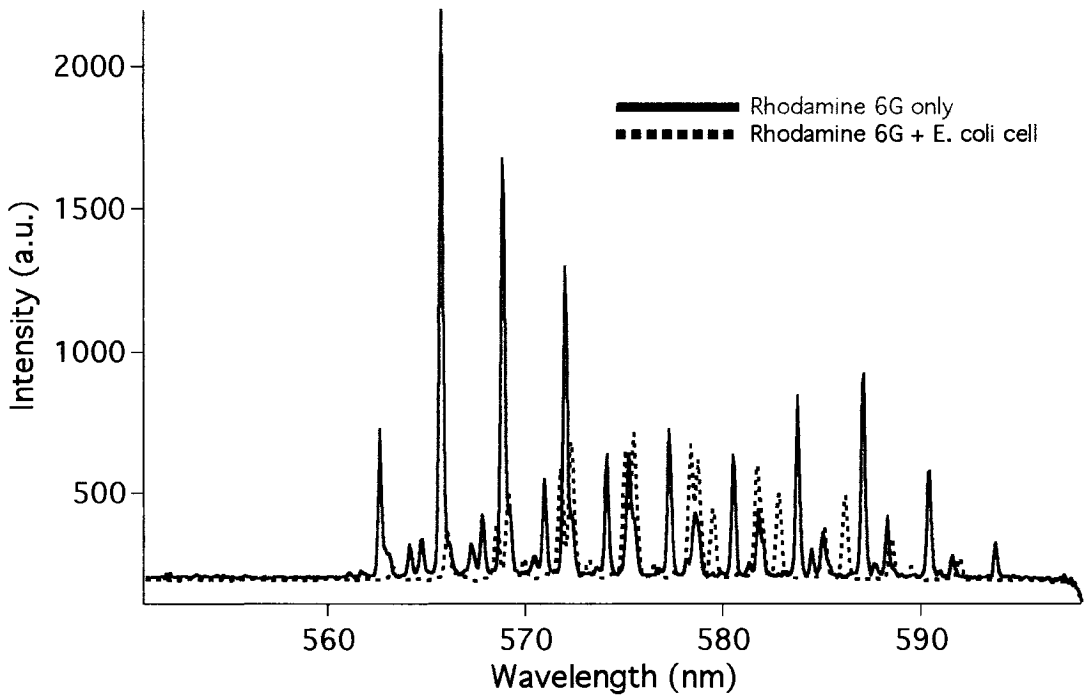

Figure 4.2 Suppression of MDR peaks in a microdroplet due to a single cell presence. The suppression of MDR peaks when the E-Coli cells are added to the fluorescent solution. Here the sample solution consists of 10 μM Rhodamine 6G in PBS with E Coli cells (~10^9 cells/mL). The sample size in a 20 micron droplet is about 4.2 pL.

The MDR spectrum of 10 μM Rhodamine 6G in PBS solution (without cells) exhibits intense maxima at the first order modes of the microdroplet cavity (Figure 4.2). When cells are added to the solution, the suppression of the MDR peak intensities are observed in the microdroplet spectrum. The effect of cell inclusions in the microdroplet is similar to quenching or a reduction in the Q factor of the cavity. This quenching effect can be due to two effects: the local refractive index can change due to the presence of a cell inside the microcavity; the cells can also lead to scattering losses within the cavity. Although scattering can increase the mode visibility by increasing the photon leakage from the microcavity, it can also induce a reduction in Q factor due to an asymmetry in refractive index

Reproduced with permission of the copyright owner. Further reproduction prohibited without permission.

profile of the optical cavity resulting in a reduction in MDR peak intensities. From the spectrum, one can observe that most of the first order modes are suppressed. Meanwhile, some of the higher order modes at the blue end of the spectrum have higher intensities compared to the original spectrum. This is mainly because of the leakage of the high order modes due to scattering. Usually, the modes with higher radial mode-order number (ℓ) have low intensities compared to the first order modes and tend to disappear first when the cavity medium has a quenching or absorbing component. These results, in general, confirm previous experimental and theoretical studies on the effect of inclusions in microdroplets.[102-105] In addition, there is no obvious spectral shift associated with the inclusion of cells into the optical cavity. The MDR peak locations remain unchanged.

Figure 4.3 shows ten consecutive spectra from the same cell detection experiment. From the estimate that three out of ten microdroplets should contain a single bacterial cell, we expect that approximately three out of ten spectra should indicate the presence of a cell, on average. Through the spectra, it can be seen that in two out of ten microdroplets, the MDR peak intensities have dropped dramatically. For low cell concentrations, the number of cells in a single microdroplet should follow Poisson statistics, and it is possible to have more than one cell in each microdroplet when the resonance suppression is observed. With an average concentration of 0.3 cells per droplet, the probability of detecting $n = 1,2,3$ cells would be 0.222, 0.033 and 0.003 respectively.

Single cell detection through MDR spectra was confirmed by the observation of diffraction patterns through the interaction between the microdroplet and

Reproduced with permission of the copyright owner. Further reproduction prohibited without permission.

the laser. The images of the diffraction patterns from the microdroplets containing a single streptococcus cell are shown in Figure 4.3.

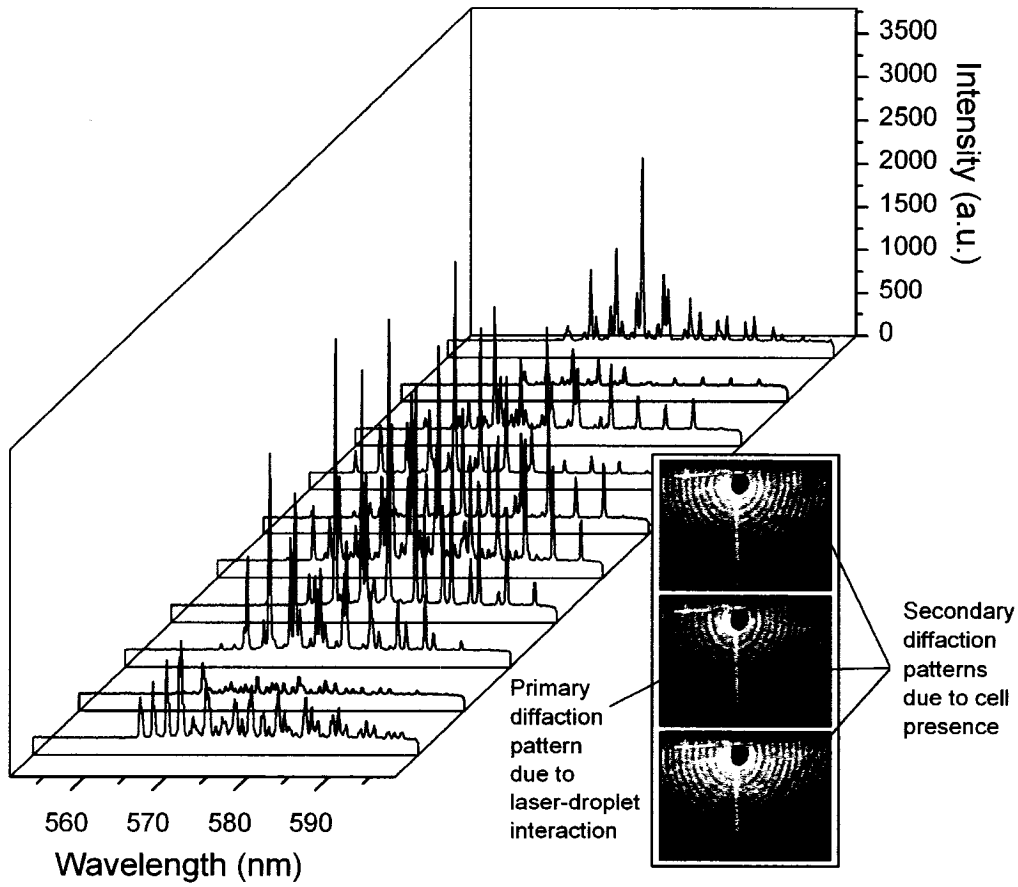

Figure 4.3 Single cell detection through optical resonances in microdroplets. Ten consecutive spectra from the cell detection experiments in microdroplets. Here, a single cell presence is detected in two droplets in a total of ten droplets observed through the suppression of MDR peaks (spectra numbers two and nine counting from front to back). A single cell event is confirmed through the observation of a secondary, dimmer, diffraction pattern (due to cell presence) that is superimposed on the primary diffraction pattern caused by the microdroplet alone.

Whenever a single cell event is detected through the spectrum, a secondary, dimmer, diffraction pattern is observed on top of the primary diffraction pattern. The primary diffraction pattern is due to laser scattering from the microdroplet. The secondary diffraction pattern is due to laser scattering from the round cell in the microdroplet. The secondary diffraction pattern appears at different loca-

Reproduced with permission of the copyright owner. Further reproduction prohibited without permission.

tions on the primary one, since it depends on the location of the cell which is random within the microdroplet. The diffraction pattern data can also be used to rule out the presence of multiple cells in a microdroplet, because multiple cells would exhibit multiple secondary diffraction patterns on the primary diffraction pattern.

We also examined the difference between the signal from the E. Coli culture and the Streptococcus culture to check the effect of inclusion morphology on MDR spectra. E. Coli is rod-shaped and Streptococcus is round-shaped. Both types of cells are approximately 1-2 microns in size. The comparison of the MDR spectra from both experiments does not suggest an obvious difference to distinguish between the shapes of the cells inside the microdroplet. However, there is an indication that cell morphology can play a role in altering the shot-to-shot differences in MDR spectra. The round-shaped cells lead to a constant reduction when the resonance suppression is observed – surprisingly, the rod-shaped cells show a variation in the spectra instead of a constant reduction in the intensity of MDRs. The variation of intensity reduction arises from the random orientation of the rod cells with respect to the location of the MDRs inside the spherical microcavity. Observations of this sort can be used as an indication of cell morphology.

The location of the cell inside the microdroplet plays an essential role in determining the changes observed in the MDR spectrum. The cell, as an inclusion, will affect the MDRs if it is located near the droplet rim where the resonances are intense. If the cell is located near the center of the droplet, it will not affect the MDR spectra; therefore it will count as a "miss" in the detection process. In addition, the scattering effect of the inclusion will increase, if it is located at one of the two focal points of the microdroplet (due to lensing effects).

Reproduced with permission of the copyright owner. Further reproduction prohibited without permission.

Furthermore, we checked the effect of cell viability on the MDR spectra. To do this, the cell cultures were exposed to UV light for ten minutes. The cell viability was checked under microscope. After UV exposure, the cell motility was reduced by more than 90%. When these cells were used for the experiment, the results showed no difference between the live cells and the dead ones. This is due to the fact that the cell membrane remains intact for a while after the exposure. In particular, E. Coli cells have a cell wall in addition to the membrane that would maintain the same cell shape after lysis.

The detection of single bacterial cells in microdroplets has been demonstrated using optical resonances. At cell concentrations as low as one per microdroplet; the MDR peaks have been suppressed. The mechanism is mainly due to the local refractive index change and scattering caused by the cells. Absorption/adsorption of fluorescent molecules might have contributed further to the signal reduction. The detection system is non-specific; any inclusion that would cause a change in the optical characteristics of the microcavity would change the nature of the MDR peaks. The advantage of the system is the omission of the labeling procedure for the bioparticulates to be detected. The fluorescent marker is simply added to the final solution without any specific binding protocols to label the cells to be detected. The effect of the cell morphology and viability on the MDR peaks was also studied. Cell morphology affected the variability of the spectra from droplet to droplet as rod-like cells rotated randomly inside the droplets. Cell viability did not affect the spectra. Further analysis of the data focused on the mode visibility and lasing thresholds might help distinguish different cell shapes and cell viability, especially when combined with additional light scattering information.

Reproduced with permission of the copyright owner. Further reproduction prohibited without permission.

Chapter 5

Fluorescent Immunoassays in Microdroplets through Radiative Energy Transfer Mediated by Optical Resonances

A. Introduction

One of the most common optical detection techniques used for bioassays is fluorescence detection. Some of the fluorescence detection techniques use an affinity-based energy transfer phenomenon called Fluorescence Resonance Energy Transfer (FRET). As explained in detail in Chapter 2, a non-radiative energy transfer occurs between a donor and an acceptor depending on the distance between them and the overlap of the emission spectrum of the donor and the ex-

Reproduced with permission of the copyright owner. Further reproduction prohibited without permission.

citation spectrum of the acceptor. The transfer efficiency depends inversely on the sixth power of the distance between the donor and the acceptor molecule leading to a powerful nanoscale (2-10 nm) measurement technique. The transfer efficiencies for a wide variety of fluorescent dyes have been studied.[110] Non-fluorescent quenchers such as QSY can also be used as efficient acceptors (donors) because of their availability in a wide spectrum range and the absence of any intrinsic fluorescence emission.

FRET can be used as an efficient detection tool for fluorescent immunoassays.[111-118] Antibody and antigen pairs can be labeled with FRET pairs, e.g., antibody with a fluorescent dye and antigen with its FRET pair; and used in different immunoassay formats including competitive immunoassays. Upon binding reaction between the antibody and the antigen, the FRET dye pairs will come to close proximity. This will increase the FRET efficiency of the dye pair. The binding reaction can be observed as a simultaneous decrease in the donor signal and a corresponding increase in the acceptor signal due to the energy transfer between the fluorescent dyes. If a non-fluorescent dye (quencher) is used as an acceptor, then we only observe the decrease in the donor signal and relate it to the reaction between the antibody-antigen.

Microdroplets have several advantages for performing FRET based immunoassays.[119, 120] The first advantage is the small sample volume that is presented in the micron-sized droplets used in the experiments. The second advantage is the elimination of non-specific binding to the sample container walls. The droplets are airborne and only interact with laser light. Another advantage arises from the optical cavity formed by the microdroplets. As discussed in Chapter 2, the energy transfer can be enhanced due to the morphology dependent reso-

Reproduced with permission of the copyright owner. Further reproduction prohibited without permission.

nances captured inside the microdroplet.[67, 121-123] The emission from donor molecules can be efficiently coupled to the resonant modes of the microcavity, enhancing the photonic mode strength at those wavelengths. The acceptor molecules can be excited through these coupled resonances without being in the close proximity of the donor molecule, which is a general requirement for FRET. Hence, a more efficient energy transfer mechanism can be established and used to detect a wide variety of binding reactions. In this chapter, we demonstrate the detection of the specific binding of avidin and biotin through radiative energy transfer between a FRET pair in a microdroplet. The content of this chapter was presented in SPIE Photonics West 2005 and also published in the conference proceedings.

B. Methods and Materials

The experimental setup is very similar to the one described in Chapter 4 with some improvements for increased signal stability/repeatability. The setup consists of a droplet generator, two lasers (instead of one), a spectrometer and a CCD camera (Figure 5.1). One laser (He-Ne) is used to detect individual droplets ejected from the printhead nozzle. The other laser (Argon ion) is used as the excitation laser.

The droplet generator is a customized commercial piezo inkjet printhead that ejects approximately 20-micron diameter droplets. The droplets are first detected by a He-Ne laser (Uniphase, Manteca, CA) and a photodiode (Thorlabs, Newton, NJ). The red laser beam (633 nm) is focused on the droplets at a closer vertical position to the printhead nozzle and at a different angle than the Argon ion laser and the forward-scattered light is collected through a series of lenses and filters and focused onto the photodiode. The current induced in the photodiode is

Reproduced with permission of the copyright owner. Further reproduction prohibited without permission.

monitored through a digital oscilloscope (LeCroy, WavePro 7000, Chestnut Ridge, NJ). The peak of the signal is set as a threshold for the droplet detection and used as a timer for triggering the delay generator.

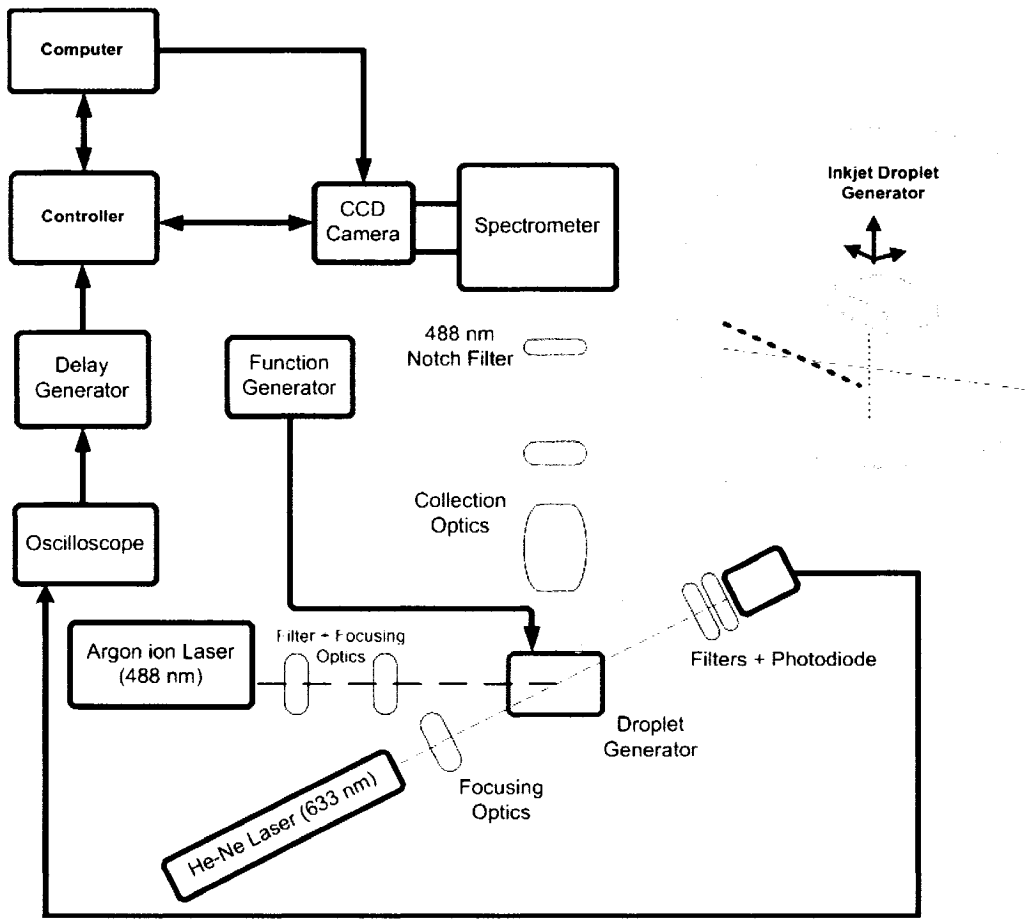

Figure 5.1 Experimental setup for fluorescent immunoassay experiments in micro-droplets. The droplets are first detected through a He-Ne laser/photodiode system. The droplets are then excited by an Argon ion laser. The fluorescent emission is collected and focused on to a spectrometer/CCD camera. The droplet detection system provides improved signal stability and repeatability for optical resonance experiments.

Two filters were used to avoid false signals due to the strong scattering from the Argon ion laser and red fluorescence emission from Alexa Fluor 555. One of them is a shortwave cutoff filter at 540 nm (Optosigma, Santa Ana, CA). This filter can block the scattered blue light from the laser. The second filter is a narrow-band interference filter (Optosigma, Santa Ana, CA), centered at 633 nm

Reproduced with permission of the copyright owner. Further reproduction prohibited without permission.

with a bandwidth of 1 nm. This filter blocks possible emission from Fluorescein or Alexa Fluor 555 dye in the droplet, which would interfere with the scattering light from the droplets through He-Ne laser. Since we observed the spectra in the 500-620 nm range, scattering from the droplets due to elastic scattering of He-Ne light did not affect our results.

Through this configuration, the fluctuations in the vertical position of the droplets were eliminated. By observing the scattering signal from the droplets, it is possible to determine the phases of the droplet ejection including satellite droplet formation. This allowed us to probe the droplets where they are stable and spherical and set their position precisely relative to the laser beam, resulting in a dramatic improvement in repeatability.

After the detection, the droplets generated by the inkjet printhead were optically pumped by an Argon ion laser (Coherent, Innova 70, Santa Clara, CA). The original beam (1.5 mm diameter at the $1/e^2$ point) was directed through a 488 nm bandpass filter (FWHM 1 nm, Optosigma, Santa Ana, CA) and was focused to a 50-micron spot to get better coupling of the pump beam into the microdroplets.

The resultant fluorescent signal from the droplets was collected by a long working distance lens, and then focused onto a dual grating imaging spectrometer which was connected to a cooled CCD camera as described in Chapter 4. The scattered laser light (Argon ion) was filtered by a holographic notch filter at 488 nm. The droplet detection signal from the He-Ne/photodiode is used to synchronize the camera and the droplet generator through the output of the digital oscilloscope and the delay generator.

Reproduced with permission of the copyright owner. Further reproduction prohibited without permission.

Fluorescein-labeled biotin (biotin-4-fluorescein); streptavidin-Alexa Fluor 555 conjugate (3 moles dye/mole protein); streptavidin-Alexa Fluor 610 conjugate (5 moles dye/mol protein); biotin labeled FluoSpheres (40 nm, yellow/green fluorescent); neutravidin labeled FluoSpheres (40 nm, yellow/green fluorescent) and Alexa Fluor 555 dye were purchased from Molecular Probes (Eugene, OR). To prepare biotinylated BSA-Rhodamine conjugate, ImmunoPure biotinylated BSA (8 moles biotin/mol BSA) was purchased from Pierce (Rockford, IL). 5-carboxyrhodamine 6G, succinimidyl ester was obtained from Sigma (St. Louis, MO). BSA-biotin and BSA were labeled with Rhodamine 6G following a standard procedure recommended by Molecular Probes. The degrees of labeling obtained were 1.3 moles Rhodamine/mol BSA-biotin and 1.4 moles/Rhodamine/mol BSA. FluoSpheres are polystyrene beads, which are internally loaded with a variety of dyes. Yellow-green fluorescent beads have excitation/emission maxima of 505/515 nm and thus are excited very efficiently using the 488 nm spectral line of the argon-ion laser. Biotin conjugated beads were used to observe the binding reaction between biotin and streptavidin. Neutravidin conjugated beads were used to conduct a control experiment for avidin-biotin reaction. Small bead size (40 nm) was chosen for two reasons. First reason is to eliminate the background signal in the Alexa Fluor 555 emission range due a possible bulk fluorescence emission from the beads. The second reason is to reduce the avidin binding ratio per bead and make it closer to the 4:1 ratio as observed in avidin-biotin binding in bulk solution. All solutions were prepared with PBS buffer (8.18 g/L NaCl, 2.98 g/L KCl, 0.27 g/L $Na_2HPO_4.7H_2O$, 1.43 g/L KH_2PO_4, pH=7.5). After each run the printhead was flushed with 20 ml deionized water (DI water) (Resistance = 18 MΩ) and operated for 5 minutes to avoid contamination between each run. A Spectramax M2

Reproduced with permission of the copyright owner. Further reproduction prohibited without permission.

microplate reader (Molecular Devices, Sunnyvale, CA) and black 96-well plates from Nunc (Rochester, NY) were used for initial FRET studies.

C. Results and Discussion

We chose the avidin-biotin pair as immunoassay agents to demonstrate the utilization of optical resonances for biosensing. Avidin-biotin pair has high binding affinity and this combination can be used efficiently for fluorescent immunoassay applications when one or both of them are labeled with fluorescent dyes. Avidin and biotin can be conjugated with different dye pairs using straightforward protocols and because of the relatively small size (biotin is a small molecule and avidin has dimensions of approximately 5.6 nm x 5.0 nm x 4.0 nm); the distances are suitable to observe energy transfer between the dye pairs. One avidin has four biotin-binding sites.

Initially, we studied the binding reaction between streptavidin and biotinylated BSA in a 96-well microtiter plate. Due to the considerable overlap of the emission spectrum of Rhodamine (absorption/emission maxima 525/547 nm) and absorption spectrum of Alexa Fluor 610 (absorption/emission maxima 612/628 nm) in the 550-600 nm range, these dyes can be used as a FRET pair to study the binding reaction between streptavidin and biotin. The degrees of labeling for the conjugates used in this experiment were 5.1 Alexa Fluor 610 molecules per one streptavidin molecule and 1.3 Rhodamine molecules per one biotinylated BSA molecule (8 moles biotin/mol BSA). Solutions prepared in PBS solution were mixed in the 5-20 μg/ml range for both reagents and incubated for at least 30 minutes before data acquisition in a fluorescence plate reader. Measurements for solutions containing only BSA-biotin-Rhodamine and only streptavidin-Alexa Fluor

Reproduced with permission of the copyright owner. Further reproduction prohibited without permission.

610 were performed for blank subtraction. The fluorescence intensity was measured between 550 nm and 700 nm (excitation: 525 nm) and the changes in the emission spectrum of Rhodamine and Alexa Fluor 610 were observed. After the blank subtraction, this binding reaction did not show any FRET. At constant Alexa Fluor 610 concentration, Rhodamine concentration was increased from 5 µg/ml to 20 µg/ml and no substantial change (less than 10%) in Alexa Fluor 610 emission was observed. To verify these data, the experiment was repeated with a non-specific pair, replacing BSA-biotin-Rhodamine with BSA-Rhodamine (1.4 moles Rhodamine/mol BSA). Streptavidin-Alexa Fluor 610 and BSA-Rhodamine pair showed a similar spectrum with the biotinylated pair. This shows that avidin-biotin reaction did not result in FRET between the dyes. This could be due to the relatively long distance between donor and acceptor molecules due to the low donor concentration (1.3 Rhodamine molecule per BSA-biotin).

To reduce the distance between the donor and the acceptor molecule, biotin-4-fluorescein (absorption/emission maxima 495/519 nm) and streptavidin conjugated with Alexa Fluor 555 (Absorption/Emission maxima 553/568 nm) pair was chosen thus excluding BSA from the reaction. The streptavidin-Alexa Fluor 555 concentration was kept in the 0-100 µg/ml range corresponding to 0-1.76 µM. The biotin-fluorescein concentration was varied between 1.4 and 11.2 µM to keep some excess fluorescein to account for the 4:1 binding ratio. In this configuration, the donor molecule was fluorescein and the acceptor molecule was Alexa Fluor 555. Similar to the Rhodamine/Alexa Fluor 610 pair, the Fluorescein/Alexa Fluor 555 pair also has substantial overlap for their emission/absorption spectra. The labeling ratio was 3 Alexa Fluor 555 molecules per one streptavidin molecule and 1 fluorescein molecule for each biotin molecule.

Reproduced with permission of the copyright owner. Further reproduction prohibited without permission.

The fluorescence emission intensity measurements were performed in a microplate reader between 510 nm and 620 nm (excitation at 485 nm) following incubation for at least 30 min. After the blank subtraction, the emission spectra for both dyes were compared. We observed a major decrease in fluorescein intensity while the streptavidin-Alexa Fluor 555 concentration was increased at a constant fluorescein-4-biotin concentration (Figure 5.2).

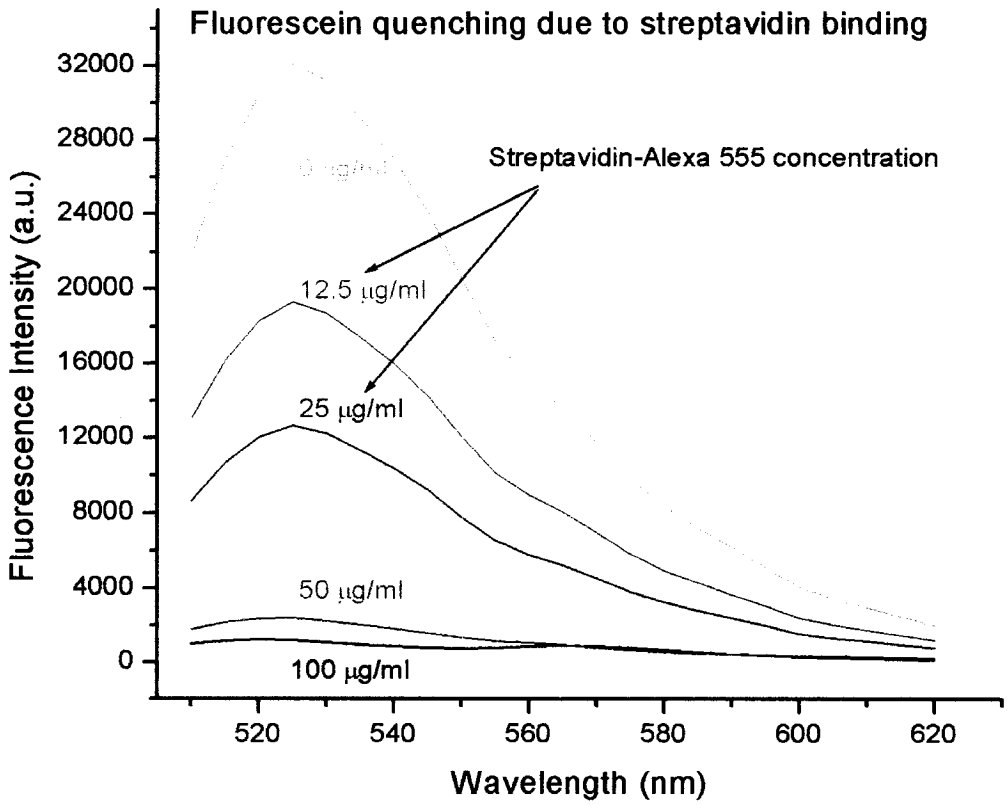

Figure 5.2 Fluorescein quenching (physical) upon streptavidin binding. Biotin-4-fluorescein (Absorption/Emission maxima 495/519 nm) and streptavidin-Alexa Fluor 555 (Absorption/Emission maxima 553/568 nm) interaction (Emission spectra at 485 nm excitation). The spectra correspond to 5.6 µM biotin-4-fluorescein at different streptavidin-Alexa Fluor 555 concentrations (0-100 µg/ml). Labeling ratio was 3 Alexa Fluor 555 (acceptor) molecules per one streptavidin molecule and 1 fluorescein (donor) molecule for each biotin molecule. A major decrease in fluorescein intensity due to contact quenching was observed when Alexa Fluor 555 concentration was increased at a constant fluorescein concentration.

When the streptavidin-Alexa Fluor concentration was above saturation, all the biotin-fluorescein molecules in the solution were bound to streptavidin and

Reproduced with permission of the copyright owner. Further reproduction prohibited without permission.

fluorescein emission intensity dropped down dramatically. But this decrease in fluorescein emission did not result in an increase in Alexa Fluor 555 emission. This means that instead of a resonant energy transfer to Alexa Fluor 555, the fluorescein emission was quenched by the binding reaction. Since the biotin-fluorescein complex is a small molecule (MW = 644), the binding reaction caused static quenching by streptavidin. This was confirmed by a control experiment where biotin-fluorescein was mixed with avidin only. The same fluorescence intensity drop was observed.

To avoid physical quenching due to binding, the link between biotin and the fluorescent tag should be sufficiently long. To achieve this, we used biotinylated fluorescent beads. As noted in the Methods and Materials section, we used 40 nm biotinylated fluorescent polystyrene beads (absorption/emission maxima 505/515 nm) with streptavidin-Alexa Fluor 555 to observe FRET. The streptavidin-Alexa Fluor 555 concentration was kept in the range from 25-200 µg/ml, while the fluorescent bead concentration was changed between 0.0045% and 0.019% corresponding to 1.31-5.25 x 10^{12} beads/ml. The fluorescent intensity measurements were performed at 500-620 nm (excitation at 485 nm) and emission peaks were observed with varying donor or acceptor concentration. The result was a decrease in fluorescent emission intensity from the nanobeads, corresponding to an increase in fluorescence intensity in Alexa Fluor 555 emission (Figure 5.3). This increase in acceptor intensity due to a decrease in donor emission implies an energy transfer between these molecules. Unlike the biotin-fluorescein and streptavidin-Alexa Fluor 555 reaction, the donor and acceptor molecules were close enough without being affected by the avidin-biotin interaction. We performed three control experiments to confirm this observation. Initially,

Reproduced with permission of the copyright owner. Further reproduction prohibited without permission.

to check whether observed intensity changes were due to specific binding, we replaced streptavidin-Alexa Fluor 555 with Alexa Fluor 555 only. As the Alexa Fluor 555 concentration was increased at constant fluorescent bead concentration, we neither observed a significant decrease in fluorescence emission from the beads nor an increase in Alexa Fluor 555 emission.

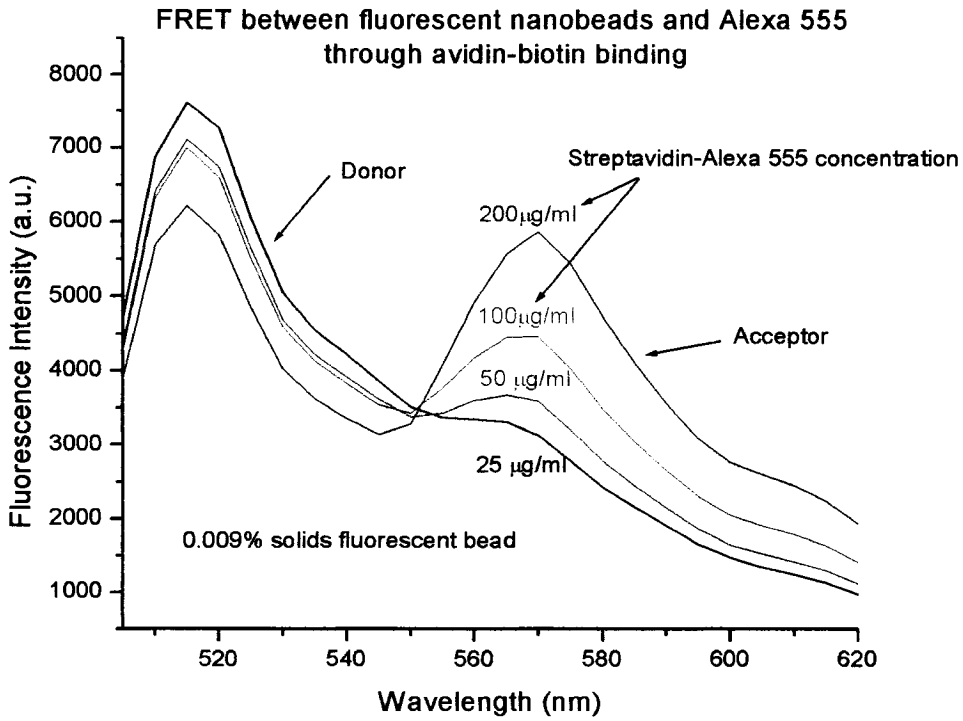

Figure 5.3. FRET observed between fluorescent nanobeads and Alexa 555 through streptavidin-biotin binding. 40 nm biotinylated fluorescent polystyrene beads (Absorption/Emission maxima 505/515 nm) and streptavidin-Alexa Fluor 555 interaction (Emission spectra at 485 nm excitation). The spectra presented correspond to 0.009% solids fluorescent beads and streptavidin-Alexa Fluor 555 at various concentrations (25-200 μg/ml). A decrease in fluorescent emission intensity from the nanobeads corresponding to an increase in fluorescence intensity in Alexa Fluor 555 emission is observed. This increase in acceptor intensity due to a decrease in donor emission implies an energy transfer between these molecules.

Additionally, we substituted biotinylated fluorescent nanobeads with beads, which were conjugated to neutravidin. In this case, we did not expect specific binding to occur between this pair. 0.1% BSA was added to the solution before incubation to reduce non-specific binding of streptavidin to the beads. As ex-

Reproduced with permission of the copyright owner. Further reproduction prohibited without permission.

pected, fluorescence emission intensities revealed that there was no correlation between donor and acceptor emission intensities when there is no specific binding. As a final verification, we checked the reaction between the biotinylated fluorescent beads and avidin only. In this scheme, we observed whether the binding reaction affects the donor emission in the absence of acceptor molecule. The fluorescence intensity dropped less than (10% compared to 50% in FRET) compared to the case where the acceptor molecule was conjugated to avidin. This observed intensity drop for the fluorescent bead emission shows that part of the donor emission drop observed in streptavidin-Alexa Fluor 555 and biotinylated fluorescent bead reaction is due to the binding reaction itself and cannot be completely attributed to FRET between the labels.

High photonic mode intensities in microdroplets increase the donor emission rate resulting in enhanced energy transfer efficiency for the FRET pairs which provides a high sensitivity biodetection scheme. Furthermore, the emission from the fluorescent beads (donor) can be coupled to the optical resonances of the microdroplet and enhance the acceptor emission through radiative energy transfer. To demonstrate these two effects, we repeated the biotinylated fluorescent bead and streptavidin-Alexa Fluor 555 binding reaction in microdroplets using the setup shown in Figure 5.1.

This can result in much longer Förster radii than expected for the FRET pair. The same energy transfer pattern was achieved with microdroplets with a further decrease in donor emission fluorescence and a larger increase in acceptor emission because of enhanced energy transfer efficiency (Figure 5.4 and 5.5). Streptavidin-Alexa Fluor 555 concentration was kept in the 25-200 μg/ml range,

Reproduced with permission of the copyright owner. Further reproduction prohibited without permission.

while the fluorescent bead concentration was changed between 0.0045% and 0.019%. We observed the morphology dependent resonances based on the fluorescence spectrum of fluorescent beads and Alexa Fluor 555.

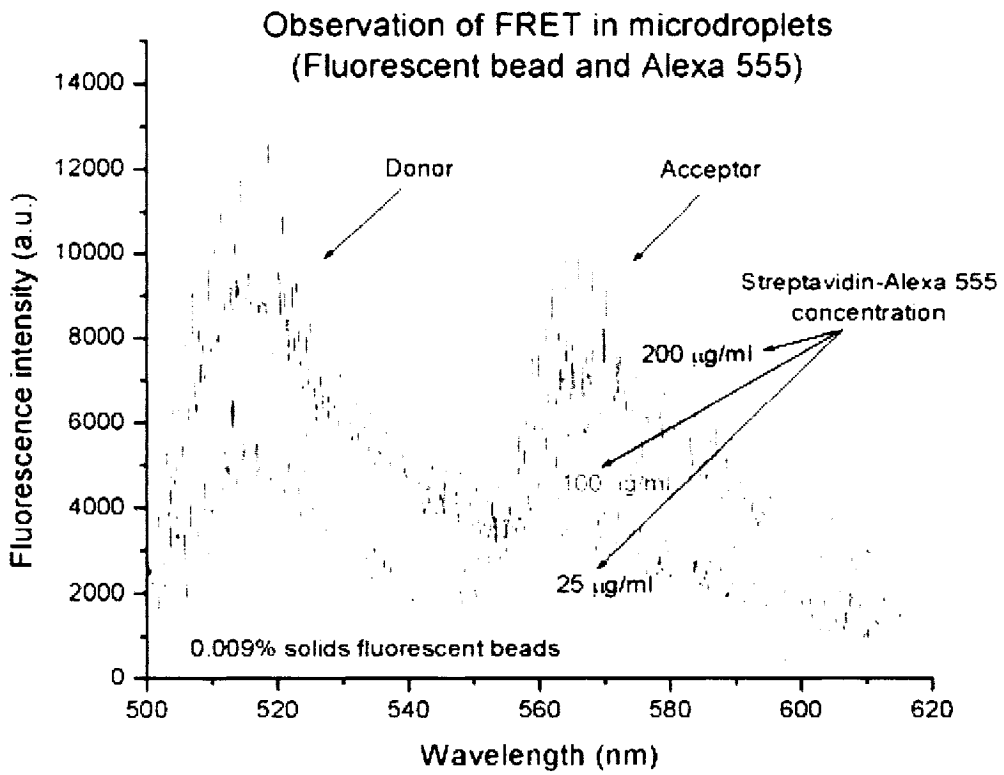

Figure 5.4. Detection of binding reaction between streptavidin and biotin through enhanced energy transfer in a microdroplet. Biotinylated fluorescent bead and streptavidin-Alexa Fluor 555 binding reaction in microdroplets. The spectrum presented corresponds to three different streptavidin-Alexa Fluor 555 concentrations (25,100,200 µg/ml) at constant fluorescent bead concentration (0.009 % solids). As the streptavidin-Alexa Fluor 555 concentration is increased, there is a decrease in the donor (fluorescent bead) emission (500-550 nm; laser excitation at 488 nm). Morphology dependent resonances based on the fluorescence spectrum of fluorescent beads and Alexa Fluor 555 are also observed. The emission from the fluorescent beads (donor) can be coupled to the optical resonances of the microdroplet and enhance the acceptor emission through radiative energy transfer. This results in enhanced energy transfer efficiency between donor and acceptor molecules.

From Figures 5.3 and 5.4, we observe that there is some bulk fluorescence emission, which is not associated with the fluorescence resonance energy transfer. This is due to the fluorescent donor molecules located in the inner region of the beads, which are sufficiently removed from their acceptor pair to support

Reproduced with permission of the copyright owner. Further reproduction prohibited without permission.

FRET. As a result, the donor emission decreases but was not completely quenched because of the energy transfer. Reducing the droplet size and the bead size can reduce the bulk emission from the beads.

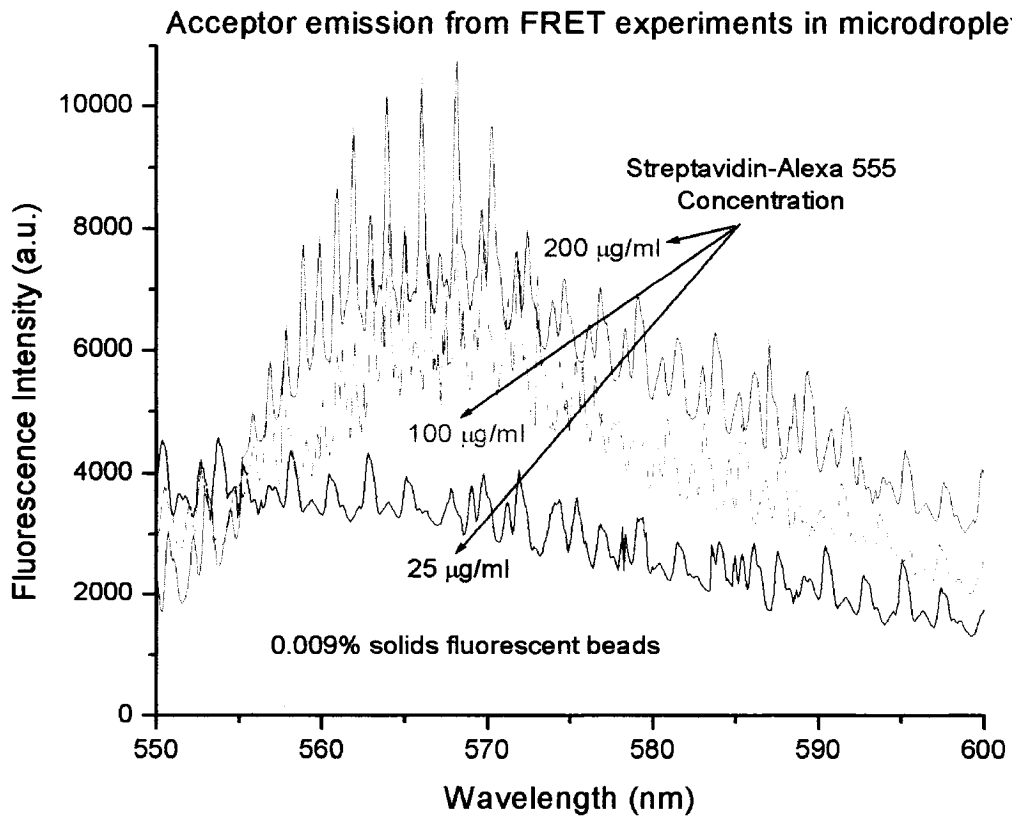

Figure 5.5. Acceptor emission from enhanced FRET (fluorescent radiative energy transfer) experiments in microdroplets. Acceptor (Streptavidin-Alexa Fluor 555) emission due to donor (biotinylated fluorescent bead) excitation through FRET as a result of the specific binding reaction in microdroplets. This figure shows the acceptor emission spectra in the 550-600 nm range and it is enlarged from Figure 5.4.

Some of the most important factors affecting FRET due to specific binding are the number of fluorescent molecules conjugated to avidin/biotin; the ratio of the concentrations of labeled avidin/biotin; the temperature and pH of the media as it affects the fluorescence spectrum; the emission/absorption overlap of the donor/acceptor pair; and the excitation wavelength. The detection mechanism used in this work can be applied to several immunoassay formats, including a

Reproduced with permission of the copyright owner. Further reproduction prohibited without permission.

competitive fluorescence immunoassay. The antibody can be conjugated to the donor dye of a FRET pair while the antigen can be coupled to the acceptor molecule. The initial emission from the acceptor molecule should be high because of the energy transfer between the donor and the acceptor. When an unknown amount of antigen is introduced into the solution, some of these antigens will replace the antigens labeled with the acceptor molecule and the change will be observed as a decrease in the acceptor emission.

Reproduced with permission of the copyright owner. Further reproduction prohibited without permission.

Chapter 6

Pendant Droplet Approach to Immunoassays in Microdroplets

A. Introduction

One disadvantage of using optical resonances in microdroplets is the spatial distribution of the resonances inside the droplet. Due to the nature of the total internal reflection, the resonances occur mostly around the droplet rim and do not penetrate into the inner regions of the droplet. As discussed in Chapter 2, the thickness of the region around the droplet rim where optical resonances occur is given by the following formula:

$$d = a\left(1 - \frac{m_0}{m_i}\right) \qquad \textbf{(6.1)}$$

where m_o and m_i are the refractive index of the outside and the inside of the microdroplet respectively. Assuming the refractive index of the microdroplet is

Reproduced with permission of the copyright owner. Further reproduction prohibited without permission.

1.33 (water) and the surrounding air is 1, the resonances occur around the droplet rim defined by a shell with a thickness of $0.25a$. This accounts for roughly 60% of the total volume of the droplet.

Since the optical resonances mostly occur around the droplet rim, it is ideal to have all the analytes in this region of the droplet to improve the detection sensitivity. This can be achieved through phase separation or hydrophobicity. In this chapter, an approach involving emulsions is proposed. Water-in-oil emulsions are prepared which assure that the necessary binding reaction for immunoassay occurs around the droplet rim due to the specific density difference between the oil and the water phase. The refractive index difference between the oil phase and the water phase is eliminated through index-matching by mixing glycerin into the water phase. The experiments reported here were presented as an invited paper at SPIE Optics East 2005 in Boston and published in the conference proceedings as well.

B. Methods and Materials

The experimental setup is again very similar to the previously described setups but this time the droplets are not produced by a piezo droplet generator (Figure 6.1). Instead of producing individual microdroplets into air, pendant microdroplets are produced at the tip of a pulled micropipette. The micropipette tip is approximately 5 μm. The analyte solution is ejected by a syringe pump through the micropipette tip. The micropipette tip is silanized before each run to prevent the droplet to move up and stick to the micropipette wall through capillary action. Silanization also helps producing droplets closer to perfectly spherical shape,

Reproduced with permission of the copyright owner. Further reproduction prohibited without permission.

which enhances the optical resonance effects. The pendant droplet size can be adjusted from 50 μm to several hundred microns.

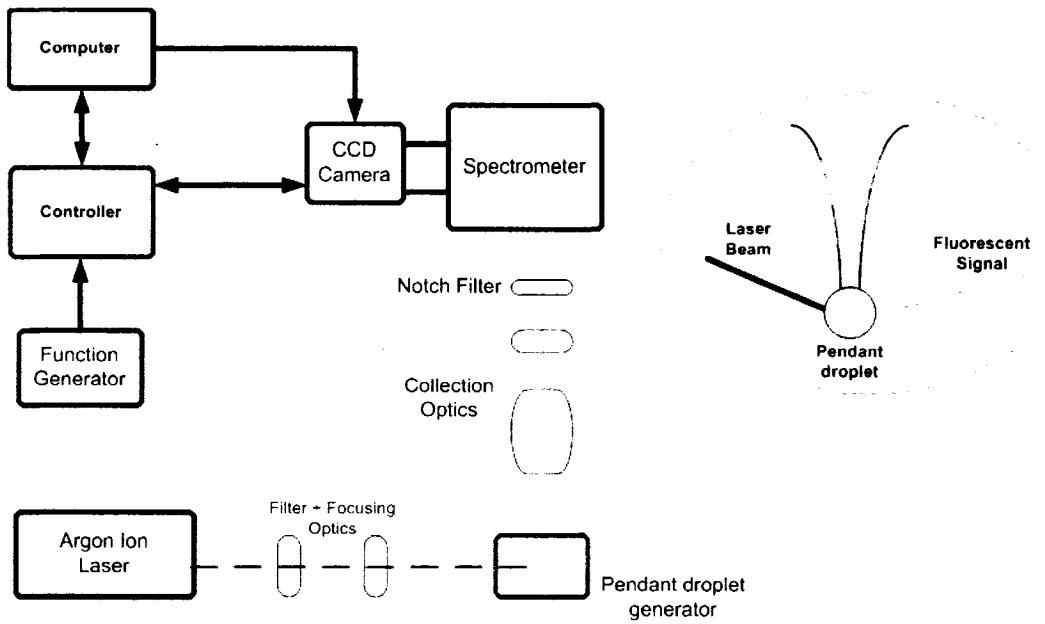

Figure 6.1 Experimental setup for pendant microdroplet experiments. The experimental setup consists of a micropipette pendant droplet generator, a laser, and a spectrometer/CCD camera detection system.

The pendant droplet is optically pumped by an Argon ion laser (Coherent, Innova 70, Santa Clara, CA). The original beam (1.5 mm diameter at the $1/e^2$ point) passing through a 488 nm bandpass filter (FWHM 1 nm, Optosigma, Santa Ana, CA) was focused to a 50-micron spot to couple the pump beam into the pendant droplet. The excitation geometry affects the resonance spectrum.[124] We tried different excitation geometries and observed that the most efficient coupling method is to focus the excitation source (Argon ion laser) at the bottom of the pendant droplet. In this configuration, the laser light enters the droplet tangentially and is trapped around the rim resulting in a strong fluorescent resonance emission.

Reproduced with permission of the copyright owner. Further reproduction prohibited without permission.

The details of all the reagents and buffers used in FRET experiments are given in Chapter 5. Here, we briefly summarize the crucial ones. Fluorescein-labeled biotin (biotin-4-fluorescein); streptavidin-Alexa Fluor 555 conjugate (3 moles dye/mole protein); streptavidin-Alexa Fluor 610 conjugate (3.1 moles dye/mol protein); biotin conjugated FluoSpheres (40 nm and 1 μm, yellow/green fluorescent) were purchased from Molecular Probes (Eugene, OR).

Two different bead sizes (40 nm and 1 μm) were used to take advantage of their properties in different stages of the experiments. Small beads (40 nm) were specifically used to observe the binding reaction between biotin and streptavidin through FRET. The large beads (1 μm) were also used to achieve streptavidin-biotin binding reaction; in addition, they were used to accumulate efficiently around the water phase (to form colloidal capsules) in the water-in-oil emulsion.

If the beads are large enough, they form colloidosomes around the water phase.[125] This allows maximum interaction between the avidin and biotin, which exist separately in water and oil phase respectively. All water phase solutions were prepared with PBS buffer (pH=7.5). Several oil phases (silicon oil, toluene, dodecane, decalin) were used to prepare the emulsion. Toluene and decalin were used to optimize emulsion preparation as mentioned in the pioneering work of Dinsmore et al. about colloidomes.[125] Since index-matching is essential for the experiments, lower refractive index liquids such as silicone oil and dodecane are used as the oil phase for the pendant droplet experiments. The refractive index of silicone oil is 1.397 and the refractive index of dodecane is 1.421. Matching the refractive index is achieved through 50% by weight water/glycerine solution for silicone oil and 65% by weight water/glycerine solution for dodecane.

Reproduced with permission of the copyright owner. Further reproduction prohibited without permission.

The emulsions used in the pendant droplet experiments are prepared as follows: biotin-4-fluorescein or biotin labeled FluoSpheres (absorption/emission peaks at 505/515 nm) were dissolved/suspended in the oil phase (silicone oil or dodecane). Streptavidin-Alexa Fluor conjugate (either Alexa Fluor 555 or 610) is dissolved in PBS then mixed with glycerine to match the index of refraction of the water phase with the oil phase[‡]. The water phase is added to the oil phase in several volumetric ratios (0.5%, 1%, 2%, and 5%) corresponding to different acceptor molecule concentrations and mixed gently with a pipettor with the oil phase. The result is a clear suspension (due to the refractive index matching) with micron-sized water/glycerine droplets in oil phase. The confocal microscope image of water droplets in the emulsion is shown in Figure 6.2.

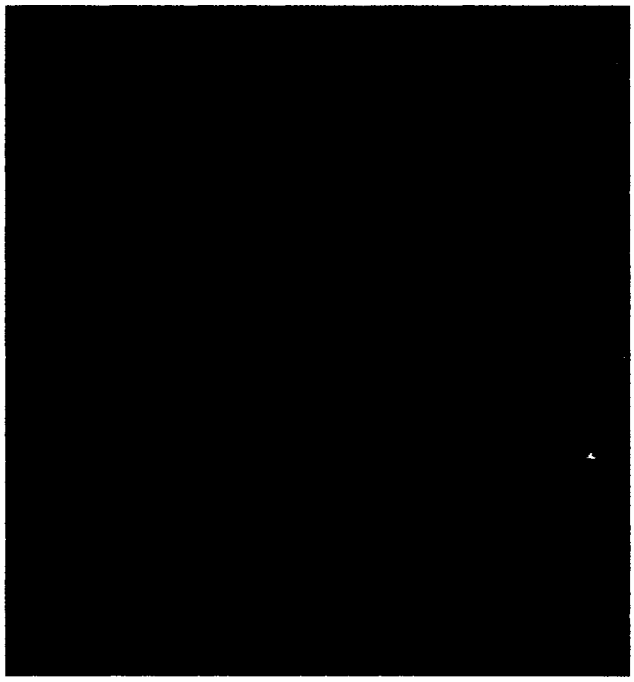

Figure 6.2 Confocal micrograph of the water droplets in oil phase. The red background is the toluene, which contains suspended 200 nm red fluorescent particles, and the green spots are the water droplets containing biotin-4-fluorescein.

[‡] 50% by weight glycerine/water solution for silicone oil and 65% by water glycerine/water solution for dodecane

Reproduced with permission of the copyright owner. Further reproduction prohibited without permission.

In this figure, the red background is the toluene, which contains suspended 200 nm red fluorescent particles (not used in FRET experiments, used here to show proof of concept), and the green spots are the water droplets containing biotin-4-fluorescein. For the pendant droplet experiments, biotin-4-fluorescein is not used because upon streptavidin binding this molecule exhibits static quenching since the fluorescein and the streptavidin molecules become too close to each other. Biotinylated fluorescent beads avoid physical quenching and offer additional advantage. Since these beads are made of polystyrene, they accumulate around the water phase and form colloidosomes, which makes the streptavidin-biotin binding reaction much efficient.

C. Results and Discussion

High optical intensities in microdroplets increase the energy transfer efficiency for FRET pairs, resulting in a high sensitivity biodetection scheme. The binding reaction between a biotinylated fluorescent bead and streptavidin-Alexa Fluor 555 in microdroplets was studied previously as described in Chapter 5. Upon avidin-biotin binding, the donor (yellow fluorescent dye in biotinylated bead) and the acceptor (Alexa Fluor 555) come into close proximity, which allows FRET to occur. In a microdroplet, the emission from the donor molecules (in fluorescent beads) can be coupled to the optical resonances of the microdroplet and increase the donor emission lifetime. This can result in much a longer Förster radius than expected normally for this FRET pair. This energy transfer pattern was achieved with microdroplets with a further decrease in donor emission fluorescence and a corresponding increase in acceptor emission because of enhanced energy transfer efficiency. The morphology dependent resonances based on the bulk fluores-

Reproduced with permission of the copyright owner. Further reproduction prohibited without permission.

cence emission spectrum of fluorescent beads and Alexa Fluor 555 were observed as well.

The resonances inside a microdroplet occur mostly around the rim and the thickness of the shell around the droplet rim where the resonances occur is given by (6.1). Successful use of optical resonances inside microdroplets for immunoassays based on FRET depends on efficient coupling of the donor and acceptor emission to these optical resonances. To achieve this, the binding reaction must either occur around the rim or the bound molecules should somehow be carried to the optically active region of the microdroplet. In a microdroplet, this can be done by two ways. One of them is to make the avidin-biotin complex lipophilic, so that a fraction of the molecules accumulate at the microdroplet surface. This approach will be described in Chapter 8 as a future project. Another approach is to use emulsions. The binding reaction for the immunoassay can be engineered to happen at the water-oil interface of an emulsion (water-in-oil). Because of the specific gravity difference between the oil and water phase, the water phase will eventually end up at the droplet rim.

The emulsion approach is depicted in Figure 6.3. The microdroplet consists of a water-in-oil emulsion where the oil phase contains the biotin-donor molecule and the water phase contains the avidin-acceptor molecule. The avidin-biotin binding reaction occurs at the water-oil interface. Since the specific gravity of the water phase is larger than the oil phase, the water phase accumulates at the microdroplet air interface. This facilitates the interaction of the optical resonances inside the pendant droplet with the donor and the acceptor molecules

Reproduced with permission of the copyright owner. Further reproduction prohibited without permission.

bound to the avidin-biotin pair, since most of the bound complex exists at the water-oil interface.

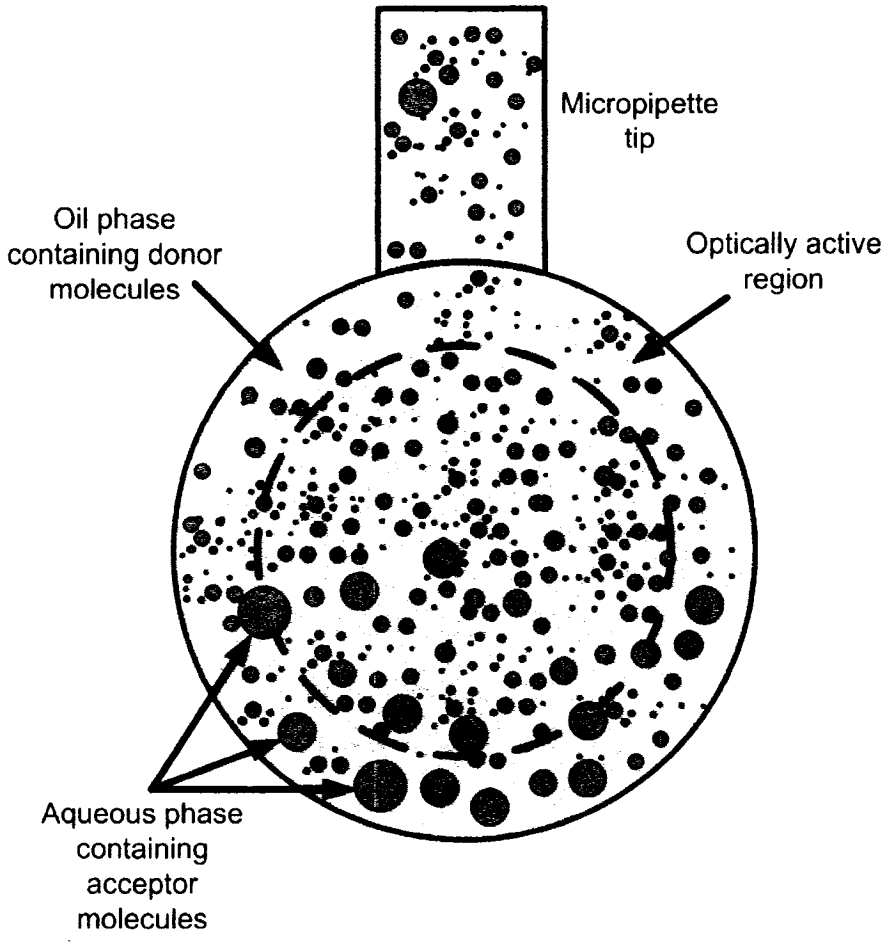

Figure 6.3 Using emulsion approach in pendant microdroplet experiments. The microdroplet consists of a water-in-oil emulsion where the oil phase contains the biotin-donor molecule and the water phase contains the avidin-acceptor molecule. The avidin-biotin binding reaction occurs at the water-oil interface. Since the specific gravity of the water phase is larger than the oil phase, the water phase accumulates at the microdroplet air interface.

The emulsion approach for improving the detection sensitivity of the immunoassay depends on the effects of diffusion and gravity inside the microdroplet. The time scale for these effects to result in a major difference in detection efficiency is on the order of seconds. The interaction of the excitation laser and the microdroplet produced by a Vibrating Orifice Aerosol Generator or a piezo drop-on-demand system is on the order of milliseconds. Thus, the necessary time

Reproduced with permission of the copyright owner. Further reproduction prohibited without permission.

scale cannot be obtained by producing individual droplets into air with these two droplet generation mechanisms to observe an enhanced effect due to phase separation through the approaches described above for sensitivity improvement. So instead of a dynamic droplet generation mechanism, we used a pendant droplet technique where the microdroplet produced is not perfectly spherical but still can sustain resonances.[126-128]

Through the use of the pendant droplet technique, it is possible to achieve the necessary time scale for diffusion and gravity to take effect and produce the necessary transfer of the bound antibody-antigen molecules closer to the micro-droplet surface. For example, the diffusion length for a 1 μm aqueous particle to diffuse in silicone oil in 5 minutes is approximately 13 μm. The average distance that a 10 μm droplet travels in 10 minutes moving at terminal velocity due to gravity is 7.2 μm. For smaller droplets in the emulsion, the main transfer mechanism would be diffusion since gravitational force will be damped by drag forces. For larger droplets, the Stokes-Einstein diffusion coefficient is smaller, so the main mechanism for transport is gravity. Due to the combined effect of diffusion and gravity, the aqueous phase in the emulsion is observed to concentrate at the droplet rim within 5 to 10 minute time scale. Waiting for a longer period for these effects to take place may lead to better results, but it also entails other problems for data acquisition. Although droplet size does not change significantly due to evaporation since pendant droplet setup allows us to avoid this by capillary action feeding through the micropipette tip; waiting for longer period of time makes it harder to maintain the initial droplet conditions before data acquisition.

The water-in-oil emulsion containing the donor (biotinylated fluorescent beads) and the acceptor (streptavidin-Alexa Fluor 610) molecules is prepared

Reproduced with permission of the copyright owner. Further reproduction prohibited without permission.

(see Methods and Materials) and used to form a pendant droplet at the tip of a micropipette. The typical droplet size is less than 200 μm.

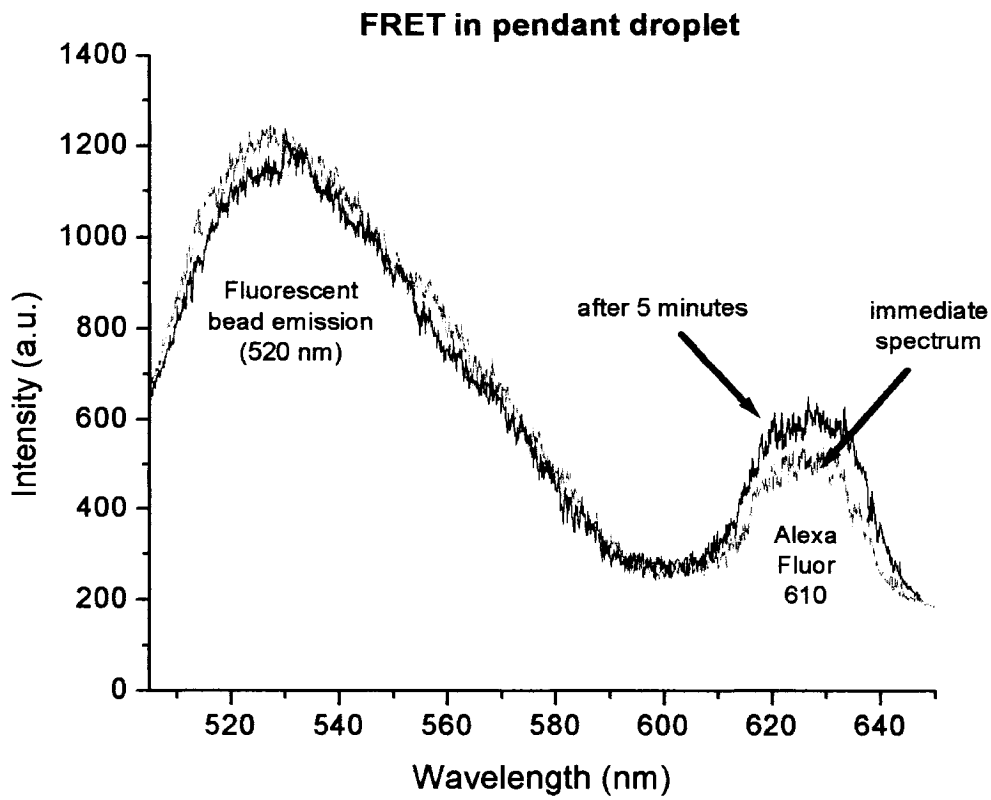

Figure 6.4 Results of the pendant droplet experiment using emulsion approach. As the bound streptavidin-biotin molecules (thus donor-acceptor molecules) move to the region where optical resonances occur, the detection efficiency increases. The figure shows two spectra: black solid line shows the initial FRET spectrum of the yellow fluorescent bead and Alexa Fluor 610 after the pendant droplet is ejected. After five minutes, a slight increase is observed in the Alexa Fluor 610 emission peak (red solid line). The donor emission peak does not show any major change, since the number of donor molecules in the optically active region does not change significantly due to the transfer of the aqueous phase inside the pendant droplet. Here, 0.019% solids 1 μm biotinylated yellow-green FluoSphere fluorescent bead solution is dried and resuspended in dodecane. 2 mg/ml streptavidin-Alexa Fluor 610 solution is mixed with FluoSphere/dodecane suspension to obtain the emulsion (2% by volume). This emulsion is used to produce pendant droplets of approximately 200 μm in diameter.

The biotinylated fluorescent beads accumulate around the water phase and the biotin groups interact with the streptavidin-Alexa Fluor conjugate at the water-oil interface. Upon binding, donor and acceptor molecules come to close proximity, allowing FRET to occur. Since the emulsion is prepared before pendant droplet formation, it is possible to observe FRET immediately after the pendant

Reproduced with permission of the copyright owner. Further reproduction prohibited without permission.

droplet is ejected from the micropipette tip and excited by the Argon ion laser. As time elapses, gravitational and diffusional effects take place transferring a large portion of the aqueous phase carrying the bound avidin-biotin molecules closer to the pendant droplet rim. As seen in Figure 6.4, as the bound streptavidin-biotin molecules (thus donor-acceptor molecules) move to the region where optical resonances occur, the detection efficiency increases. The figure shows two spectra: one shows the initial FRET spectrum of the yellow fluorescent bead and Alexa Fluor 610 after the pendant droplet is ejected. After five minutes, a slight increase is observed in the Alexa Fluor 610 emission peak. The donor emission peak does not show any major change, since the number of donor molecules in the optically active region does not change significantly due to the transfer of the aqueous phase inside the pendant droplet.

One important difference between the conventional droplet experiments and the pendant droplet experiments is in the observation of the resonance peaks. In pendant droplet experiments, observation of the resonance peaks is sensitively dependent on the morphology of the droplets. One can merely observe the MDRs, if the droplet size is small enough and the droplet shape is close to a sphere. If the pendant droplet is large (larger than 300 μm), then the resonant peaks are suppressed by the bulk fluorescence signal from the inner regions of the droplet which does not couple into the MDRs. In better cases, the resonant peaks are observed on top of the bulk fluorescent signal. To show this effect, spectra from the droplet growth experiments are shown in Figure 6.5. Twenty-five consecutive spectra are taken as a Rhodamine 6G containing pendant water droplet is evolving at the micropipette tip. Initially, since the droplet is small, we observe the red-shifted emission peak around 575 nm, which is typical for the

Reproduced with permission of the copyright owner. Further reproduction prohibited without permission.

fluorescence emission coupled to MDRs of a microdroplet. The relatively small resonant peaks can be observed on top of this main resonant peak. As the droplet grows, the red emission peak starts diminishing and the bulk fluorescence intensity due to Rhodamine 6G (at 550 nm) increases. For smaller droplets, the resonant peaks are more evident. Figure 6.6 shows part of the resonant spectrum of a small pendant water droplet containing biotin-4-fluorescein. Here, small resonant features appear on top of the broad fluorescence spectrum.

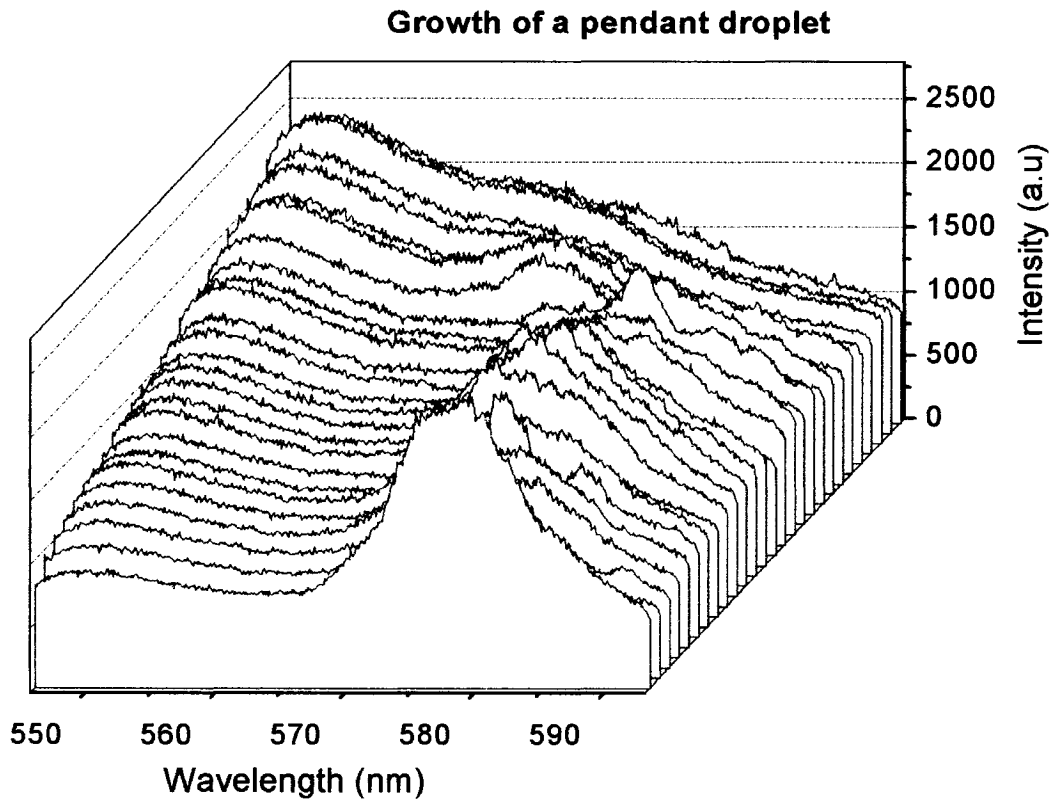

Figure 6.5 Transition between the bulk emission and the emission coupled to the resonances of a pendant droplet as the droplet grows. Twenty-five consecutive spectra taken as a Rhodamine 6G containing pendant water droplet is ejected through a micropipette tip. As the droplet grows the resonant spectra disappears leaving behind the bulk fluorescence spectra from Rhodamine 6G.

Reproduced with permission of the copyright owner. Further reproduction prohibited without permission.

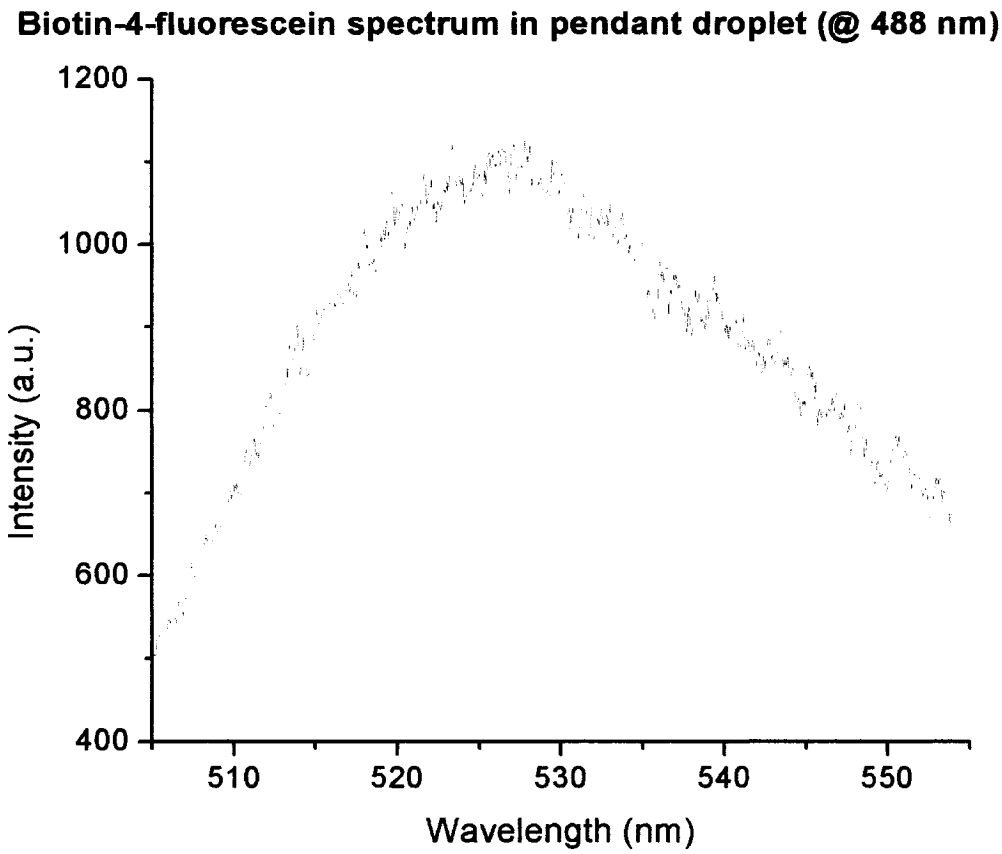

Figure 6.6 Biotin-4-fluorescein emission spectrum in a pendant droplet. Part of the resonant spectrum (from 505-555 nm) from a small pendant water droplet containing biotin-4-fluorescein excited at 488 nm is shown here.

Reproduced with permission of the copyright owner. Further reproduction prohibited without permission.

Chapter 7

Lasing Droplets in a Microfabricated Channel

A. Introduction

As pointed out in Chapter 3, morphology dependent resonances have recently found many applications in optical communications[129, 130] and biosensing.[33, 34, 68, 69, 72, 78, 86, 131] The utilization of the high-Q resonances in biosensing offers specific advantages such as a small sample volume and high sensitivity. Optical cavity geometries can include spheres[34, 69, 72], disks (or toroids)[33, 86] and cylinders.[78, 131] Since the refractive index of the optical cavity should be higher than the surrounding medium to confine the light inside by total internal reflection, silicon or glass can be used when the surrounding medium is water or air. However, it is often desirable to use the liquid medium containing the analyte as the optical cavity to minimize the interaction between the analyte and the surroundings. So far,

Reproduced with permission of the copyright owner. Further reproduction prohibited without permission.

this has been achieved by producing microdroplets into air.[132, 133] In this chapter, we describe for the first time to our knowledge, lasing spherical microdroplets in a microfabricated device. Through coupling MDRs to a minute liquid sample, this technique has the potential to provide high sensitivity for chemical and biological detection. The results discussed in this chapter have been submitted to Optics Letters for publication.

B. Methods and Materials

To achieve MDRs in a spherical liquid microcavity, a miniaturized device, was microfabricated with a T-junction configuration to produce roughly 50 μm diameter water droplets into an oil phase in a microchannel (Figure 7.1). The details of the microfabrication process are described in Appendix A.

The T-junction (Figure 7.1, inset) in this device consists of a 30-μm-wide channel (transporting the water phase) opening into a perpendicular 50-μm-wide channel (transporting the oil phase). The water phase is dispersed into the oil phase (flowing perpendicular to the water phase) forming a water-into-oil (W/O) emulsion at the junction of these two microchannels. The dispersed water phase initially forms small plugs in the oil phase by breaking up into the 50-μm-wide microchannel due to the shear stress caused by the fast oil flow. Approximately 500 μm downstream from the T-junction, the 50-μm-wide channel carrying the emulsion widens out to 200 μm. At this point, the water plugs form individual spherical droplets due to surface tension and the hydrophobicity of the microchannel walls. This design also helps to slow down the droplets for excitation and detection of the optical resonances through the integrated optical fibers in the device.

Reproduced with permission of the copyright owner. Further reproduction prohibited without permission.

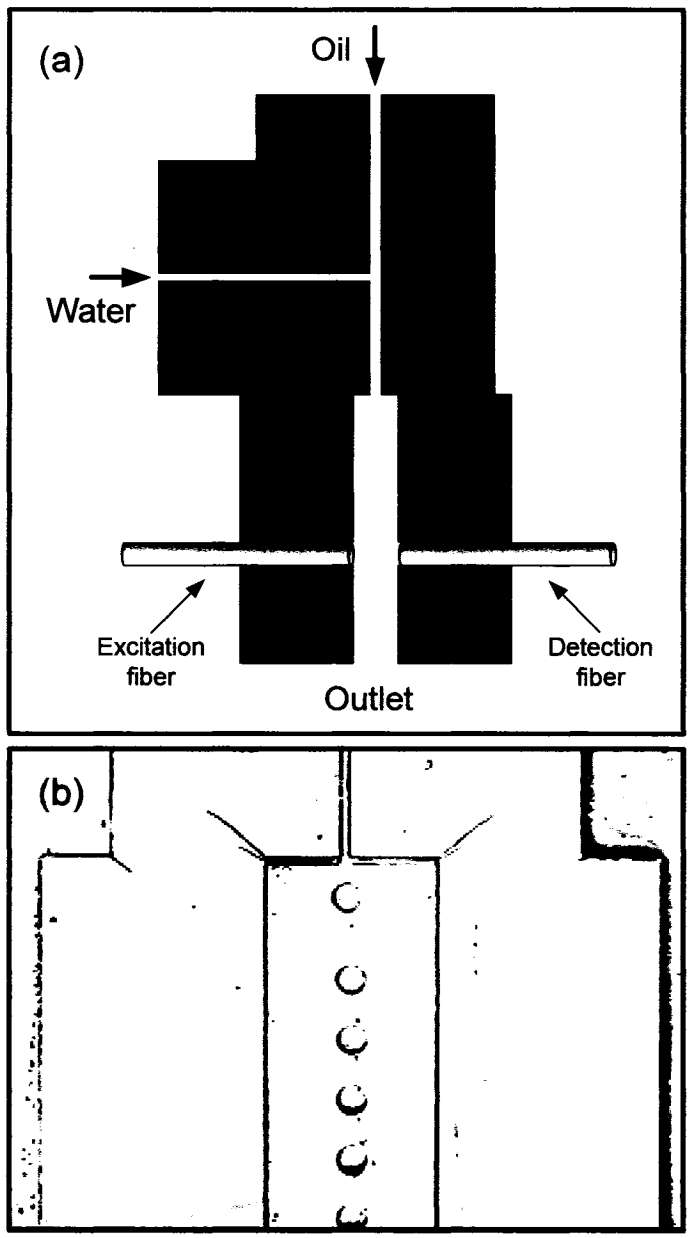

Figure 7.1 The layout of the microfabricated droplet generator. The microfluidic device has a T-junction configuration. A 30-μm-wide channel opens up to a 50-μm-wide perpendicular channel. The narrow channel carries an immiscible liquid which breaks up into droplets at the T-junction due to shear stress as a result of the fast flow in the wide perpendicular channel.

When generating microdroplets with a T-junction design, the droplet size is usually comparable to the size of the microchannel carrying the oil phase and the droplet frequency typically depends on the ratio of the flow rates of the water

Reproduced with permission of the copyright owner. Further reproduction prohibited without permission.

phase and the oil phase.[134-136] For our device, the width and depth of the microchannel carrying the oil phase was 50 and 110 μm respectively. The diameter of the droplets was 50-60 μm. This corresponds to a 65-113 pL volume for each droplet. Droplet production rates vary roughly between 20-60 Hz. This droplet production rate is at least an order of magnitude smaller than the previously reported droplet generation rates using a T-junction or a flow-focusing design[134-136], allowing us to setup an efficient optical detection system as described below.

Both the water and the oil phase are pumped with a syringe pump at a flow rate ranging between 10-30 μL/hr and 0.5-1.5 mL/hr respectively. The experiments consume only about 50 μL of fluorescent sample (water phase) and 1 mL of oil phase to generate droplets and collect spectra. Rhodamine 6G or Fluorescein is dissolved in the water phase at a final concentration of 10 μM and excited with a laser through optical fibers integrated into the microfabricated device to attain MDRs in the microdroplets.

The outline of the experimental setup comprising the droplet generator, excitation and detection system is depicted in Figure 7.2. The spherical droplets are first detected, and then excited by a set of two multimode fibers located 500 μm downstream from the junction of the channels. The fibers face each other and are positioned perpendicular to the droplet stream. Synchronization of the excitation and fluorescent detection with the droplet production is realized through detection of He-Ne laser scattering off the microdroplets. The He-Ne laser is delivered via one of the multimode fibers into the microchannel; as the droplets pass by the fibers, the scattered light from the illuminated droplets is collected by the second multimode fiber (which is coupled to a photodiode) directly across from the excitation fiber. The change in the backscattered laser light due to droplet

Reproduced with permission of the copyright owner. Further reproduction prohibited without permission.

presence is detected by the photodiode and used as a trigger for the excitation laser for the lasing experiments. The droplet detection signal from the photodiode is sent to a delay generator (SRS, Palo Alto, CA) which synchronizes the excitation laser and the spectrometer. The excitation laser (either a Nd:YAG or an Argon ion laser) is coupled to the same multimode fiber that is used for delivering the He-Ne laser into the microchannel for droplet detection. To introduce the detection and excitation lasers through the same fiber, a 45^0 degree dichroic filter (Edmund Optics, Barrington, NJ) and a fiber coupler (Newport, Irvine, CA) is used. The fluorescence emission from the droplets is collected by a long working distance Apochromat lens normal to the plane of the droplet generator device.

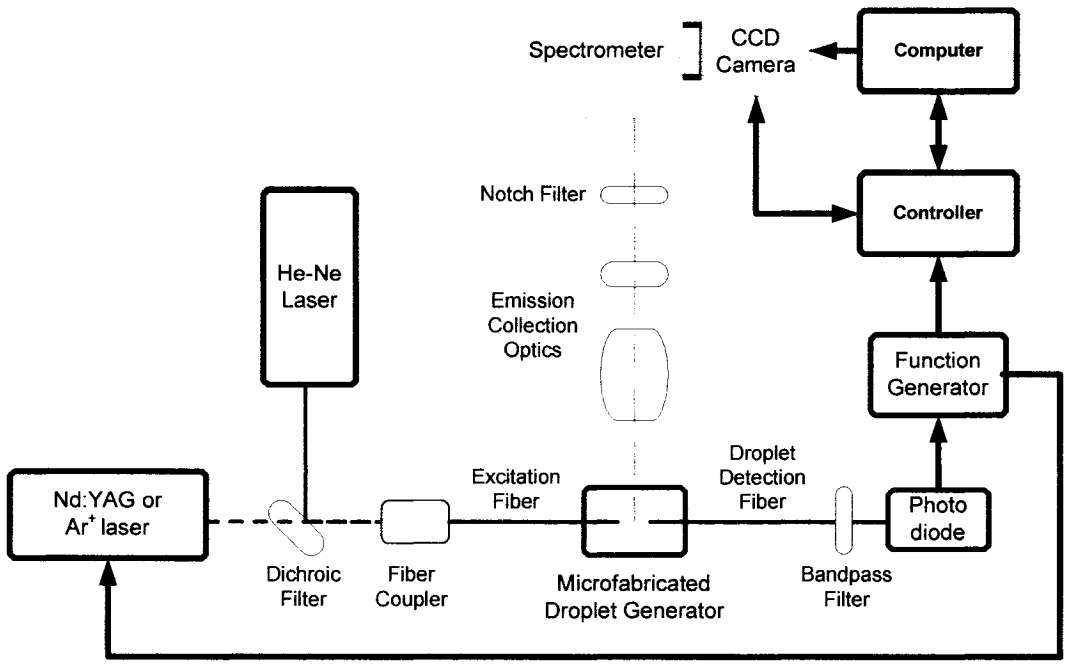

Figure 7.2 Experimental setup for optical resonance experiments in microdroplets produced in a T-junction microfluidic device. The water and the oil phase are introduced into the microfluidic device by two syringe pumps through a custom stainless steel (clamp) interconnect. Two multimode fibers integrated into the device to deliver two lasers; He-Ne laser for droplet detection using droplet scattering (for synchronization) and Nd:YAG or Argon ion for exciting the dyes in the microdroplets to obtain lasing.

Reproduced with permission of the copyright owner. Further reproduction prohibited without permission.

C. Results and Discussion

To obtain optical resonances within a microcavity, the refractive index of the microcavity must be higher than the surrounding medium. This is readily achieved in microdroplets in air. To realize total internal reflection in a microdroplet produced in a microchannel, the surrounding liquid medium should have a lower refractive index. For this purpose, a low refractive index laser liquid (n=1.293 at 25°C, Cargille Labs, Cedar Grove, NJ) is used as the oil phase.

Initially, the fluorescent dyes (Rhodamine 6G or Fluorescein) are dissolved in deionized water where the relative refractive index of the water phase (n=1.332) with respect to the oil phase (n=1.293) was only 1.03. In this case, no MDRs were observed as the droplets were excited with the laser (data not shown). On the other hand, an experimental demonstration of MDRs coupled to a polystyrene microsphere (n=1.59) with a relative refractive index of as low as 1.09 (surrounding medium, n= 1.457) has been reported.[137]

As the relative refractive index between the water phase and the oil phase is increased to 1.1 by adding glycerol to the water phase, MDRs are observed. The refractive index of the mixture was (n=1.428) when the water phase with the fluorescent dye is mixed with 70% glycerol by weight. Figure 7.3 (a-j) shows the ejection of a 50-μm-diameter droplet containing 10 μM Rhodamine 6G dye and its illumination by the Nd:YAG laser through the optical fiber. A strobe light was exploited to assist in the capture of the droplet ejection by a CCD camera. The two dark images show the illumination and the excitation of a microdroplet in greater detail. In the left image, the droplet was illuminated partially and the scattering from the laser is also detected. The image on the right was obtained by blocking

Reproduced with permission of the copyright owner. Further reproduction prohibited without permission.

the scattered laser light through a notch filter – it clearly demonstrates the lasing emission (red) at the circumference of the droplet. The fluorescence emission (from the dye) corresponding to MDRs confined near the droplet rim are observed as a bright red shell and it is easy to tell it apart from the bulk fluorescence (orange) from the inner region of the droplet.

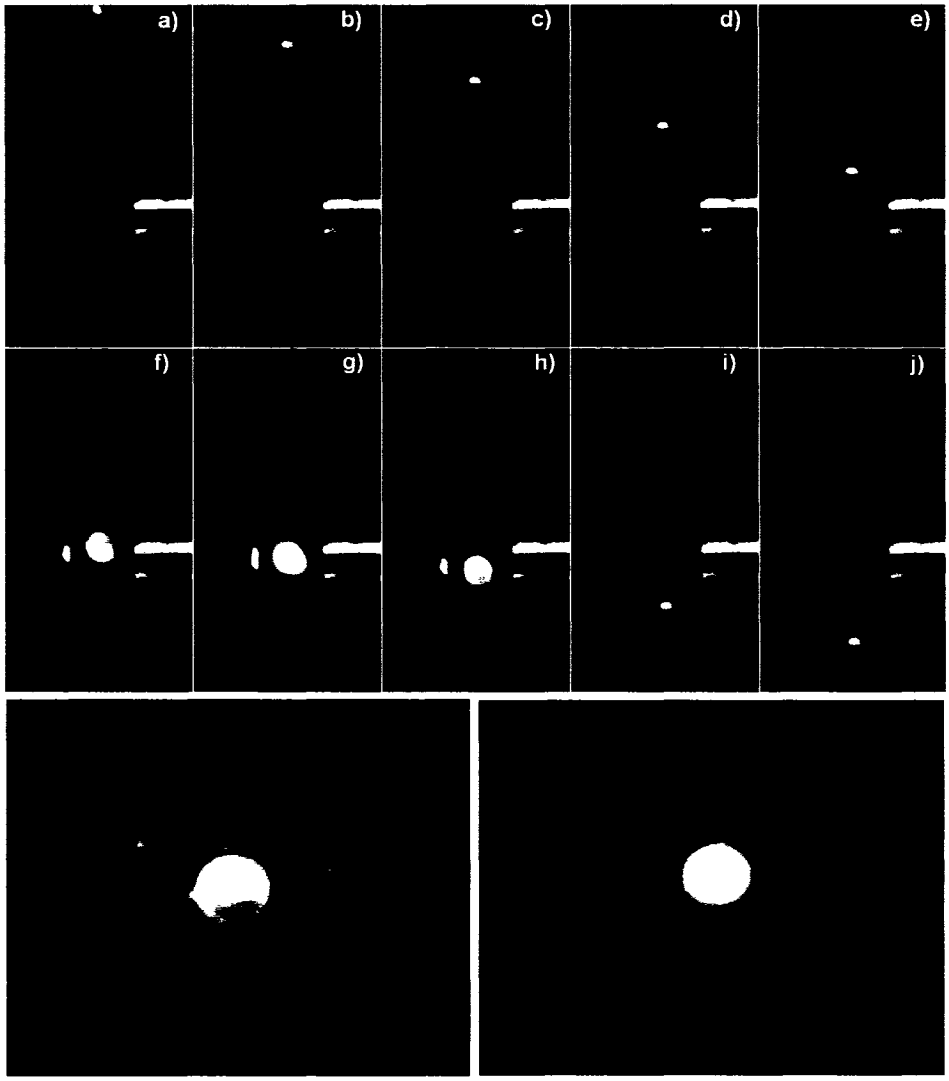

Figure 7.3 Droplet lasing in a microchannel. Upper section (a-j) shows the droplet ejection through the T-junction device. After the ejection, the droplet is excited with the laser through a multimode fiber integrated into the microchannel. The two figures (below) show lasing images from Rhodamine 6G doped liquid microdroplets excited with a pulsed Nd:YAG laser (532 nm). The left image shows some green laser scattering whereas the pump laser is filtered with a 532 nm notch filter on the right image. The bulk fluorescence emission (orange) is observed from the interior region of the droplets. The strong red emission is observed near the rim due to lasing.

Reproduced with permission of the copyright owner. Further reproduction prohibited without permission.

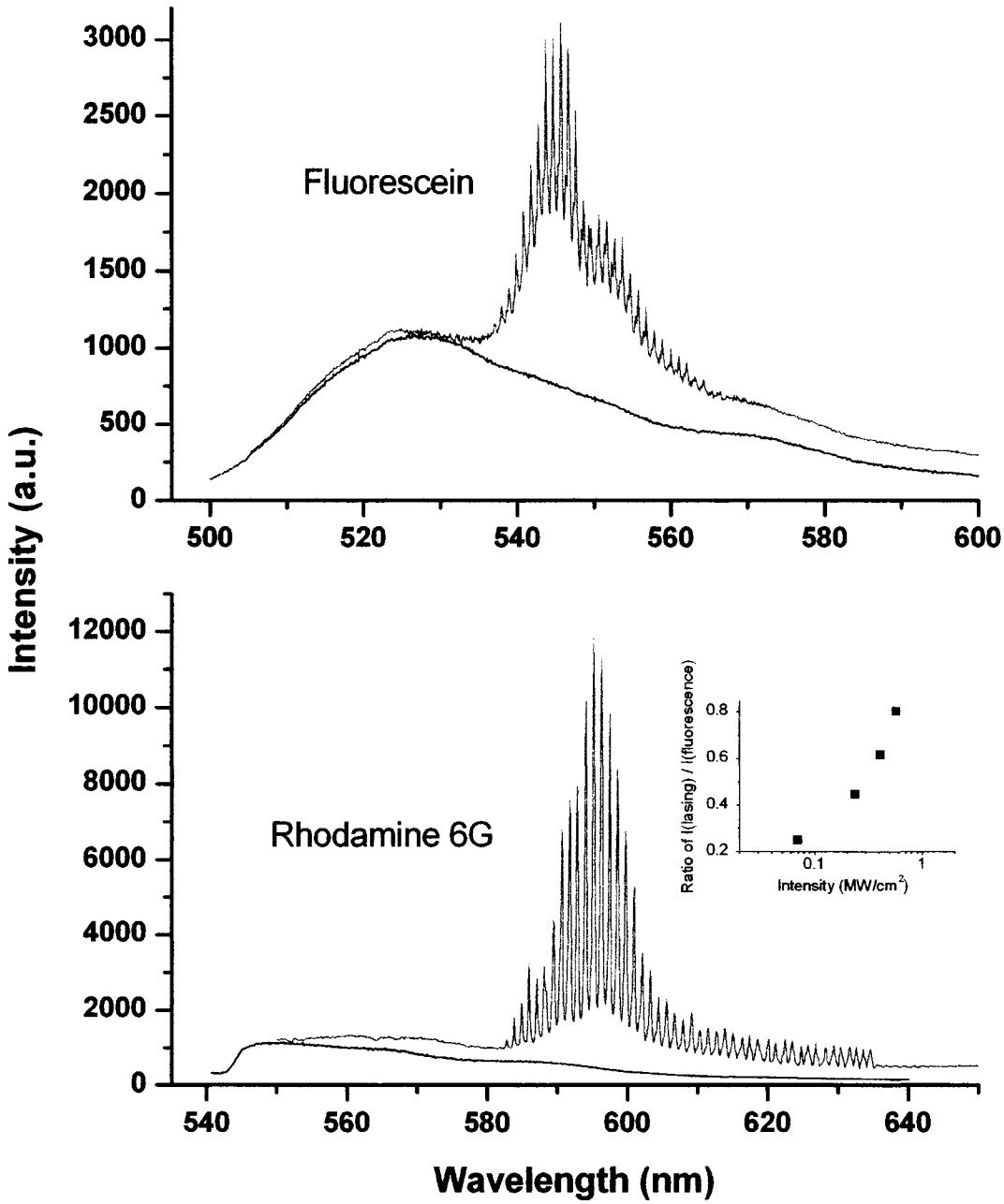

Figure 7.4 Lasing spectra from 50-60 μm diameter water-glycerol droplets containing 10 μM Rhodamine 6G or Fluorescein. The MDR spectrum confirms the observation of lasing emission through droplet images. The lasing spectrum is red shifted compared to the bulk fluorescence emission (where the absorption from the dye molecules is weak). The inset shows the nonlinear dependence of lasing emission intensity upon pump laser intensity.

The emission spectrum from the droplets confirms the observation of lasing through the droplet images (Figure 7.4). For both Fluorescein and Rhodamine 6G, the MDR peaks are superimposed on the broad emission spectra

Reproduced with permission of the copyright owner. Further reproduction prohibited without permission.

of each dye. The resonance peaks occur at longer wavelengths compared to the bulk emission spectrum peaks for both dyes. The maximum intensity is observed at 545 nm and 595 nm for the lasing peaks as opposed to 527 nm and 550 nm for the bulk fluorescence for Fluorescein and Rhodamine 6G respectively. The absorption spectrum of Rhodamine 6G has a peak at ~530 nm and the tail reaches 585 nm. So lasing is expected at the low absorption region of 585-640 nm for this dye. The absorption spectrum of Fluorescein has a peak at ~490 nm and the tail reaches 535 nm. Lasing for this dye is also observed at the low absorption region (535-560 nm) although the bulk fluorescence emission peaks at 527 nm.

The spectral data is in excellent agreement with the images from the droplets containing Rhodamine 6G where bright red lasing emission trapped near the droplet rim is observed along with the orange bulk fluorescence signal from the inner regions. Similarly, images from droplets containing Fluorescein displayed a yellow bulk fluorescent emission profile at the droplet center with bright orange lasing emission trapped near the rim (data not shown).

The integrated intensity from the lasing spectrum is measured as a function of the pump laser intensity for Rhodamine 6G. As depicted in the inset of Figure 7.4, the ratio of the total intensity from the lasing region (585-600 nm) and the absorbing region (550-585 nm) increases with increasing Nd:YAG laser power (~0.5 MW/cm^2). The emission in the (585-600 nm) region shows nonlinear dependence on the laser power which is typical to lasing as a result of optical gains dominating over absorption losses and radiation leakage.

Reproduced with permission of the copyright owner. Further reproduction prohibited without permission.

Chapter 8

Conclusion

A. Summary

In Chapters 4 through 7, it has been shown that optical resonances in microdroplets can be used for biosensing applications. An indirect detection mechanism (without any specific labeling) was employed to detect single bacterial cells. A direct detection mechanism (FRET-based immunoassay) was exploited to detect the binding reaction between two biomolecules (avidin-biotin) at low concentrations. A microfluidic device has been designed and fabricated to integrate the droplet generation, excitation of the fluorescent dyes and the detection of emission spectrum from microdroplets. This microdevice has the potential for future lab-on-chip applications of optical resonance-based high-throughput biosensing.

The detection of single bacterial cells through optical resonances has been demonstrated in microdroplets. The conventional Vibrating Orifice Aerosol Generator has been replaced with a custom a drop-on-demand piezo inkjet

Reproduced with permission of the copyright owner. Further reproduction prohibited without permission.

printhead. With the new setup, it is possible to address every individual droplet with improved excitation/detection stability enabling high throughput non-specific detection of single E. Coli cells without any labeling. The cells inside the micro-droplet have a direct effect on the morphology dependent resonances that are supported by Rhodamine 6G fluorescence; modification of the resonances arises from changes due to scattering and changes in the local refractive index. The change in the optical resonance spectrum can be observed at low concentrations where each microdroplet contains as little as one cell.

Optical resonances in microdroplets were also used for the sensitive detection of binding reactions between avidin and biotin through FRET. The use of a biotinylated fluorescent bead and streptavidin-Alexa Fluor 555 interaction caused a decrease in donor emission that was associated with an increase in acceptor emission. This energy transfer can be enhanced in a microdroplet because both the donor and the acceptor emission can be coupled to the optical resonances of microdroplet. Since the fluorescence lifetime can be increased inside the micro-droplet and the coupled fluorescence emission can travel long distances around the droplet rim, a radiative energy transfer between FRET pairs is achieved and the detection limit can be improved. This phenomenon is equivalent to an effective increase in Forster radius or in FRET efficiency for FRET pairs. This detection method can be applied to a variety of immunoassay formats.

If the number of donor-acceptor pair molecules in the optically active region – where MDRs occur – can be increased, the sensitivity of the detection for the immunoassay reaction can also be increased. This is critical to increase the sensitivity of the detection mechanism utilizing optical resonances in microcavities. By transferring the avidin-biotin complex to the pendant microdroplet rim, a

Reproduced with permission of the copyright owner. Further reproduction prohibited without permission.

better interaction between the donor-acceptor pair and the optical resonances is established. This was achieved by using an emulsion to initiate the binding reaction and then transferring the aqueous phase to the pendant droplet rim.

Finally, lasing from dye-doped microdroplets ejected into a surrounding liquid medium has been observed. Through the microfabricated droplet generation device described in Chapter 7, it is possible to produce and analyze picoliter size droplets with an initial sample volume as small as 50 μL. The high-Q resonances observed can be used as an ultrasensitive detection mechanism for high throughput chemical and biological sensing.

B. Future Work

Lately, single atom detection[87] has been proposed using optical resonators which evidently shows the high potential of whispering gallery modes for sensing applications. The successful demonstration of biological (cell and immunoassay) sensing application through optical resonances in microdroplets opens up new possibilities for further investigations and raises stimulating questions to answer. Additional studies may be pursued to increase the sensitivity of detection.

One of the main obstacles is to overcome the specificity problem that is encountered with the indirect detection scheme (as discussed in Chapter 4) in detecting single E. Coli cells. This problem may be resolved through specific binding of the target to a known chemical or biological agent. But this would convert the indirect detection mechanism to a direct one which may not be ideal in some cases.

Another major hurdle is that the molecules/particles should be located in the optically active region of the microdroplet to be detected through the changes

Reproduced with permission of the copyright owner. Further reproduction prohibited without permission.

in the optical resonances. Successful use of optical resonances inside microdroplets for immunoassays based on FRET depends on efficient coupling of the donor and acceptor emission to these optical resonances. To achieve this, the binding reaction must either occur around the rim or the bound molecules should somehow be carried to the optically active region of the microdroplet. In a microdroplet, this can be done by two ways. One of them is to use an emulsion approach which is described in Chapter 6. Another approach is to make the avidin-biotin complex lipophilic, so that part of the molecules accumulate at the microdroplet surface. This can be done by engineering an immunoassay where either the antibody or antigen is conjugated to a lipophilic dye. There are commercially available lipophilic dyes (e.g. DiI, Molecular Probes, Eugene, OR) or fluorescent phospholipids (e.g. biotinylated fluorescent phospholipids, Avanti Polar Lipids, Alabaster, AL). These molecules can be employed in an immunoassay format to detect binding of an antigen. If the pendant droplet approach is utilized as described in Chapter 6, the bound complex will accumulate at the droplet-air interface due to the lipophilic nature of the reagents.

Optical resonances also affect the donor emission lifetime due to high optical mode intensities within the microcavity. This effect can easily be observed in small microcavities (<10 μm) for fluorescent particles with relatively long lifetimes. Especially lanthanide chelates or nanoparticles can be studied in small microdroplets. Since FRET can be established between a fluorescent nanoparticle (as donor) and an organic dye molecule (as acceptor), immunoassays can be performed by using antibody/antigen conjugated lanthanide nanoparticles and conventional organic dyes. Fluorescence lifetime measurements can be used as supporting data (besides spectral data) to confirm FRET upon binding reaction

Reproduced with permission of the copyright owner. Further reproduction prohibited without permission.

between the biomolecules. Lanthanide particles offer long fluorescence lifetime (up to milliseconds) and large Stokes shift, and are therefore attractive for biosensing applications.

Here, two novel projects are proposed that can be implemented as an application of optical resonances for chemical and biological sensing.

1. Microspheres fused/attached on a coverslip excited by TIR

As described in Chapter 3, a spheroid-shaped optical fiber tip can be used as a biosensor.[34] In this example, optical resonances are evanescently coupled to the microcavity (a melted fiber tip ~300 μm in diameter) through an eroded single mode fiber. A similar approach coupling the optical resonances to a microsphere through a fiber prism has also been reported.[73] These two approaches are elaborate since they require careful preparation and alignment of the microcavity and the optical fiber.

Here, a much simpler and versatile method is proposed. The microcavity is a polystyrene or silica bead fused to the surface of a microscope coverslip. This can be achieved in several ways. The microspheres spread on a coverslip can be heated up close to the glass transition temperature and stay at that temperature short enough so that only the very bottom of each microsphere is fused to the coverslip. Another method would be to use a diluted acid bath (1% HCl, 5 minutes) to fuse the beads on a glass coverslip.

Reproduced with permission of the copyright owner. Further reproduction prohibited without permission.

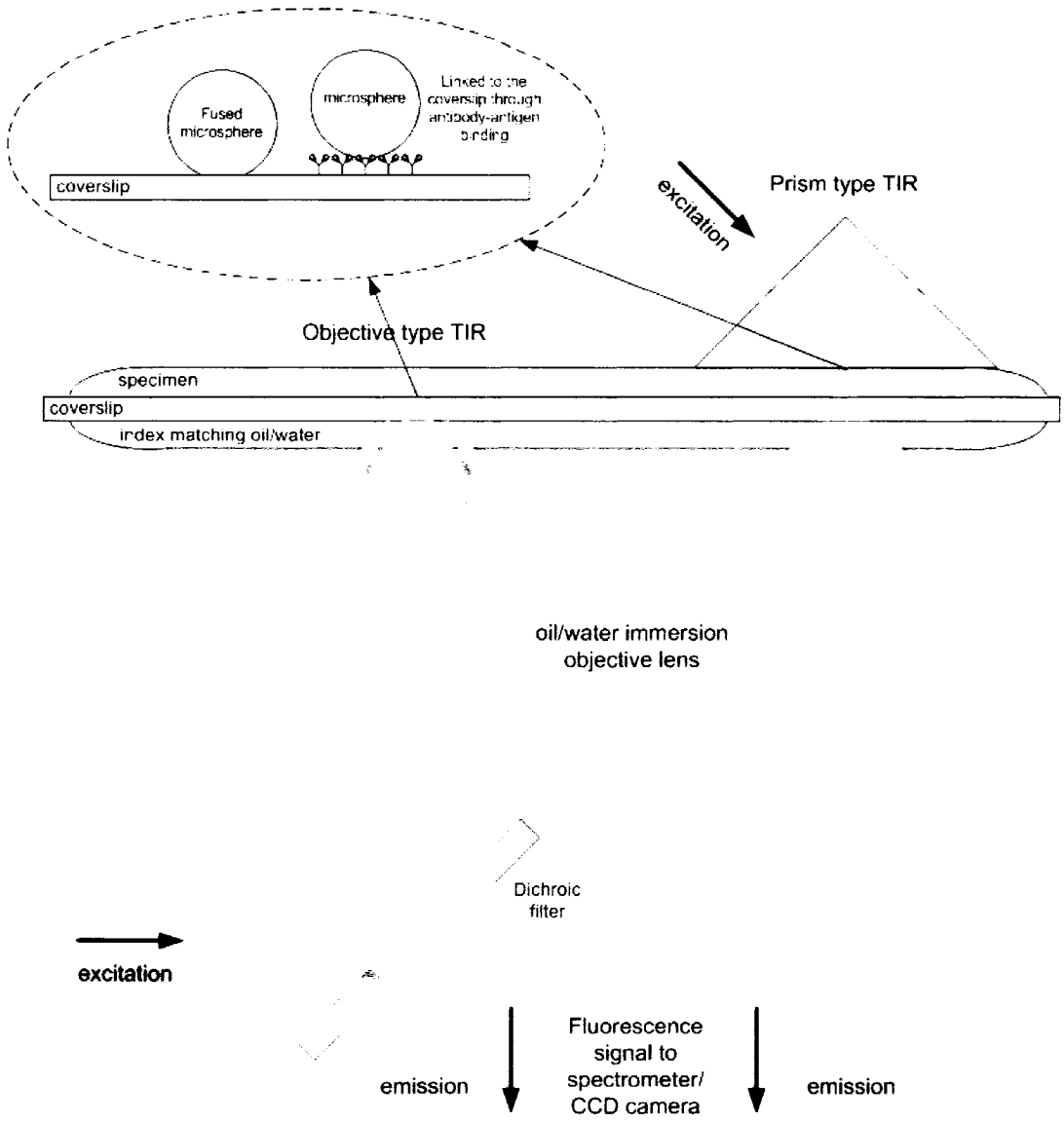

Figure 8.1 Microspheres fused/attached on a coverslip and optical resonances are excited by Total Internal Reflection. The microspheres can be attached to the glass surface by either fusing them or binding them through antibody-antigen reaction. The optical resonances can be excited by Total Internal Reflection through an objective type or a prism type setup. The evanescent wave, extending beyond the coverslip into the specimen region, will efficiently couple into the optical resonances of the microspheres.

The optical resonances of the microspheres fused onto the glass coverslip are excited through the evanescent wave of the beam (delivered by a microscope objective or a prism) undergoing total internal reflection inside the coverslip.[§] The

[§] This is actually Total Internal Reflection Microscopy, a commonly used technique in biology.

Reproduced with permission of the copyright owner. Further reproduction prohibited without permission.

emission is collected through the same objective lens and the excitation light is blocked by a dichroic filter and an emission filter. A water or oil immersion objective lens with high NA would yield efficient coupling of excitation and collection of emission signal by reducing the losses due to scattering and collecting more photons respectively.

In this setup, the size of the microcavity is totally controllable, since a specific size of bead can be purchased and fused onto the surface. Different bead sizes can be tested to optimize results. The beads can be fluorescent or non-fluorescent. In case of non-fluorescent beads, a tunable laser should be used to find the specific wavelength that would couple into the optical resonances of the bead of choice. If the beads are fluorescent, then the optical resonances observed would be based on the bulk fluorescence emission of the dye molecules embedded in the beads.

In an ideal experiment, the fluorescent beads fused onto the coverslip are excited through TIR and the corresponding optical resonances are recorded. The microspheres can be coated with a specific antibody of choice through adsorption. A solution containing antigens can be introduced into the medium and the shift in the optical resonances is observed throughout the immunoassay reaction. The nonspecific binding of the antigens can be avoided through a blocking agent such as BSA or casein.

2. Monodisperse microsphere stream in a microfabricated channel

Microdroplets produced in a microfluidic device integrated with optical fibers can be used as a miniaturized biosensor as shown in Chapter 7. This device can be simplified and its reliability can be improved as described below.

Reproduced with permission of the copyright owner. Further reproduction prohibited without permission.

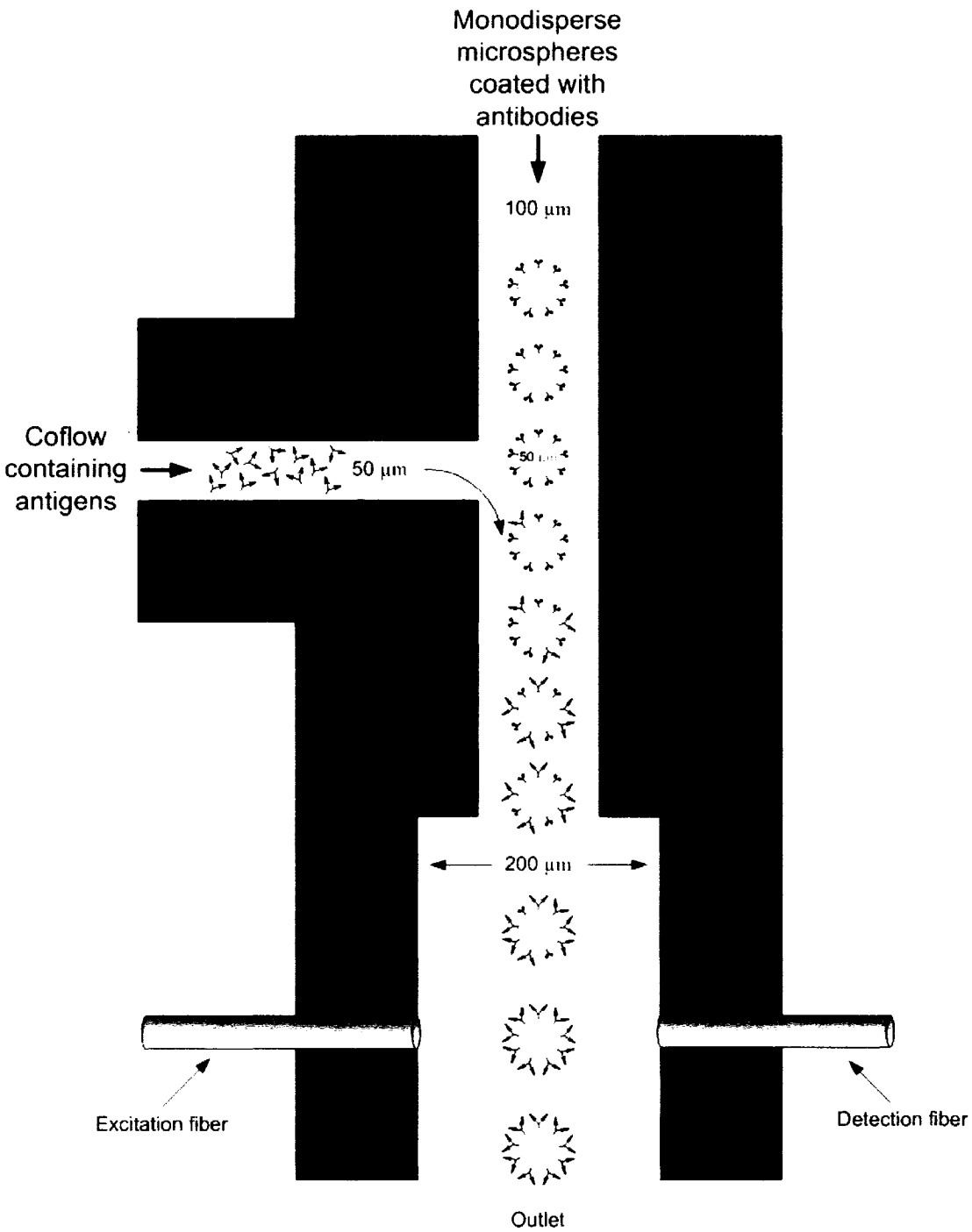

Figure 8.2 Monodisperse microspheres in a microchannel for immunoassay applications based on optical resonances. A monodisperse stream of microspheres is produced in a microfluidic device. For immunoassay applications the microspheres can be coated with an antibody. The specific antigens can be carried at a different channel and mixed with the microspheres at a T-junction. The binding reaction kinetics can be observed by changing the flow rates and the distance between the T-junction and the excitation/detection fibers.

Reproduced with permission of the copyright owner. Further reproduction prohibited without permission.

The microdroplets can be replaced with fluorescent polystyrene or silica microspheres (beads). The same microfluidic device described in Chapter 7 can be exploited to form a monodisperse stream of microspheres. To attain optical resonances in these polystyrene ($n = 1.59$) or silica ($n = 1.46$) particles, the surrounding medium can simply be water ($n = 1.33$) rather than a special laser liquid. Optical resonances (or lasing) can be achieved if the monodisperse stream of fluorescent polystyrene microspheres is excited through an optical fiber inside the microfabricated channel (see Figure 8.2).

The water flow in the microchannel will help achieve a monodisperse flow of microspheres and also provide a low refractive index medium for the polystyrene microspheres to sustain optical resonances through total internal reflection at the interface with the surrounding liquid medium.

For biosensing applications, the microspheres can be coated with a specific antibody. The antigen that would bind to the antibody can be introduced at a T-junction through a flow perpendicular to the main stream. The change in the optical resonance spectrum due to the binding reaction can be observed. If the excitation/detection can be acquired at several points after the mixing of two flows, reaction kinetics for the antibody-antigen pair can be obtained. This can be done through setting up multiple detection ports by inserting multiple optical fiber pairs down the stream. The kinetics of the immunoassay reaction can be manipulated through the concentrations of the antibody-antigen, ratio of the flow rates and the microchannel geometry.

Reproduced with permission of the copyright owner. Further reproduction prohibited without permission.

Appendix A

Fabrication of a T-junction Microfluidic Device for Droplet Generation

A. Materials

- Pyrex 7740 wafers 4"
- SU-8 2025 (for 40 micron channel height)
- SU-8 2002 (for bonding)
- SU-8 developer
- Microscope coverslips (No.1.5)
- Sigmacote (to make the channel hydrophilic)
- Epoxy (for extra mechanical strength)
- Mask of desired design

B. Fabrication

Preparation of the wafer

1. Clean pyrex wafers in piranha (3:1 H_2SO_4:H_2O_2) and rinse thoroughly with deionized (DI) water.
2. Rinse cleaned wafers with isopropyl alcohol (IPA), dry with nitrogen and heat to 100°C for 5 minutes.

Reproduced with permission of the copyright owner. Further reproduction prohibited without permission.

3. Spin coat SU-8 2025 at 500 rpm for 5 seconds and then 2000 rpm for 30 seconds.
4. Pre-bake at 65°C for 2 minutes, ramp slowly to 95°C and heat for 5 minutes. Let cool slowly to 65°C.
5. UV (350-400nm, I-line) expose for 15 seconds through mask.
6. Post exposure bake at 65°C for 1 minute, ramp slowly to 95°C and bake for 5 minutes. Let cool slowly to 65°C and remove from hotplate.
7. Develop in SU-8 developer for approximately 1 minute, rinse with IPA and dry with nitrogen.

Preparation of the coverslip

1. Clean coverslips in piranha (3:1 H_2SO_4:H_2O_2) and rinse thoroughly with DI water.
2. Rinse cleaned coverslips with IPA, dry with nitrogen and heat to 100°C for 5 minutes.
3. Spin coat coverslips with SU-8 2002 at 500 rpm for 5 seconds and then 2000 rpm for 30 seconds.
4. Pre-bake coverslips at 65°C for 1 minute.

Assembly of the microdevice

1. Heat wafer from step 7 (preparation of the wafer) to 65°C.
2. Flip coverslips and place on wafer in desired location.
3. Heat slowly to 95°C.
4. Gently press on top of coverslip to ensure good bonding with the wafer.
5. Cool the device slowly to 65°C and remove from hotplate.
6. Align features with mask and expose for 6 seconds.
7. Bake at 65°C for 1 minute, ramp slowly to 80°C and bake for 2 minutes. Let cool slowly to 65°C and remove from hotplate.
8. Soak for at least one hour in SU-8 developer to remove the residue in the microchannels and under the coverslip.
9. Rinse with IPA and dry using vacuum to carefully suck the developer out of channels, repeat two more times.
10. Apply a few drops of epoxy to edges of coverslip and let dry.
11. Dice with dicing saw to get individual devices.
12. Apply Sigmacote for silanization and carefully remove from channel using vacuum.

Reproduced with permission of the copyright owner. Further reproduction prohibited without permission.

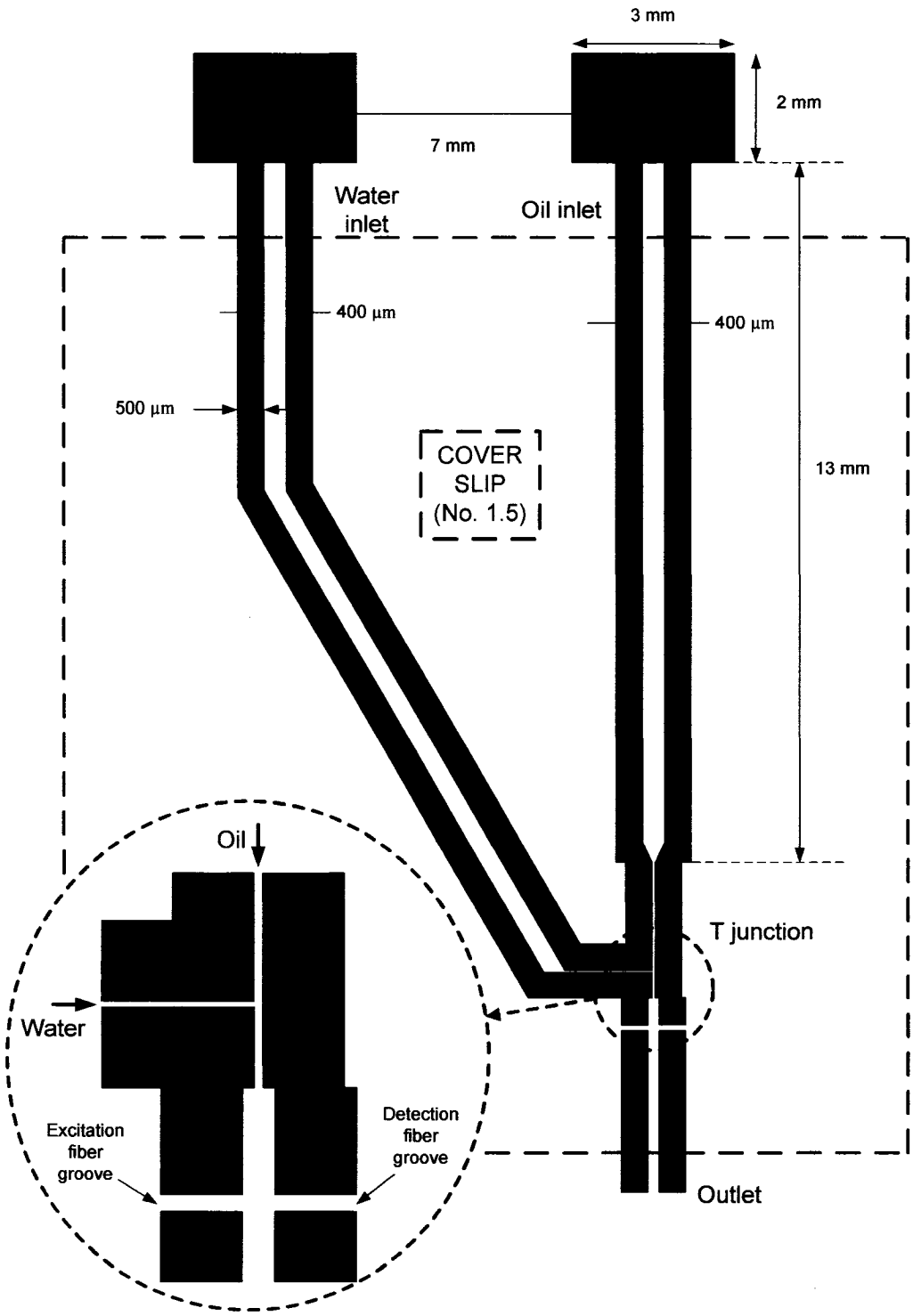

Figure A.1 Layout of a T-junction microdroplet generator. The flow in the main channel (oil) is much higher than the perpendicular channel (water) causing it to break up into small droplets due to shear. The device can produce 40-60 µm diameter water-into-oil and oil-into-water droplets depending on the hydrophobicity of the channel walls.

Reproduced with permission of the copyright owner. Further reproduction prohibited without permission.

We have also tried a flow focusing design:

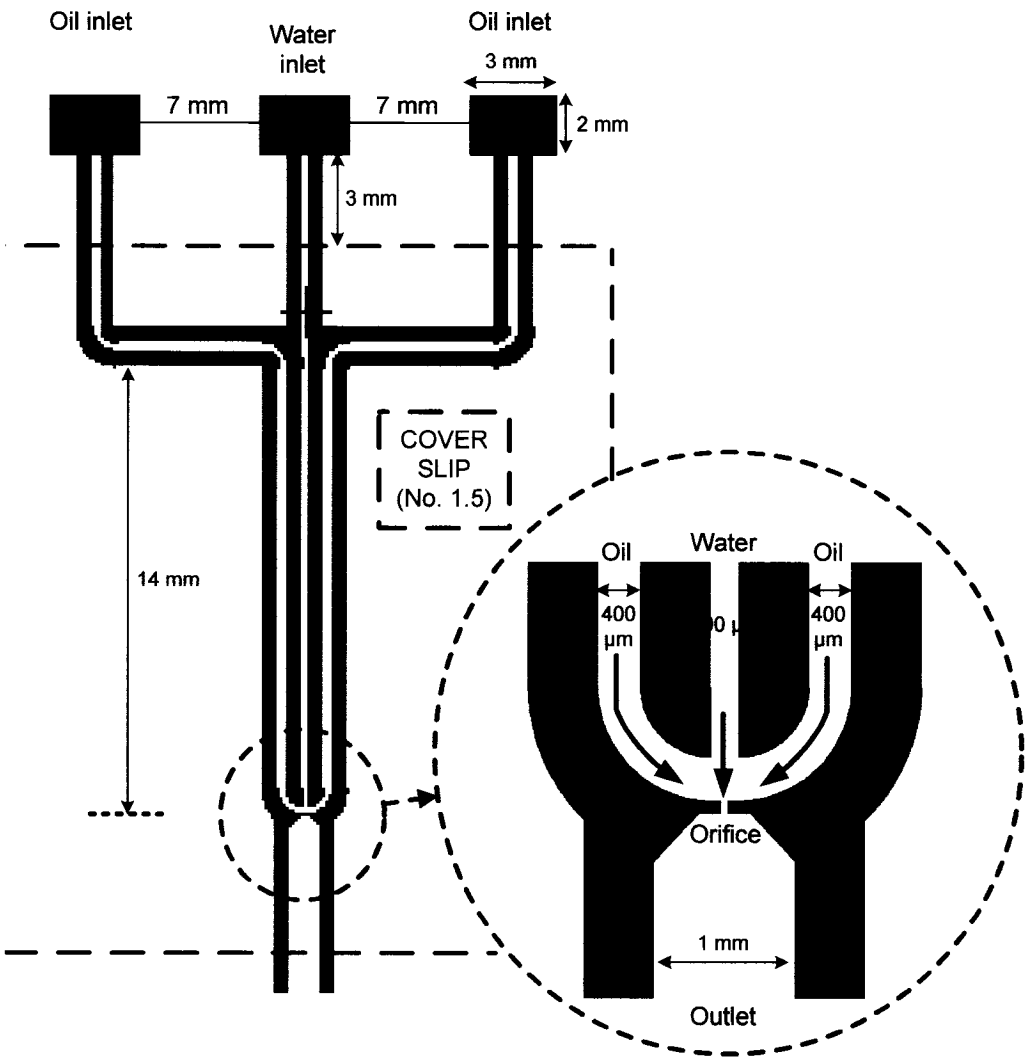

Figure A.2 Layout of a flow focusing microdroplet generator. The channel in the middle carries the liquid phase that is going to break up into droplets. The liquid in the two outer channels flow at a much higher rate than the middle one, forcing it to break up into droplets due to hydrodynamic focusing.

Fabrication of a stainless steel clamp as a microfluidic interconnect.

A novel method is developed to introduce fluid (water or oil) into the microfluidic device. After a microfluidic device is fabricated, the regular method to introduce fluid into the channels is through inserting microfluidic interconnects for each

Reproduced with permission of the copyright owner. Further reproduction prohibited without permission.

microchannel. The process is often tedious and involves gluing (epoxy) which may result in clogging the inlets of the microchannels wasting effort and time. It also makes it harder to clean and reuse the device since the device would be susceptible to clogging due to dirt or debris carried with the fluids. These drawbacks can be avoided through the use of removable microfluidic interconnect.

As depicted in the layouts above, the microchannels are 7 mm apart for both the T-junction device (which has two channels) and the flow focusing device (which has three channels). A stainless steel removable microfluidic interconnect is micromachined to introduce fluid into these microchannels. The interconnect has three metal capillary intakes that are connected to plastic capillary tubing to introduce the fluids by syringes. The three metal capillaries are linked to three tiny orifices on a stainless steel plate. The fluid coming out of the orifices is coupled into the microfluidic device. A thin rubber washer seals the connection between the stainless steel interconnect and the microfluidic device. The orifices of the interconnect and the microfluidic device are aligned under microscope to avoid any leaks. The fluids that are introduced through the interconnect are filtered. The flow rate for each microchannel can be manipulated by using separate syringe pumps.

Since this microfluidic interconnect (stainless steel clamp) is removable, both the device and the microfluidic interconnect can be cleaned thoroughly and reused for further experiments.

Reproduced with permission of the copyright owner. Further reproduction prohibited without permission.

Bibliography

1. T. Vo-Dinh, and B. Cullum, "Biosensors and biochips: advances in biological and medical diagnostics," Fresenius Journal of Analytical Chemistry 366, 540-551 (2000).
2. B. M. Paddle, "Biosensors for chemical and biological agents of defense interest," Biosensors & Bioelectronics 11, 1079-1113 (1996).
3. A. J. Baeumner, "Biosensors for environmental pollutants and food contaminants," Analytical and Bioanalytical Chemistry 377, 434-445 (2003).
4. M. A. Cooper, "Optical biosensors in drug discovery," Nature Reviews Drug Discovery 1, 515-528 (2002).
5. B. R. Eggins, *Chemical sensors and biosensors* (John Wiley, New York, 2002).
6. F. S. Ligler, and C. A. R. Taitt, *Optical biosensors : present and future* (Elsevier, Amsterdam : Oxford : , 2002).
7. G. G. Guilbault, M. Pravda, M. Kreuzer, and C. K. O'Sullivan, "Biosensors - 42 years and counting," Analytical Letters 37, 1481-1496 (2004).
8. H. Nakamura, and I. Karube, "Current research activity in biosensors," Analytical and Bioanalytical Chemistry 377, 446-468 (2003).
9. F. W. Scheller, U. Wollenberger, A. Warsinke, and F. Lisdat, "Research and development in biosensors," Current Opinion in Biotechnology 12, 35-40 (2001).
10. P. J. O'Connell, and G. G. Guilbault, "Future trends in biosensor research," Analytical Letters 34, 1063-1078 (2001).
11. C. Ziegler, and W. Gopel, "Biosensor development," Current Opinion in Chemical Biology 2, 585-591 (1998).
12. P. Vadgama, and P. W. Crump, "Biosensors - Recent Trends - a Review," Analyst 117, 1657-1670 (1992).
13. K. Cammann, U. Lemke, A. Rohen, J. Sander, H. Wilken, and B. Winter, "Chemical Sensors and Biosensors - Principles and Applications," Angewandte Chemie-International Edition in English 30, 516-539 (1991).
14. F. Scheller, F. Schubert, D. Pfeiffer, R. Hintsche, I. Dransfeld, R. Renneberg, U. Wollenberger, K. Riedel, M. Pavlova, M. Kuhn, H. G. Muller, P. M. Tan, W. Hoffmann, and W. Moritz, "Research and Development of Biosensors - a Review," Analyst 114, 653-662 (1989).
15. C. R. Lowe, "Biosensors," Trends in Biotechnology 2, 59-65 (1984).
16. G. S. Wilson, and Y. B. Hu, "Enzyme based biosensors for in vivo measurements," Chemical Reviews 100, 2693-2704 (2000).
17. K. R. Rogers, "Principles of affinity-based biosensors," Molecular Biotechnology 14, 109-129 (2000).
18. J. R. North, "Immunosensors - Antibody-Based Biosensors," Trends in Biotechnology 3, 180-186 (1985).
19. C. A. Corcoran, and G. A. Rechnitz, "Cell-Based Biosensors," Trends in Biotechnology 3, 92-96 (1985).

Reproduced with permission of the copyright owner. Further reproduction prohibited without permission.

20. E. Bakker, and Y. Qin, "Electrochemical sensors," Analytical Chemistry 78, 3965-3983 (2006).

21. J. Wang, "Amperometric biosensors for clinical and therapeutic drug monitoring: a review," Journal of Pharmaceutical and Biomedical Analysis 19, 47-53 (1999).

22. A. Janshoff, H. J. Galla, and C. Steinem, "Piezoelectric mass-sensing devices as biosensors - An alternative to optical biosensors?," Angewandte Chemie-International Edition 39, 4004-4032 (2000).

23. R. L. Bunde, E. J. Jarvi, and J. J. Rosentreter, "Piezoelectric quartz crystal biosensors," Talanta 46, 1223-1236 (1998).

24. N. V. Lavrik, M. J. Sepaniak, and P. G. Datskos, "Cantilever transducers as a platform for chemical and biological sensors," Review of Scientific Instruments 75, 2229-2253 (2004).

25. R. Raiteri, M. Grattarola, H. J. Butt, and P. Skladal, "Micromechanical cantilever-based biosensors," Sensors and Actuators B-Chemical 79, 115-126 (2001).

26. J. J. Ramsden, "Optical biosensors," Journal of Molecular Recognition 10, 109-120 (1997).

27. C. L. Baird, and D. G. Myszka, "Current and emerging commercial optical biosensors," Journal of Molecular Recognition 14, 261-268 (2001).

28. B. M. Cullum, and T. Vo-Dinh, "The development of optical nanosensors for biological measurements [Review]," Trends in Biotechnology 18, 388-393 (2000).

29. O. S. Wolfbeis, "Fiber-optic chemical sensors and biosensors," Analytical Chemistry 76, 3269-3283 (2004).

30. M. A. Cooper, "Label-free screening of bio-molecular interactions," Analytical and Bioanalytical Chemistry 377, 834-842 (2003).

31. J. Homola, S. S. Yee, and G. Gauglitz, "Surface plasmon resonance sensors: review," Sensors and Actuators B-Chemical 54, 3-15 (1999).

32. J. C. Owicki, L. J. Bousse, D. G. Hafeman, G. L. Kirk, J. D. Olson, H. G. Wada, and J. W. Parce, "The Light-Addressable Potentiometric Sensor - Principles and Biological Applications," Annual Review of Biophysics and Biomolecular Structure 23, 87-113 (1994).

33. A. Yalcin, K. C. Popat, J. C. Aldridge, T. A. Desai, J. Hryniewicz, N. Chbouki, B. E. Little, O. King, V. Van, S. Chu, D. Gill, M. Anthes-Washburn, and M. S. Unlu, "Optical sensing of biomolecules using microring resonators," Ieee Journal of Selected Topics in Quantum Electronics 12, 148-155 (2006).

34. F. Vollmer, D. Braun, A. Libchaber, M. Khoshsima, I. Teraoka, and S. Arnold, "Protein detection by optical shift of a resonant microcavity," Applied Physics Letters 80, 4057-4059 (2002).

35. L. Rayleigh, "The problem of the whispering gallery," Philosophical Magazine 20, 1001-1004 (1910).

36. A. Ashkin, "Observation of resonances in radiation pressure on dielectric spheres," Physical Review Letters 38, 1351-1354 (1977).

37. J. A. Stratton, *Electromagnetic theory* (McGraw-Hill book company inc., New York, London,, 1941).

38. H. C. v. d. Hulst, *Light scattering by small particles* (Wiley, New York,, 1957).

39. M. Kerker, *The scattering of light, and other electromagnetic radiation* (Academic Press, New York,, 1969).

Reproduced with permission of the copyright owner. Further reproduction prohibited without permission.

40. C. F. Bohren, and D. R. Huffman, *Absorption and scattering of light by small particles* (Wiley, New York, 1983).

41. R. D. Van Zee, and J. P. Looney, *Cavity-enhanced spectroscopies* (Academic Press, San Diego, 2002).

42. B. R. Johnson, "Theory of Morphology-Dependent Resonances - Shape Resonances and Width Formulas," Journal of the Optical Society of America a-Optics Image Science and Vision 10, 343-352 (1993).

43. P. Chylek, "Partial-wave resonances and ripple structure in Mie normalized extinction cross-section," Journal of the Optical Society of America 66, 285 (1976).

44. P. Chylek, J. T. Kiehl, and M. K. W. Ko, "Optical levitation and partial-wave resonances," Physical Review A 18, 2229 (1978).

45. P. Chylek, V. Ramaswamy, A. Ashkin, and J. M. Dziedzic, "Simultaneous Determination of Refractive-Index and Size of Spherical Dielectric Particles from Light-Scattering Data," Applied Optics 22, 2302-2307 (1983).

46. P. R. Conwell, C. K. Rushforth, R. E. Benner, and S. C. Hill, "Efficient Automated Algorithm for the Sizing of Dielectric Microspheres Using the Resonance-Spectrum," Journal of the Optical Society of America a-Optics Image Science and Vision 1, 1181-1187 (1984).

47. J. L. Huckaby, A. K. Ray, and B. Das, "Determination of Size, Refractive-Index, and Dispersion of Single Droplets from Wavelength-Dependent Scattering Spectra," Applied Optics 33, 7112-7125 (1994).

48. J. Popp, M. Lankers, M. Trunk, I. Hartmann, E. Urlaub, and W. Kiefer, "High-precision determination of size, refractive index, and dispersion of single microparticles from morphology-dependent resonances in optical processes," Applied Spectroscopy 52, 284-291 (1998).

49. T. Mukaiyama, K. Takeda, H. Miyazaki, Y. Jimba, and M. Kuwata-Gonokami, "Tight-binding photonic molecule modes of resonant bispheres," Physical Review Letters 82, 4623-4626 (1999).

50. L. Collot, V. Lefevreseguin, M. Brune, J. M. Raimond, and S. Haroche, "Very High-Q Whispering-Gallery Mode Resonances Observed on Fused-Silica Microspheres," Europhysics Letters 23, 327-334 (1993).

51. A. Ashkin, and J. M. Dziedzic, "Observation of Optical Resonances of Dielectric Spheres by Light-Scattering," Applied Optics 20, 1803-1814 (1981).

52. R. E. Benner, P. W. Barber, J. F. Owen, and R. K. Chang, "Observation of Structure Resonances in the Fluorescence-Spectra from Microspheres," Physical Review Letters 44, 475-478 (1980).

53. J. F. Owen, R. K. Chang, and P. W. Barber, "Morphology-Dependent Resonances in Raman-Scattering, Fluorescence Emission, and Elastic-Scattering from Microparticles," Aerosol Science and Technology 1, 293-302 (1982).

54. R. Thurn, and W. Kiefer, "Observations of Structural Resonances in the Raman-Spectra of Optically Levitated Dielectric Microspheres," Journal of Raman Spectroscopy 15, 411-413 (1984).

55. S. X. Qian, J. B. Snow, H. M. Tzeng, and R. K. Chang, "Lasing Droplets - Highlighting the Liquid-Air Interface by Laser-Emission," Science 231, 486-488 (1986).

56. H. M. Tzeng, K. F. Wall, M. B. Long, and R. K. Chang, "Laser-Emission from Individual Droplets at Wavelengths Corresponding to Morphology-Dependent Resonances," Optics Letters 9, 499-501 (1984).

Reproduced with permission of the copyright owner. Further reproduction prohibited without permission.

57. J. R. Lakowicz, *Principles of fluorescence spectroscopy* (Springer, New York, 2004).

58. E. M. Purcell, "Spontaneous emission probabilities at radio frequencies," Physical Review 69, 681 (1946).

59. H. B. Lin, J. D. Eversole, C. D. Merritt, and A. J. Campillo, "Cavity-Modified Spontaneous-Emission Rates in Liquid Microdroplets," Physical Review A 45, 6756-6760 (1992).

60. D. Kleppner, "Inhibited Spontaneous Emission," Physical Review Letters 47, 233-236 (1981).

61. P. Sandeep, and P. B. Bisht, "Concentration sensing based on radiative rate enhancement from a single microcavity," Chemical Physics Letters 415, 15-19 (2005).

62. M. D. Barnes, W. B. Whitten, and J. M. Ramsey, "Enhanced Fluorescence Yields through Cavity Quantum-Electrodynamic Effects in Microdroplets," Journal of the Optical Society of America B-Optical Physics 11, 1297-1304 (1994).

63. M. D. Barnes, W. B. Whitten, and J. M. Ramsey, "Probing Femtosecond Dynamics in Solution on a Picosecond Time-Scale - Cavity Enhancement of Spontaneous Emission Rates in Microdroplets," Chemical Physics Letters 227, 628-632 (1994).

64. M. D. Barnes, W. B. Whitten, S. Arnold, and J. M. Ramsey, "Homogeneous Linewidths of Rhodamine-6G at Room-Temperature from Cavity-Enhanced Spontaneous Emission Rates," Journal of Chemical Physics 97, 7842-7845 (1992).

65. P. Andrew, and W. L. Barnes, "Forster energy transfer in an optical microcavity," Science 290, 785-788 (2000).

66. G. Griffel, S. Arnold, D. Taskent, A. Serpenguzel, J. Connolly, and N. Morris, "Morphology-dependent resonances of a microsphere-optical fiber system," Optics Letters 21, 695-697 (1996).

67. L. M. Folan, S. Arnold, and S. D. Druger, "Enhanced Energy-Transfer within a Microparticle," Chemical Physics Letters 118, 322-327 (1985).

68. W. B. Whitten, M. J. Shapiro, J. M. Ramsey, and B. V. Bronk, "Morphological Resonances for Multicomponent Immunoassays," Applied Optics 34, 3203-3207 (1995).

69. F. Vollmer, S. Arnold, D. Braun, I. Teraoka, and A. Libchaber, "Multiplexed DNA quantification by spectroscopic shift of two microsphere cavities," Biophysical Journal 85, 1974-1979 (2003).

70. N. M. Hanumegowda, C. J. Stica, B. C. Patel, I. White, and X. D. Fan, "Refractometric sensors based on microsphere resonators," Applied Physics Letters 87, (2005).

71. N. M. Hanumegowda, I. M. White, and X. D. Fan, "Aqueous mercuric ion detection with microsphere optical ring resonator sensors," Sensors and Actuators B-Chemical 120, 207-212 (2006).

72. N. M. Hanumegowda, I. M. White, H. Oveys, and X. D. Fan, "Label-free protease sensors based on optical microsphere resonators," Sensor Letters 3, 315-319 (2005).

73. I. M. White, N. M. Hanumegowda, and X. D. Fan, "Subfemtomole detection of small molecules with microsphere sensors," Optics Letters 30, 3189-3191 (2005).

74. H. Y. Zhu, J. D. Suter, I. M. White, and X. D. Fan, "Aptamer based microsphere biosensor for thrombin detection," Sensors 6, 785-795 (2006).

75. I. M. White, N. M. Hanumegowda, H. Oveys, and X. D. Fan, "Tuning whispering gallery modes in optical microspheres with chemical etching," Optics Express 13, 10754-10759 (2005).

Reproduced with permission of the copyright owner. Further reproduction prohibited without permission.

76. I. M. White, H. Oveys, X. Fan, T. L. Smith, and J. Y. Zhang, "Integrated multiplexed biosensors based on liquid core optical ring resonators and antiresonant reflecting optical waveguides," Applied Physics Letters 89, (2006).

77. I. M. White, H. Oveys, and X. D. Fan, "Liquid-core optical ring-resonator sensors," Optics Letters 31, 1319-1321 (2006).

78. S. Blair, and Y. Chen, "Resonant-enhanced evanescent-wave fluorescence biosensing with cylindrical optical cavities," Applied Optics 40, 570-582 (2001).

79. R. W. Boyd, and J. E. Heebner, "Sensitive disk resonator photonic biosensor," Applied Optics 40, 5742-5747 (2001).

80. A. M. Armani, and K. J. Vahala, "Heavy water detection using ultra-high-Q microcavities," Optics Letters 31, 1896-1898 (2006).

81. C. Y. Chao, W. Fung, and L. J. Guo, "Polymer microring resonators for biochemical sensing applications," Ieee Journal of Selected Topics in Quantum Electronics 12, 134-142 (2006).

82. C. Y. Chao, and L. J. Guo, "Biochemical sensors based on polymer microrings with sharp asymmetrical resonance," Applied Physics Letters 83, 1527-1529 (2003).

83. S. Y. Cho, and N. M. Jokerst, "A polymer microdisk photonic sensor integrated onto silicon," Ieee Photonics Technology Letters 18, 2096-2098 (2006).

84. W. Fang, D. B. Buchholz, R. C. Bailey, J. T. Hupp, R. P. H. Chang, and H. Cao, "Detection of chemical species using ultraviolet microdisk lasers," Applied Physics Letters 85, 3666-3668 (2004).

85. A. Ksendzov, M. L. Homer, and A. M. Manfreda, "Integrated optics ring-resonator chemical sensor with polymer transduction layer," Electronics Letters 40, 63-65 (2004).

86. A. Ksendzov, and Y. Lin, "Integrated optics ring-resonator sensors for protein detection," Optics Letters 30, 3344-3346 (2005).

87. M. Rosenblit, P. Horak, S. Helsby, and R. Folman, "Single-atom detection using whispering-gallery modes of microdisk resonators," Physical Review A 70, (2004).

88. J. Yang, and L. J. Guo, "Optical sensors based on active microcavities," Ieee Journal of Selected Topics in Quantum Electronics 12, 143-147 (2006).

89. I. Teraoka, and S. Arnold, "Enhancing the sensitivity of a whispering-gallery mode microsphere sensor by a high-refractive-index surface layer," Journal of the Optical Society of America B-Optical Physics 23, 1434-1441 (2006).

90. I. Teraoka, and S. Arnold, "Theory of resonance shifts in TE and TM whispering gallery modes by nonradial perturbations for sensing applications," Journal of the Optical Society of America B-Optical Physics 23, 1381-1389 (2006).

91. C. Y. Chao, and L. J. Guo, "Design and optimization of microring resonators in biochemical sensing applications," Journal of Lightwave Technology 24, 1395-1402 (2006).

92. S. V. Boriskina, "Spectrally engineered photonic molecules as optical sensors with enhanced sensitivity: a proposal and numerical analysis," Journal of the Optical Society of America B-Optical Physics 23, 1565-1573 (2006).

93. H. Y. Quan, and Z. X. Guo, "Simulation of whispering-gallery-mode resonance shifts for optical miniature biosensors," Journal of Quantitative Spectroscopy & Radiative Transfer 93, 231-243 (2005).

Reproduced with permission of the copyright owner. Further reproduction prohibited without permission.

94. M. Noto, M. Khoshsima, D. Keng, I. Teraoka, V. Kolchenko, and S. Arnold, "Molecular weight dependence of a whispering gallery mode biosensor," Applied Physics Letters 87, (2005).

95. I. Teraoka, S. Arnold, and F. Vollmer, "Perturbation approach to resonance shifts of whispering-gallery modes in a dielectric microsphere as a probe of a surrounding medium," Journal of the Optical Society of America B-Optical Physics 20, 1937-1946 (2003).

96. E. Krioukov, J. Greve, and C. Otto, "Performance of integrated optical microcavities for refractive index and fluorescence sensing," Sensors and Actuators B-Chemical 90, 58-67 (2003).

97. S. Arnold, M. Khoshsima, I. Teraoka, S. Holler, and F. Vollmer, "Shift of whispering-gallery modes in microspheres by protein adsorption," Optics Letters 28, 272-274 (2003).

98. G. Schweiger, and M. Horn, "Effect of changes in size and index of refraction on the resonance wavelength of microspheres," Journal of the Optical Society of America B-Optical Physics 23, 212-217 (2006).

99. A. B. Matsko, and V. S. Ilchenko, "Optical resonators with whispering-gallery modes - Part I: Basics," Ieee Journal of Selected Topics in Quantum Electronics 12, 3-14 (2006).

100. V. S. Ilchenko, and A. B. Matsko, "Optical resonators with whispering-gallery modes - Part II: Applications," Ieee Journal of Selected Topics in Quantum Electronics 12, 15-32 (2006).

101. P. L. Gourley, "Biocavity laser for high-speed cell and tumour biology," Journal of Physics D-Applied Physics 36, R228-R239 (2003).

102. R. L. Armstrong, J. G. Xie, T. E. Ruekgauer, J. Gu, and R. G. Pinnick, "Effects of Submicrometer-Sized Particles on Microdroplet Lasing," Optics Letters 18, 119-121 (1993).

103. H. B. Lin, A. L. Huston, J. D. Eversole, A. J. Campillo, and P. Chylek, "Internal Scattering Effects on Microdroplet Resonant Emission Structure," Optics Letters 17, 970-972 (1992).

104. D. Ngo, and R. G. Pinnick, "Suppression of Scattering Resonances in Inhomogeneous Microdroplets," Journal of the Optical Society of America a-Optics Image Science and Vision 11, 1352-1359 (1994).

105. J. G. Xie, T. E. Ruekgauer, R. L. Armstrong, and R. G. Pinnick, "Suppression of Stimulated Raman-Scattering from Microdroplets by Seeding with Nanometer-Sized Latex-Particles," Optics Letters 18, 340-342 (1993).

106. A. L. Huston, H. B. Lin, J. D. Eversole, and A. J. Campillo, "Effect of bubble formation on microdroplet cavity quality factors," Journal of the Optical Society of America B-Optical Physics 13, 521-531 (1996).

107. P. T. Leung, S. W. Ng, K. M. Pang, and K. M. Lee, "Morphology-dependent resonances in dielectric spheres with many tiny inclusions," Optics Letters 27, 1749-1751 (2002).

108. H. Taniguchi, M. Nishiya, S. Tanosaki, and H. Inaba, "Lasing behavior in a liquid spherical dye laser containing highly scattering nanoparticles," Optics Letters 21, 263-265 (1996).

109. T. Maniatis, E. F. Fritsch, and J. Sambrook, *Molecular cloning: a laboratory manual* (Cold Spring Harbor Laboratory, Cold Spring Harbor, N.Y., 1982).

110. S. A. E. Marras, F. R. Kramer, and S. Tyagi, "Efficiencies of fluorescence resonance energy transfer and contact-mediated quenching in oligonucleotide probes," Nucleic Acids Research 30, (2002).

Reproduced with permission of the copyright owner. Further reproduction prohibited without permission.

111. M. Adamczyk, J. A. Moore, and K. Shreder, "Quenching of biotinylated aequorin bioluminescence by dye-labeled avidin conjugates: Application to homogeneous bioluminescence resonance energy transfer assays," Organic Letters 3, 1797-1800 (2001).

112. J. G. Bruno, S. J. Ulvick, G. L. Uzzell, J. S. Tabb, E. R. Valdes, and C. A. Batt, "Novel immuno-FRET assay method for Bacillus spores and Escherichia coli O157 : H7," Biochemical and Biophysical Research Communications 287, 875-880 (2001).

113. S. A. Grant, J. T. Xu, E. J. Bergeron, and J. Mroz, "Development of dual receptor biosensors: an analysis of FRET pairs," Biosensors & Bioelectronics 16, 231-237 (2001).

114. S. Ko, and S. A. Grant, "Development of a novel FRET method for detection of Listeria or Salmonella," Sensors and Actuators B-Chemical 96, 372-378 (2003).

115. E. Michelini, M. Mirasoli, M. Karp, M. Virta, and A. Roda, "Development of a bioluminescence resonance energy-transfer assay for estrogen-like compound in vivo monitoring," Analytical Chemistry 76, 7069-7076 (2004).

116. P. J. Santangelo, B. Nix, A. Tsourkas, and G. Bao, "Dual FRET molecular beacons for mRNA detection in living cells," Nucleic Acids Research 32, (2004).

117. G. L. Wang, J. L. Yuan, K. Matsumoto, and Z. D. Hu, "Homogeneous time-resolved fluoroimmunoassay of bensulfuron-methyl by using terbium fluorescence energy transfer," Talanta 55, 1119-1125 (2001).

118. E. Zahavy, M. Fisher, A. Bromberg, and U. Olshevsky, "Detection of frequency resonance energy transfer pair on double-labeled microsphere and Bacillus anthracis spores by flow cytometry," Applied and Environmental Microbiology 69, 2330-2339 (2003).

119. J. Feng, G. M. Shan, B. D. Hammock, and I. M. Kennedy, "Fluorescence quenching competitive immunoassay in micro droplets," Biosensors & Bioelectronics 18, 1055-1063 (2003).

120. M. Nichkova, J. Feng, F. Sanchez-Baeza, M. P. Marco, B. D. Hammock, and I. M. Kennedy, "Competitive quenching fluorescence immunoassay for chlorophenols based on laser-induced fluorescence detection in microdroplets," Analytical Chemistry 75, 83-90 (2003).

121. S. Arnold, and L. M. Folan, "Energy-Transfer and the Photon Lifetime within an Aerosol-Particle," Optics Letters 14, 387-389 (1989).

122. S. Arnold, S. Holler, and S. D. Druger, "Imaging enhanced energy transfer in a levitated aerosol particle," Journal of Chemical Physics 104, 7741-7748 (1996).

123. S. D. Druger, S. Arnold, and L. M. Folan, "Theory of Enhanced Energy-Transfer between Molecules Embedded in Spherical Dielectric Particles," Journal of Chemical Physics 87, 2649-2659 (1987).

124. R. Symes, R. M. Sayer, and J. P. Reid, "Cavity enhanced droplet spectroscopy: Principles, perspectives and prospects," Physical Chemistry Chemical Physics 6, 474-487 (2004).

125. A. D. Dinsmore, M. F. Hsu, M. G. Nikolaides, M. Marquez, A. R. Bausch, and D. A. Weitz, "Colloidosomes: Selectively permeable capsules composed of colloidal particles," Science 298, 1006-1009 (2002).

126. S. S. Chang, N. B. Rex, and R. K. Chang, "Chemical lasing in pendant droplets: lasing-spectra, emission-pattern, and cavity-lifetime measurements," Journal of the Optical Society of America B-Optical Physics 16, 1224-1235 (1999).

Reproduced with permission of the copyright owner. Further reproduction prohibited without permission.

127. X. Y. Pu, and W. K. Lee, "Lasing characteristics of a pendant drop deformed by an applied electric field," Optics Letters 25, 466-468 (2000).

128. X. Y. Pu, C. W. Chan, and W. K. Lee, "Measurement of the internal lasing intensity distribution of a dye-doped pendant drop," Optics Letters 25, 1514-1516 (2000).

129. A. A. Savchenkov, I. S. Grudinin, A. B. Matsko, D. Strekalov, M. Mohageg, V. S. Chenko, and L. Maleki, "Morphology-dependent photonic circuit elements," Optics Letters 31, 1313-1315 (2006).

130. B. E. Little, J. P. Laine, D. R. Lim, H. A. Haus, L. C. Kimerling, and S. T. Chu, "Pedestal antiresonant reflecting waveguides for robust coupling to microsphere resonators and for microphotonic circuits," Optics Letters 25, 73-75 (2000).

131. S. K. Padigi, K. Asante, V. S. R. Kovvuri, R. K. K. Reddy, A. La Rosa, and S. Prasad, "Micro-photonic cylindrical waveguide based protein biosensor," Nanotechnology 17, 4384-4390 (2006).

132. G. Chen, M. M. Mazumder, R. K. Chang, J. C. Swindal, and W. P. Acker, "Laser diagnostics for droplet characterization: Application of morphology dependent resonances," Progress in Energy and Combustion Science 22, 163-188 (1996).

133. J. D. Eversole, H. B. Lin, and A. J. Campillo, "Cavity-Mode Identification of Fluorescence and Lasing in Dye-Doped Microdroplets," Applied Optics 31, 1982-1991 (1992).

134. P. Garstecki, M. J. Fuerstman, H. A. Stone, and G. M. Whitesides, "Formation of droplets and bubbles in a microfluidic T-junction - scaling and mechanism of break-up," Lab on a Chip 6, 437-446 (2006).

135. T. Nisisako, T. Torii, and T. Higuchi, "Droplet formation in a microchannel network," Lab on a Chip 2, 24-26 (2002).

136. T. Thorsen, R. W. Roberts, F. H. Arnold, and S. R. Quake, "Dynamic pattern formation in a vesicle-generating microfluidic device," Physical Review Letters 86, 4163-4166 (2001).

137. A. Serpenguzel, S. Arnold, G. Griffel, and J. A. Lock, "Enhanced coupling to microsphere resonances with optical fibers," Journal of the Optical Society of America B-Optical Physics 14, 790-795 (1997).

Reproduced with permission of the copyright owner. Further reproduction prohibited without permission.